Integrating Nanomechanical Property Testing into a Correlative Imaging Workflow

Presented by: Rachel Gwyneth Board

Submitted to Swansea University in fulfilment of the requirements for the degree of Doctor of Philosophy

Swansea University

2022

Abstract

This work is aimed at creating a cohesive workflow between correlative imaging techniques and nanomechanical property testing for materials analysis.

There exist multiple features of a material, on varying length scales, that can determine its performance in its desired function. As technology advances new materials are developed to address new problems with more and more taking their inspiration from nature. The use of different techniques individually has been able to shed light on either the structure, property, or function of the materials, either manufactured or biological. Understanding has developed that the three aspects; structure, property, and function are related and should be considered together when analysing a material. Combining multiple techniques in a workflow will allow for revealing the 'whole picture' of the material. The methods of materials analysis used in this research are X-ray micro-CT, scanning electron microscopy (SEM), light microscopy, X-ray fluorescence (XRF), and nanoindentation.

Each of the methods used here requires specific preparation methods prior to testing and one testing method may make the sample unsuitable for another testing method. Therefore, planning the sequence of testing before commencing is of high importance. Putting into place a workflow will not only reduce the likelihood of inhibiting further testing procedures but also reduce the time taken for completing a comprehensive analysis.

The workflow proposed here takes into consideration what information can be gained as well as preparation techniques. Initially, this thesis will discuss correlative imaging detailing, sample preparation, and the capabilities of these techniques in uncovering the internal nano – to the macro-structure of antler bone and barnacle plate organisation, as well as the chemical uniformity of the inorganic phase of antler bone across the cross-section and the elongated crystallographic structures unique to the barnacle ala.

Secondly, XRF will be explored for its role in the chemical analysis of biological materials and where this technique can be placed into the workflow to impact the overall understanding of the chemical composition in this instance in the application of antlers.
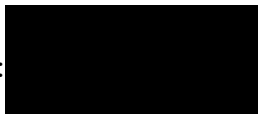
Finally covered will be nanomechanical property testing for both stand-alone equipment and in-situ indentation. The suggested position for this technique in the workflow will be explained as it is used as the final connecting piece in determining the structure-function-property relationship of the material due to how the previous methods have directed the research process. Correlating the accelerated property mapping technique to the crystallographic structures in barnacle plates showed a reduced hardness in the elongated crystal region. Nanoindentation of the antler bone showed differences in modulus between the transverse and cross-sections as well as a reduction in average hardness between the male antler and the female reindeer that had calves and those that did not.

Each of the individual pieces of information in this workflow when brought together unveils the hidden structure-property-function relationship in materials to provide an in-depth understanding.

Declarations

This work has not previously been accepted in substance for any degree and is not being concurrently submitted in candidature for any degree.
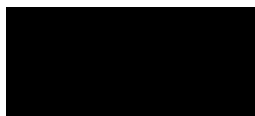
Signed: ███████████

Date: 12/12/2022

This thesis is the result of my own investigations, except where otherwise stated. Other sources are acknowledged by footnotes giving explicit references.   A bibliography is appended.

Signed: ███████████

Date: 12/12/2022

I hereby give consent for my thesis, if accepted, to be available for electronic sharing **after expiry of a bar on access approved by the Swansea University.**

Signed: ███████████

Date: 12/12/2022

The University's ethical procedures have been followed and, where appropriate, that ethical approval has been granted.

Signed: ███████████

Date: 12/12/2022

Table of Contents

Acknowledgements

List of Figures

List of Tables

1 Introduction

1.2 Aims and Objectives

The aim of this work is to develop a cohesive workflow for the comprehensive analysis of materials. This has been carried out with a focus of applying the recommended methods on biological materials. This workflow combines various imaging techniques with nanomechanical property testing for material analysis, facilitating a comprehensive grasp of the material. Importantly, this understanding will explain the interplay between the structures, properties, and functionality of the material, and how to overcome the challenges posed by the analysis of biological materials. The accumulated workflow is presented in Figure 1.1. It takes into account the many factors that must be considered when determining which procedures are necessary and which are not required to further contribute to the understanding of the sample material.
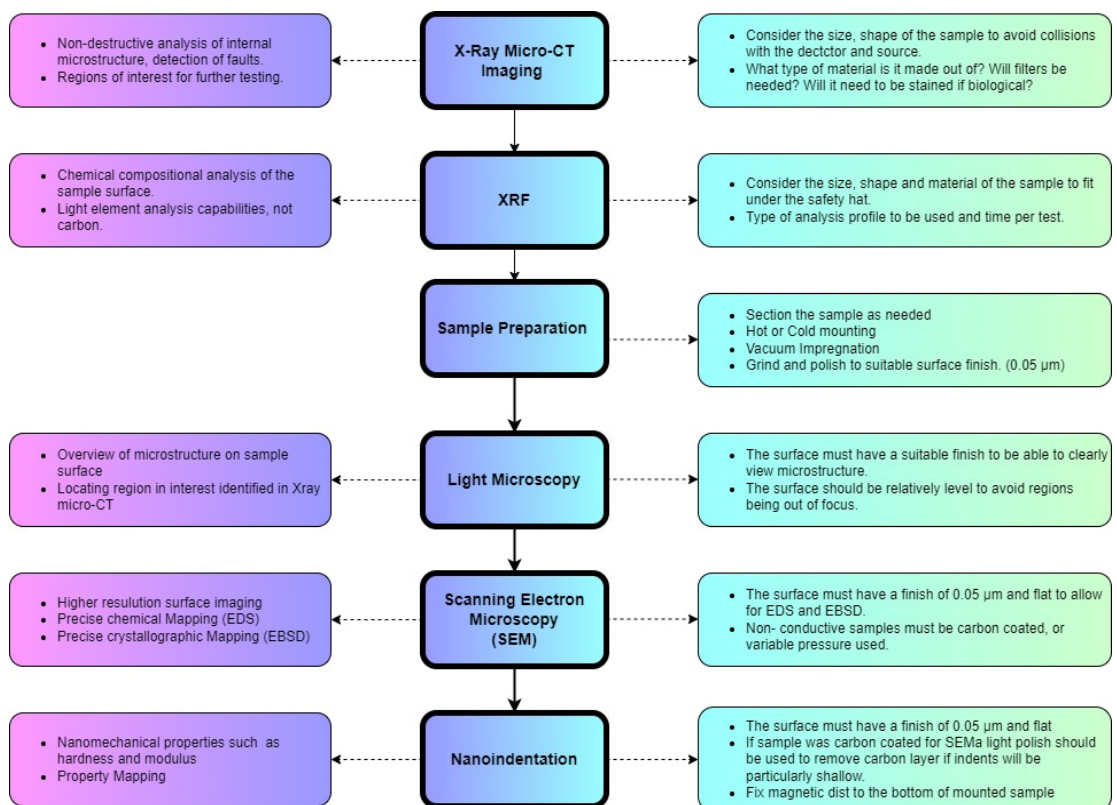
Figure 1.1. Flowchart of the workflow process. Included are the techniques in the centre with its features and capabilities on the left-hand side as well as the factors to consider for the technique on the right-hand side.

The workflow summarised in Figure 1.1. on the left-hand side shows that many factors must be considered when determining which procedures are necessary and which will not further contribute to the understanding of the sample material. This reflects on the flexibility of the workflow, as not all techniques need to be performed. Of these factors to be considered is if the material is manufactured or natural as this will affect how the methods are approached.

X-ray micro-CT imaging is at the start of the workflow as the samples do not require much preparation, this will also allow for a better understanding of the internal microstructure as it has not undergone much manipulation. X-ray fluorescence (XRF) is performed before mounting the sample to prevent contamination of the results by the process of preparation, such as mounting, grinding and polishing.

Once the previous techniques are performed the sample preparation for the following techniques are very similar requiring the sample to be mounted and have a finish of 0.05 μ. Hence, the placement of this step within the workflow finds its rationale. In the microscopy techniques, light and SEM this allows for better visualisation of surface microstructures as well as in SEM for reliable EDS and EBSD data.

Nanoindentation is placed as the final technique as this involves the application of a load to the surface with a probe of known geometry, this leaves indentations on the sample creating roughness which can go on to affect the microscopy techniques if it was performed prior to those techniques.

This chapter will introduce the concept of correlative imaging in regard to the techniques applied in the recommended workflow. Nanomechanical testing will also be introduced expressing the value of this technique when evaluating the structure-property-function relationship of the material. The structure of the thesis will also be discussed in this chapter showing how each aspect of the workflow has been applied. The two biological samples analysed in this thesis will also be introduced here, prior to the detail that will be covered in the literature review.

1.3 Correlative Imaging

Correlative imaging is the use of multiple imaging techniques to reveal information on the structure, morphology, and/or composition of a material. This can be applied to biological, geological, or manufactured materials(1). The imaging techniques commonly used include (a) X-ray micro-CT for non-destructive 3D analysis; (b) Light microscopy provides information on the surface features such as grain structure in metals, as well as natural formations in biological materials; (c) Scanning electron microscopy (SEM) provides surface feature analysis at a higher resolution as well as enabling other analytical techniques such as energy dispersive spectroscopy (EDS) for revealing the chemical compositions and their locations on the sample surface and electron backscatter diffraction (EBSD) for microstructural and crystallographic characterisation. Correlating these methods allows for an in-depth understanding of the structure of a material (2).

1.4 Nanomechanical testing

Nanomechanical testing provides another 'lens' for the understanding of the material by providing information on the properties of the regions imaged. With this information in hand, being able to relate how the structures observed with microscopy impact the mechanical properties is crucial in understanding the relationship that these features have towards the function of a material (3). Correlative imaging analysis is often carried out without nanoindentation. By adding this step further scope is added to the structure-property-function relationship of materials. This work will fully integrate nanoindentation into a correlative imaging workflow to allow for comprehensive materials characterisation.

Several previous studies have employed correlative imaging techniques to reveal the structure and function relationship in different fields from polymer research (4) to ferroelectrics (5). Although much was understood about the materials, the complexity of the behaviour of the materials were not able to be fully understood. Other studies, such as by Godec (6), tested mechanical properties of a material to correlate with multiple imaging techniques. They analysed the bulk material properties to compare

to localised crystallographic and chemical features. Using more localised testing methods such as nanoindentation and accelerated property mapping, an emerging technique, of these localised features would enable a more comprehensive understanding of the behaviour of the material on the scale imaged (6).

Manufactured materials are often tailor-made for purpose (7) and require rigorous testing to ensure that standards are met to ensure the safety and durability of a product (8) this is done by the application of robust testing methods.

1.5   Bioinspiration

The field of bioinspiration for materials is based upon drawing on ideas from nature where millions of years of evolution have resulted in the development of efficient structures. Bioinspiration leading to bioinspired designs has advanced due to improvements in analytical techniques such as in imaging and mechanical property testing. Correlating these techniques in a logical work flow will unveil the interconnected structure-function-relationship of biological materials (9,10).

Mineralised biological materials were the focus of study in this research project, including reindeer antler (11–13) and barnacle plate alae (3). The work done with the barnacle plate ala is to complement existing correlative imaging findings published by the Advanced Imaging of Materials (AIM) group at Swansea University, this initial work did not include nanomechanical property testing as it used the more traditional approach of a correlative imaging workflow. Reindeer antler underwent the complete workflow process from project conception, specimen search, and subsequent characterisation workflows.

1.6   Barnacle

This study is a continuation of work previously carried out by the Advanced Imaging of Materials (AIM) group at Swansea University in conjunction with industrial partners, Carl Zeiss microscopy. In the study published by Mitchell *et al*. a comprehensive imaging analysis was performed to understand the complexities of the structure. The techniques they applied were, X-ray microscopy, scanning electron microscopy, electron back scatter diffraction, light microscopy and focused ion beam scanning electron microscopy (3). Nanomechanical property testing, nanoindentation and in-situ testing will add valuable information to the properties of the structures studied and further develop the hypothesizes of the functionality arising from the previous work.

1.7   Antlers

Additionally, this study aims to further evaluate the differences between male and female antlers in reindeer, particularly the effect of calving on the properties of female reindeer antlers. X-ray micro-CT will be used to evaluate the internal 3D morphology, comparing the sizes of the compact bone regions, and the thickness and directionality of the trabecular region. X-ray fluorescence will be used to perform elemental analysis. Nanoindentation will be used to investigate the nanomechanical properties of the antlers in the different regions to locate any heterogeneities within the antler and between antlers of male, female, and females that have calved.

1.8 Structure of thesis

The format of this thesis will be explained in this section with an overview of the contents of each of the sections.

1.8.1   Literature review

This section reviews literature involving all the techniques in the workflow and their relevant applications to materials analysis as well as detailing the principles behind each technique. This will give further understanding as to the sequence of techniques in the workflow. This section also goes into understanding the material being tested. This is crucial as it will affect the approach of the workflow such as for biological materials. This section finally details the literature on the two main materials studied in the application of the workflow, barnacles and antlers.

1.8.2   Methods

The details regarding the applied techniques are explained in this section, and possible special considerations for the materials. It is organised to provide information the techniques as they are applied to each sample, barnacle and antlers respectively. This shows how the recommended procedure is able to flow smoothly between techniques if they are applied following the recommended workflow.

1.8.3   Results and Discussion

The data acquired from the techniques applied will displayed and discussed in this section for both barnacle and antler samples tested respectively. In this section attention will be placed on how the data is able to explain aspects of the structure-property-function relationship of the materials.

1.8.4   Conclusions

This section will bring together the information of the techniques applied in the workflow to display how, when brought together, they create a cohesive, complete understanding of the material, both barnacle and antlers. The limitations faced in the study will be discussed here along with proposed future work. Finally, this section will conclude on how the application of a systemic approach, as recommended in the workflow, enables a comprehensive understanding of the structure-property-function relationship in materials.

2. Literature Review

The story that is materials analysis has been consistently growing as new techniques emerge. Each characterization technique tells its own aspect of this story, and it is not until the information from each technique is assembled that the whole story of a material can be understood. A valuable series of tools for materials characterisation is categorised under microscopy which can offer understanding of the microstructure, chemistry, and crystallography of a material using spectrographic diffraction techniques. Another invaluable technique is mechanical property testing to understand properties such as hardness and modulus, nanomechanical testing techniques such as nanoindentation allow for analysis of features found using microscopic techniques due to its scale. Although each method to obtain this information is used independently, the correlation of information from multiple techniques is an analytical method that migrated from the biological sciences to the field of materials analysis. In materials science, by coupling correlative imaging with nanomechanical property testing, light has been shed on the structure-property-function relationship in both manufactured and biological materials. A systemic approach to sample testing will guide the analysis process and will reduce or identify possible limitations quicker allowing the user to account for such issues, for example, a suitable sample size for comparative analysis. The challenge of correlation across multiple data sets from different sources requires coordination via multiple techniques, once a site of interest is determined for example via X-ray micro-CT, the location of the site for further testing using different techniques is performed using different software linking site locations (14,15), purpose-designed stages and fiducial markers.

This literature review will evaluate innovations and applications of correlative imaging and nanomechanical property testing and how these techniques together are important in "Completing the picture" (16) as this type of analysis is incredibly diverse, and is able to be applied to multiple fields and disciplines hence emphasizing the need for a robust workflow as displayed in the introduction.

2.2   Correlative Imaging

Correlative imaging is the use of multiple, complementary imaging techniques to collect information on a sample, these techniques can be brought together to reveal several characteristics of the material being studied. These techniques can include light and scanning electron microscopy and x-ray micro-CT imaging.

Correlative imaging can probe structural properties and features in a range of scales from micro- to nano- lengths from crack defects (17,18) to crystallographic orientations and to the scale of locating atomic defects in alloys, thus enabling the user to begin their understanding of how the material would perform (16). This has been applied to purpose-made manufactured materials (7) and to biological materials (3,19) to further increase understanding of the multi-functionality of the multi-scale hierarchical structure and interactions that are seen in the complexity of biological materials (20).

2.2.1   Light Microscopy

Light or optical microscopy is commonly applied in biological investigations and materials science and is often the first step in materials analysis. With a workflow in place, a successful first step in materials characterisation gives grounding to further techniques to be applied. Light microscopy is able to provide an overview of the microstructures present within the sample, thus providing initial insight into the structure-property-function relationships in a material (21). Light microscopy allows for viewing of features down to approximately 0.2 μm with a magnification limit of up to 1000 times (22) allowing for this technique to locate regions of interest on a sample surface to improve reduce the time required to locate desired regions on further techniques such as SEM or nanoindentation.

In materials science, due to the thickness, an opacity of the materials reflected light microscopy is used. In this type of light microscopy, the illuminating light reaches the sample surface. At the surface some light may be absorbed or reflected, the light that reaches upward is captured by the objective lens according to its set level of

magnification. Once through the objective lens, the light passes through a partially silvered mirror. The resulting rays of light enter the tube lens which forms the sample's image at the plane of the fixed diaphragm opening in the eyepiece. It must be noted that light microscopes that utilise reflected light the objective has two purposes. For the light going toward the sample, it acts as a well-corrected condenser, due to its consistent alignment. Its second purpose, for the light reflecting off the sample, it serves as an image-forming optical system as normal for an objective, projecting the reflected light that carries the image of the sample surface to the eyepiece (23).

2.2.2   Scanning Electron Microscopy

Scanning electron microscopy (SEM) is a long-standing important tool in the micro- and nano-characterization of many types of samples is a range of different scientific and industrial fields (24), thus providing valuable information when correlating with multiple imaging techniques. This microscopy technique utilises a beam of electrons that interacts with the surface of the sample and produces different types of electrons. The types of signals that are created when the electron beam infringes on a specimen surface include secondary electrons, backscattered electrons Auger electrons, characteristic x-rays, and photons of various energies. These signals are taken from specific emission volumes within each sample which then can be used in the examination of properties such as the composition of the sample, its surface topography, and crystallography. In SEM the signals of greatest interest are the secondary backscattered electrons, this is so as they vary across the topography of the surface. The secondary electron emission is confined to a volume near the beam's impact area, this allows for images of a relatively high resolution to be produced (25). The x-rays produced can be analysed by either energy dispersive (EDS) or wavelength dispersive (WDS) detectors to allow for qualitative and quantitative information to be obtained about the elemental components of the sample.

As SEM evolved to its current standard it has become both competitive and complementary to the capabilities that are on offer by other microscopes. It can offer equal use and image interpretation to that of a light microscope while also providing a significantly improved depth of field. However, SEM does lack the 3D sectioning abilities of scanning beam confocal microscopes; it can however provide information

that cannot be obtained on light optical instruments and the resolution is ultimately far superior. Modern SEMs have spatial resolutions in the nanometre range making them directly comparable to Transmission Electron Microscopy with the advantage that the sample does not need to be made thin enough to transmit electrons.

A commonly used accessory of SEM is Electron Backscattered Diffraction (EBSD), it is used for characterising the crystal orientation and microstructure of a material and is thus applied to numerous fields to aid in further understanding new and existing materials. EBSD's major strength lies in looking at localised features or non-homogenized samples, as a technique it can provide excellent phase discrimination when used alongside EDS.

In EBSD, high energy electrons from an electron beam will interact with an angled crystalline sample [26]. Of the electrons that are diffracted those that satisfy Bragg's equation for diffraction depict conical trajectories for individual lattice planes. These form a pattern, known as a Kikuchi pattern, that is detectable on a fluorescent screen. These patterns created by the diffracted electrons are characteristic of the structure and orientation of the crystals within the point they were generated in the sample. Bright spots on the patterns where bands intersect correspond to zone axes [26,27]. Therefore, the patterns of the diffracted electrons can be used to determine; the crystal orientation, and the difference between different crystallographic phases, as well as to characterise its grain boundaries and provide information about the localised crystalline pattern.

When the electron beam is scanned, in a grid formation, across a polycrystalline sample and the crystal orientation is measured at each point, the final map produced shows grain morphology, boundaries, and orientations. Another use of this data is to show the preferred orientation which is the texture within the sample. EBSD is able to provide large amounts of data allowing for a complete quantitative representation of a sample to be determined [27]. Figure 2.1 shows SEM data on barnacle plate and the ala region obtained by Mitchell [3].
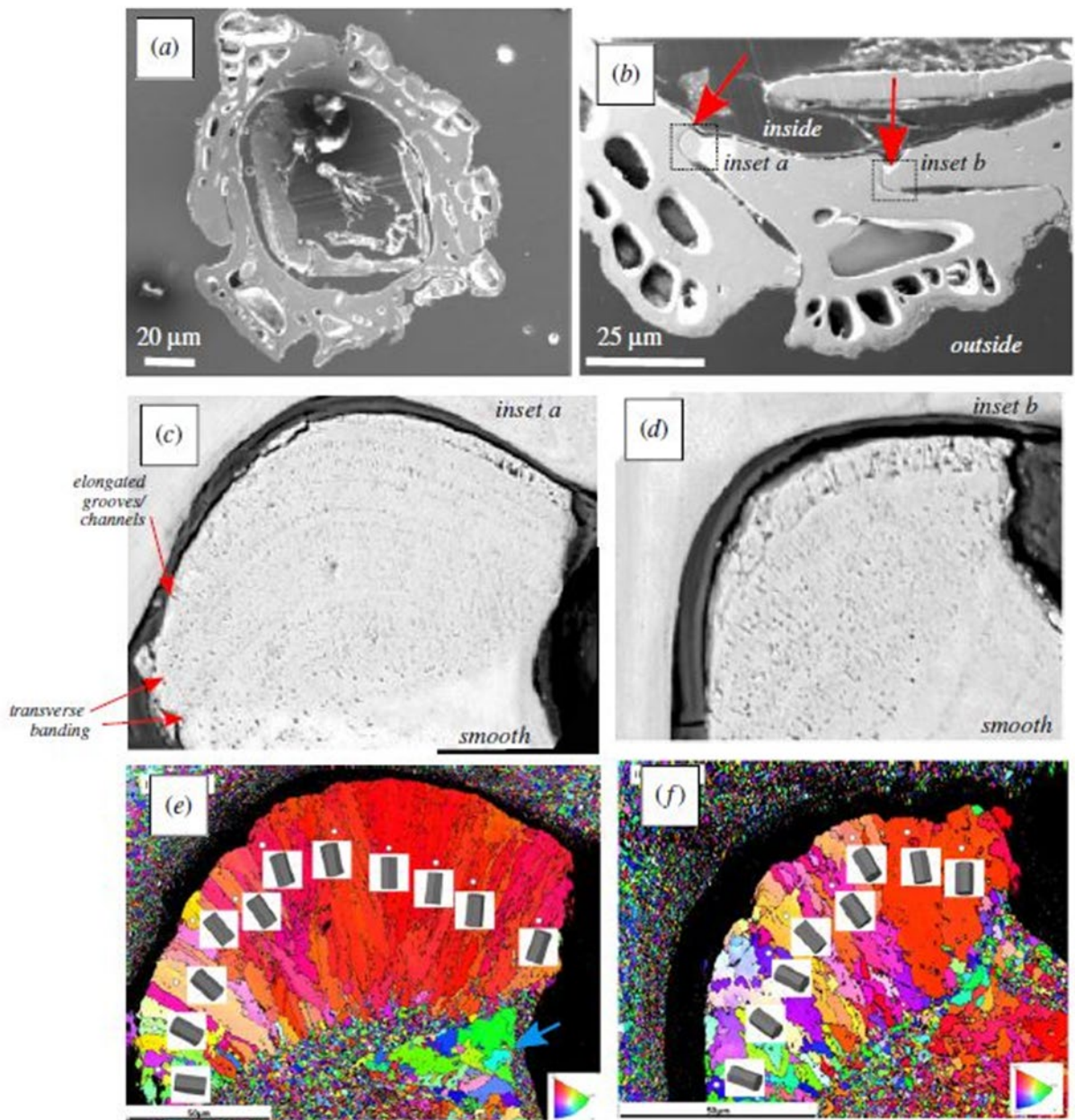
Figure 2.1. SEM imaging and EBSD displaying the crystallographic structure of the barnacle section and ala. (a) SEM image of an individual barnacle section created by mechanical polishing. (b) Three interlocking plates with the ala highlighted by red arrows. (c, d) Magnified images of two alae in image b, they show the microstructure, transverse banding and perpendicular elongated grooves or channels at the tip. (e, f) EBSD maps of ala shown in c and d, the elongated grain orientations are located at the tip of the ala, and granular grains behind this region and on the adjacent plate. Blue

arrow illustrates inside edge coarse grains. Elongated grains appear to correlate with the porous area of the ala. Taken from (3).

2.2.3 X-ray Micro-CT

X-ray micro-CT allows non-destructive visualisation of the structure of materials. In materials science, it is used most commonly for porosity analysis and the location of faults within manufactured materials (28). X-ray micro-CT is used in the analysis of biological and natural materials to non-destructively explore the existing hierarchical structure that exists within (29). To obtain this information from both natural and biological materials the samples must undergo as little interference as possible to prevent damage to the internal structures (e.g., cracks from pressure in sample mounting or shrinkage from dehydration).

The ability of x-ray micro-CT to observe the 3D internal microstructure also determines the suitability of the sample for testing in nanoindentations as the presence of subsurface voids will reduce the modulus values for the region depending on how close the void is to the surface.

The procedure for x-ray micro-CT involves placing the sample in the path of an X-ray beam emitted from the source. The X-rays will pass through the sample, and some will be absorbed into the sample and those that transmit through will project an image onto the scintillator detector. During the scan, the sample will be rotated around a single axis and imaged at multiple different angles, this is shown in figure 2.2. The sequence of images captured is then "back-projected" to enable reconstruction of the absorption or x-rays at each point within the volume of the scanned sample (30–32).
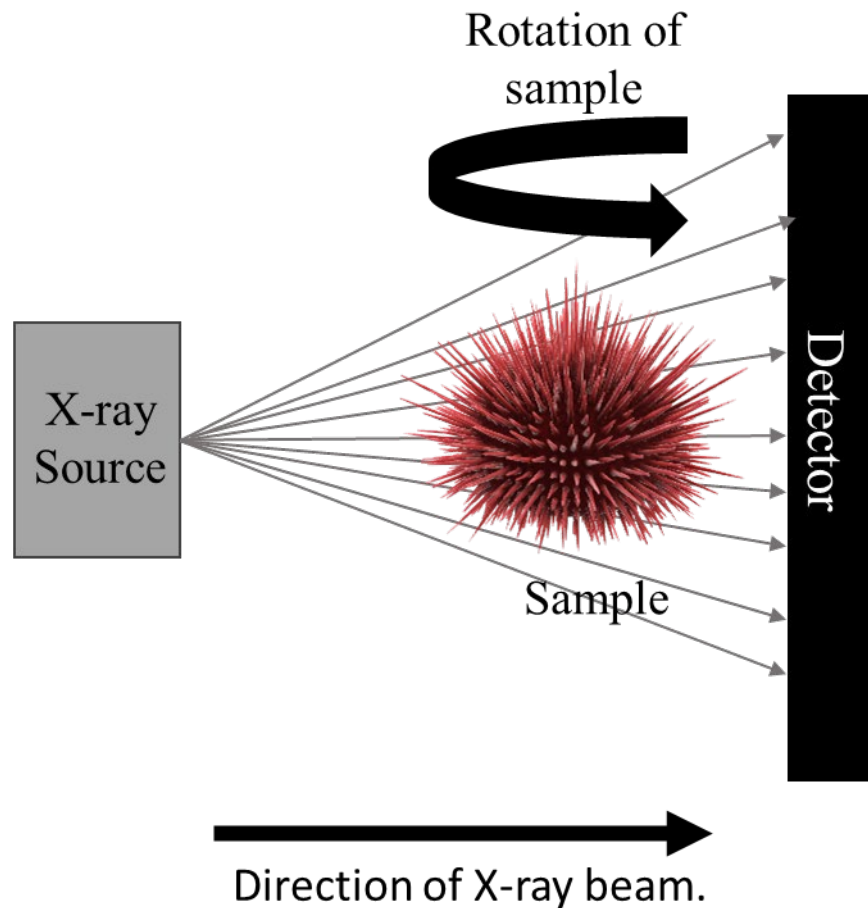
Figure 2.2. Diagram showing the process of X-ray CT scanning using a lab-based system.

Different x-ray facilities will have different requirements for size whether they be lab-based or synchrotron systems with the latter being able to reach finer resolutions. This is due to the electron beam generated in a synchrotron system being able to generate high-brilliance x-ray beams with narrower band widths at selected energy (31).

X-ray micro-CT has long been established as a valuable technique for evaluating the diverse range of mineralised animal tissues such as shells, teeth, and bone (31,33). This is due to the issue any medical problems are related to malfunctions of hard tissue such as in osteoporosis where the bones will appear with lower density (34), this lower density tissue will allow more x-rays to pass through than in healthy tissue.

With such interest in tissue such as bone, the internal microstructure has been studied to develop a better understanding of how the internal architecture distributes strain on loading (35). An incredibly interesting bone tissue used as an analogy of human bone for studies is the deer antler, this is so due to its ease of access and availability for testing as in most species they are shed once a year as well as researchers advocating the potential for antlers to be used as bone xenografts (36,37). The internal microstructure of antlers has also become of interest in applying to the design of a fenestrated network-particle structure with improved wear resistance, thermal properties, and wear resistance due to the internal structural support inspired by red deer antlers (38).

Ceramic matrix composites (CMT) are a classification of materials having high specific-strength and specific-stiffness and is able to withstand prolonged exposure to extreme thermo-mechanical- chemical environments. Such properties have made this material group ideal for application in improved designs for high-efficiency gas turbines and space vehicles for hypersonic re-entry. The manufacture of this material requires multiple repeated steps to decrease the natural porosity of the matrix. The application of X-ray micro-CT at different stages in the manufacturing process along with quantification of the pores and monitoring of crack formation (a known issue in the manufacture of CMT), via machine learning segmentation analysis has resulted in a streamlined more efficient process (39).

More recently a greater medical emphasis has been made for x-ray micro-CT. It is well documented that many medical issues arise from breakdowns of hard tissue this includes the calcification of atherosclerotic plaques and osteoporosis. The programme PHOENIX in the UK has recently placed X-ray micro-CT at the forefront of early osteoporosis detection in patients for the reduction of preventable pain, disability and health issues (34).

The range of diversity and applications of this techniques is vast and alone it spans many fields of research. X-ray micro-CT is an irreplaceable technique that is invaluable for the future developments of health, technology, and society as whole. To enable this it keeps developing, and associated techniques such as in-situ mechanical property testing will develop alongside X-ray micro-CT.

2.2.4 Correlative Imaging Conclusion

Correlative imaging can provide a wealth of detail on many sample types across different fields. Including SEM analysis of crack propagation in manufactured materials such as steels is a well-used practice when selecting materials fit for purpose. An example if this in the investigation of the microstructures near a crack after hole-extension tests comparing DP and CP steel. These tests revealed that the major crack nucleation mechanisms in the DP steels was the cracking of martensite and a decohesion of ferrite-martensite interfaces (7,40)

A study by Mitchel R. *et al*. (2019) used correlative imaging techniques to investigate the wall plate joints (alae) of the acorn barnacle which has adapted to life in the high-energy intertidal zones (3). The imaging techniques employed in this study were light and SEM, EBSD, focused ion beam scanning electron microscopy (FIB-SEM), and X-ray micro- CT. These techniques enabled the identification of specific "macro-micro-nano-scale" characteristics of the alae in both 3- and 2- dimensions (3). Upon reviewing the data collected in each individual technique Mitchel R. et al. were then able to assemble the information and discuss relationships that emerged with potential for bio-inspired designs. It was found that the crystallographic orientations on the plates of calcium carbonate differed in orientation based on their location on the plates with them being granular on the main body of the plate and elongated in the alae regions. This study produced 3 hypotheses based on the findings one of which implied that the elongated crystal region may be to contribute to the mechanical properties of the exoskeleton as seen in molluscs (3). The addition of nanoindentation into this workflow will be able to provide further information as to how this contributes to the nanomechanical properties of the alae.

The application of correlative imaging with nanoindentation is not exclusive to materials science only. In a medical setting, the combination of the disciplines: of radiography, vascular surgery, and biomedical engineering has been able to combine nanoindentation with micro-computed tomography (micro-CT) and SEM imaging to correlate the relationship between the radiographic densities with calcification and mechanical properties of atherosclerotic plaques. Research by Cahalane *et al*. (2018) emphasised the clinical importance of understanding the link between the density of the atherosclerotic plaques found in CT imaging and the degree of calcification of

these plaques as they are key contributors to the stability of these plaques and the failure of endovascular treatments for patients (41).

2.3   In-situ Testing

A further application of correlative materials characterisation is to perform the characterisation over time to observe changes in a sample. Using imaging techniques such as X-ray micro-CT to provide 3D sample analyses with a time-lapsed imaging has been termed to be 4D imaging (16) which has seen a growth in applications in materials analysis into crack propagation, fatigue, corrosion, or battery performance (42–44). 4D imaging has gained further standing with advancements made to digital imaging correlation (DIC) and digital volume correlation (DVC) to monitor stresses on or within the material microstructure over time under experimental conditions (45–47). This is particularly useful in failure analysis, which is traditionally carried out post complete failure, performing a time-lapse of a sample under load allows for the determination of the origins of a failure on the samples which translates, for example to the development of components with longer lifespans and more accurate safe life assessments.

For the investigation of bioinspired materials where the internal microstructure or specific crystallographic orientations as are observed with barnacle alae is hypothesised to impact mechanical properties of the region (3), 4D imaging will be able to provide a comprehensive understanding of how these features behave under loading over time. In-situ SEM mechanical property testing techniques take advantage of micromachining techniques for micro-pillar -cantilever testing of single or several grains within a material. Coupling in-situ nanoindentation with techniques such as EBSD and EDS will allow for location-specific testing of crystals in particular orientations or chemically heterogeneous samples (48).

Bone is of key interest for fracture analysis due to medical implications and links to morbidity that occurs when there is failure of the bone particularly in older age groups. Bone fails due to cracks that proliferate through the crystalline matrix. The microstructure of bone is able to stop this proliferation relatively early on which will normally be repaired within the living organism. If bone does fail it will likely be due to two reasons; fatigue fractures whereby small injuries can occur in successive events before there is sufficient time to repair, or, catastrophic failure where the single trauma

has sufficient force to overcome the stopping mechanisms. Lowe *et al*. (49) caried out a study into the effect of indentation damage in murine bone using 4D analysis to develop a detailed understanding of crack propagation in bone using X-ray micro-CT and in-situ indentation with the IntraSpect 360 in a laboratory setting. They incrementally increased the load applied by the indenter per scan until the displacement sensor limit was reached, and the sensor saturated with a reduction in load and a small increase in displacement was observed during the load hold time. During the loading of the samples, they found that there was evidence of plastic deformation below the surface of the bone which has the capability of being a limited toughening mechanism by blunting the crack tip through the formation of plastically deformed regions. Further investigation of the 3D data found that a crack had formed at a 45° degree angle to the direction of the indent which displayed crack bridging, a major mechanism for preventing crack growth in bone. The existence of porous networks in bone affects its mechanical behaviour, however their link to prevention of crack propagation remained relatively unknown. Lowe *et al*. (49) acknowledged that the murine sample used possessed differences to humans in regards that haversian canals were not found in mouse bone, these canals also posses an important role in the controlling crack propagation. Further investigation into these features were able to be conducted via the 4D testing, from which they determined that the interconnectivity of the pore networks themselves may have a strong effect on the reduction of fractures during indentation of mouse bone compared to human bone. However, further analysis would be required as it can be seen that the pores may have a negative effect on the mechanical properties of the bone due to the decrease in the size of the area to bear loading, furthering the argument that more research into the toughening mechanisms present in bone is necessary. They also present the importance of distinguishing between 2D and 3D data. From 2D slices through the indented bone it would appear that the crack would stop at a pore. Knowing a crack is a 3D structure, the full dimensions of the crack can be assessed revealing the more complex story of crack propagation as shown in figure 2.3 (49).
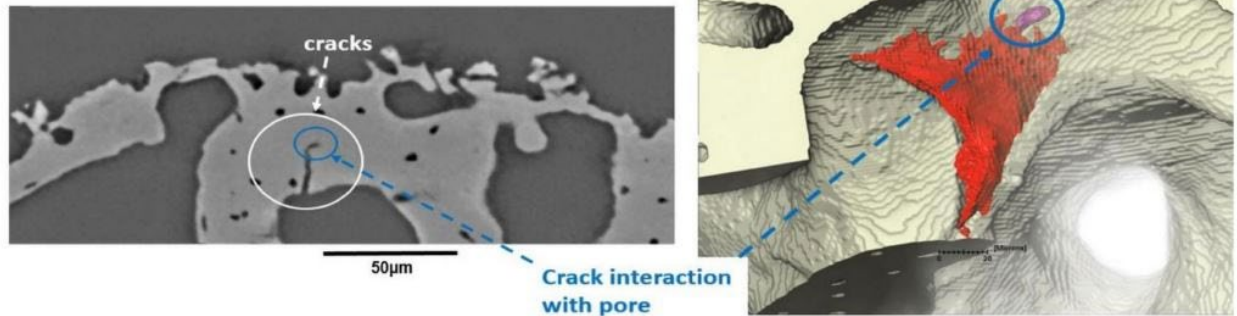
Figure 2.3 A 2- and 3-D visualisation of a large flexural crack which occurred on the opposite side of the indenter tip. This shows how the 2D image can be misleading in terms of crack complexity and propagation as the same crack is circled in both images. Taken from: (49)

Biological materials have utilised the formation alternating layers for many functional reasons. In previous work by Fratzl *et al*. (50) where they analysed the difference in properties between lamellae in biological materials found that a difference in modulus of a factor of 5 is necessary for preventing crack growth (50). North *et al.* (51) investigated this finding in the cuttlefish bone they found that that alternating layers in the middle layers of the dorsal shield and septum of lightweight structure displayed a difference in modulus on a ration of greater than 5 via the use of advanced nanoindentation techniques (accelerated property mapping). To investigate this further in-situ indentation was performed with x-ray micro-CT to evaluate the ability of the layers to absorb the crack energy by inelastic deformation instead of the energy continuing through increasing the propagation of the crack. The ability for the layers in the cuttle bone to prevent crack growth into the inner layers was proven and seen in figure 2.4 as the crack stops at the interface of the layer with a modulus 5 times lower that the layer where the crack originated.
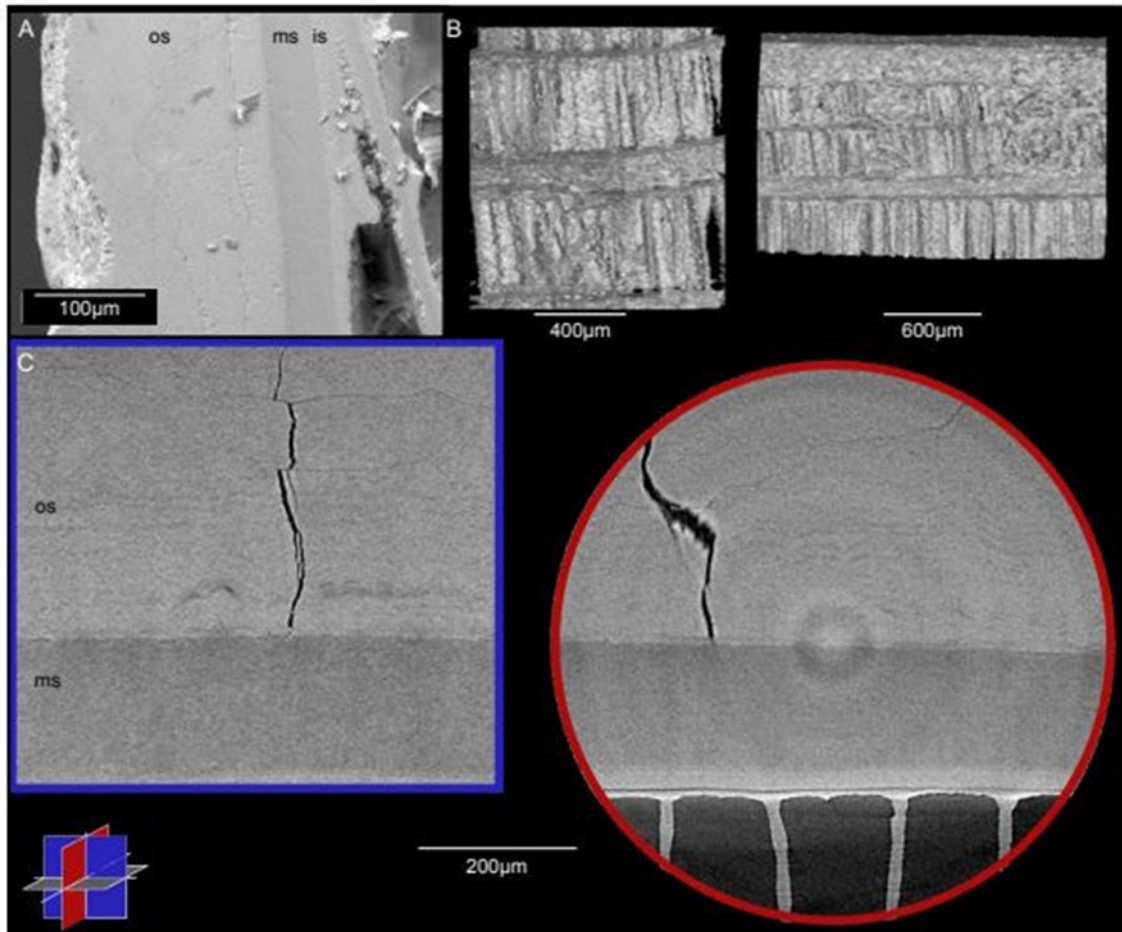
Figure 2.4 (A) Backscatter SEM image of the cuttle bone dorsal shield, identifying a layer of lower atomic mass in the middle shield which exists between two layers of higher atomic mass the outer and inner shield. (B) X-ray micro-CT showing the 3D effect of the failure in pillar structures within a layer and subsequent densification. (C) 2D sliced of an X-ray micro-CT of the dorsal shield, oriented perpendicular to each other, and to the plane of the shield. A crack is extending through the uppermost layer and fails to penetrate into the middle layer with lower modulus, of the dorsal shield. The outer surface of the shield is oriented to the top of the slices. Taken from: (51)

2.4 Chemical analysis

Access to multiple testing methods can be particularly exciting and easy to become carried away with, therefore it is important to keep in mind, the purpose of the tests and what information is necessary in order to ensure the efficiency of the available resources and time, thus the need for an efficient workflow to minimise such issues. Therefore, when planning for analysis it is important to consider the suitability of different testing methods as much attention should be given to the selection of analysis methods as this translates to the selection of a material for components and practical applications (52,53). This can be seen in the testing of the chemical components of some materials.

Some materials can be heterogeneous in nature and sampling of small areas should be done with this in mind, and multiple regions should be tested to minimise errors from this (54,55). A study into the suitability of the applications of different chemical analysis by Olise F. *et al*. (55), compared μ-PIXE, portable XRF in a laboratory setting, SEM-EDS, and XRD to tailings from tin mines and found that as convenient and fast as the portable XRF testing method is that it should be confirmed by another analytic method as, for instance, in this study μ-PIXE was able to provide this due to its suitability for geological analysis (55). Although, it is also argued that with careful consideration of factors that may affect XRF analysis, such as light elements; water and other organic matter that will have a negative effect on the measurements obtained due to the scattering and attenuation of X-rays, a systemic approach alone can provide highly accurate results (54).

SEM -EDS is seen as an important analytical tool in determining the morphological and chemical characteristics of different types of materials. Allegretta *et al*. (24) stated that in many applications of EDS the resultant elemental maps are analysed as an image, which would flatten, and therefore reduce the spectroscopic information in the resultant EDS hyperspectral data cubes which if used can maximise data analysis (24). Hyperspectral data cubes are the results taken from hyper spectral measurement this contains for each wavelength measured from the sample a calibrated spectral reflectance image therefore for any image pixel in the data there is an entire spectral reflectance curve (56). Allegretta *et al*. used soil aggregate samples for analysis due to their complex composition and microstructure and employed their analysis for the

identification if the different phases. They were able to identify a total of 9 different phases in the aggregates and perform contamination analysis and discriminate between different samples based on their compositions, which was not possible with the use of simple EDS images of regions of interest (24).

The correlation of chemical characterisation techniques can be complementary (57). This is observed in investigations of suspected counterfeit artworks whereby individual techniques were able to give sufficient pieces of data, however, upon the correlation of the techniques of XRF, SEM-EDS, FTIR, and synchrotron radiation-induced MA-XRF where each technique was applied to the investigation of a different feature of the paintings such as main paint components, to the binders used in the paints (57).

In the correlation of different techniques, a particular combination may be found to also be suitable for other sample type analysis as seen in a study by Pendleton M. *et al*. (2014) where SEM-EDS and Micro-XRF-SEM was used to analyse pottery pigments, from this work they had also determined that the combination of both techniques would also prove to be useful for the analysis of biological tissues such as bone or teeth (58). Therefore, depending on factors such as sample type and the nature of its composition the techniques used for chemical characterisation require careful consideration.

2.5   Nanomechanical property testing and correlative imaging

2.5.1   Principles of Nanoindentation

Nanoindentation has rapidly become a widely used method for probing the mechanical properties of materials on a nano- and micro- scale. This has been due to many advancements in the instruments used to perform this technique to determine localised properties most commonly hardness and modulus (59). The continuing progress in this technique has resulted in an increased range of applications from semiconductor thin film analysis (60,61), residual stress testing (62,63), to tissues and biological materials testing (64,65).

Nanoindentation is a method by which two surfaces interact, and for over half a century researchers in the field of mechanical sciences acknowledged the fact that the surface contact between materials has a strong relationship with their mechanical properties (66).

When the term nanoindentation is mentioned two names instantly come to mind, W. C Oliver and G. M Pharr (59). Their paper released in 1992 evaluated the then growing, now widely established, technique and outlined the principles for its uses and has since become the standard testing thin films and small structural features (67).

Nanoindentation uses the load and displacement data from a cycle of loading and unloading of a tip of specific geometry; during this cycle the force and depth of the tip are continually measured. The resulting deformation that occurs from loading is assumed to exhibit both elastic and plastic qualities as permanent impressions are formed on the material. The subsequent unloading phase of the cycles infers that only the elastic displacement, of the material is recovered (68).

The indentation cycle produces a very distinct graph displaying the relationship between load (P) and displacement (h), known as P-h curves as seen in figure 2.5, often referred to as the fingerprint of the material. From the curve alone, several important features can be quantified. These features are: maximum load (P_{max}), maximum displacement (h_{max}), the final depth (h_f), contact depth (h_c) and the elastic unloading stiffness (S). S is known as the slope of the upper area of the unloading

curve (*dP/dh*) during the initial stages of unloading, it is also sometimes referred to as the contact stiffness.
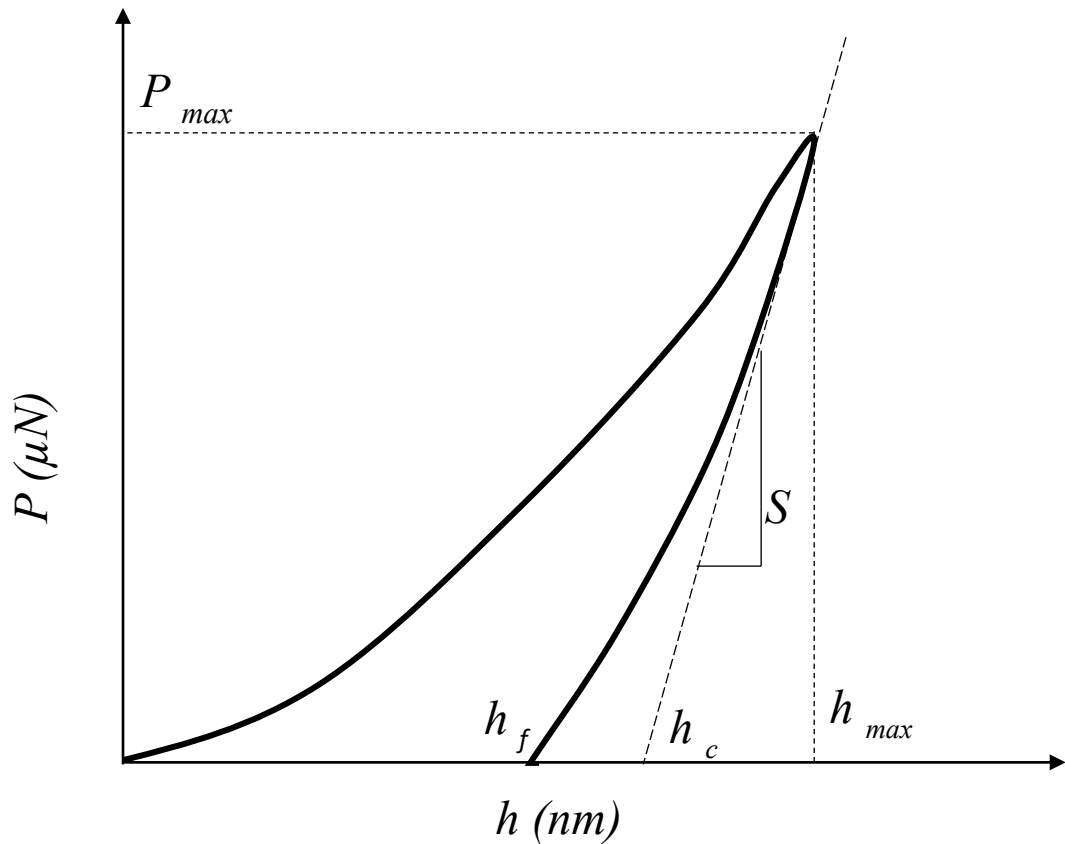
Figure 2.5. An example of a standard *P-h* curve obtained from nanoindentation of a material. From this graph, information can be extracted from graph to extract the material properties.

An issue that arises from this comes from non-linear unloading data. Where the measured stiffness depends on how much data is used in the fit. Oliver and Pharr (59) displayed this using tungsten, where the first and last unloading values are massively different. This is caused by a considerable amount of creep at the first unloading, resulting in the gradient of the initial unloading to be abnormally high (59,68).

The defined procedure to analyse *H* and *E* is taken from the unloading segment of the *P-h* curve. It can be assumed that the behaviour of a Berkovich indenter can be modelled by a conical indenter with an angle that will provide the same relationship between depth and area. There does exists the basic assumption that the peripheral area around the contact site sinks in such a manner as seen in figure 2.6.
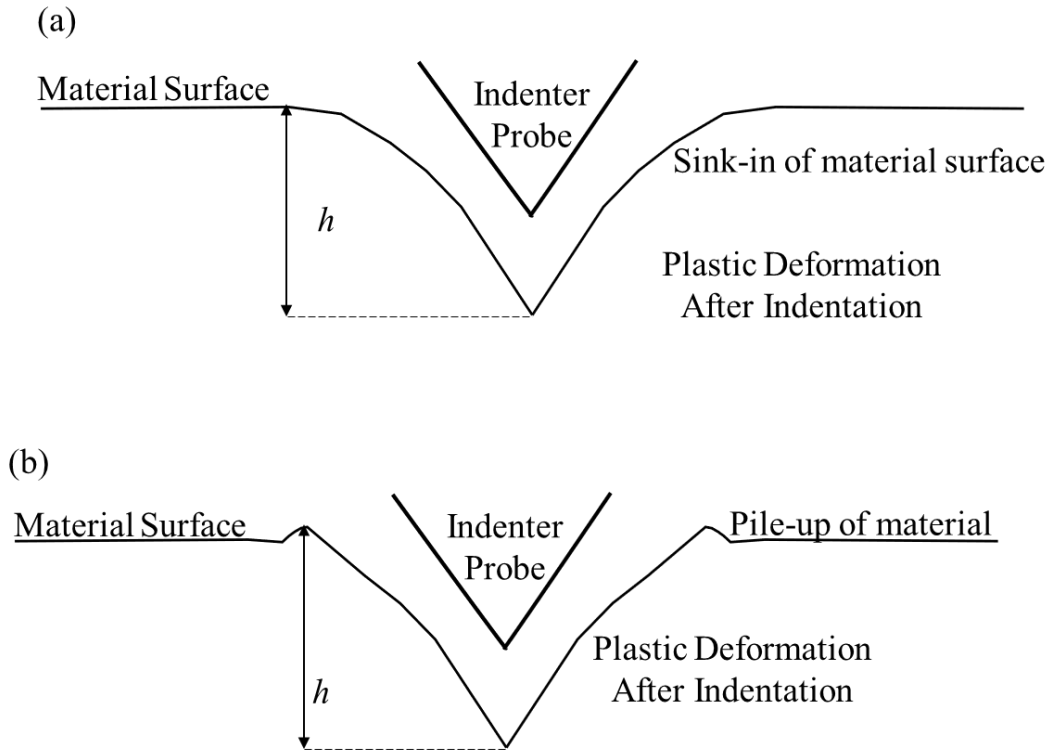
Figure 2.6. Diagram showing the difference in material surface behaviour during nanoindentation (a) sink-in and (b) pile-up.

This assumption can be easily described by models for indentation of a flat an elastic half-space by rigid punches of simple geometry. This assumption limits the ability for the method to be applied as it does not account for the piling of material that occurs at the peripheries of the contact site, which can occur in some elastic-plastic materials. However, assuming that the piling of material is negligible, elastic models have proven that the contact depth sink in, h_c, is given by the equation:

$$h_c = \epsilon \, \frac{P_{max}}{S} \qquad\qquad \text{Eq. 1}$$

Where ϵ is a constant that is dependent on the geometry of the indenter tip. From the observation of unloading curves, they are best approximated by a tip that performs like a paraboloid of revolution and the value $\epsilon = 0.75$ has become the standard value used for analysis.

To calculate the hardness (H) of the material the contact area (A) of the indenter tip must be calibrated carefully by independent measurements so that any deviations from the ideal is considered (i.e. rounding of or contamination on the indenter tip). Once A has been determined, H can be calculated by using the following equation:

$$H = \frac{P_{max}}{A}$$ Eq. 2

The value of E is related to A and S through the following equation:

$$S = \beta \frac{2}{\sqrt{\pi}} E_{eff} \sqrt{A}$$ Eq. 3

Where E_{eff} is the effective elastic modulus which takes into account the fact that elastic displacements occur in both, β is the geometric constant of the tip eg: for a Berkovich 1.05 (69): the specimen with E and Poisson's ratio v and the indenter with elastic constants E_i and v_i. Poisson's ratio is the decrease in lateral measurement in proportion to the increase of length in a material that is elastically stretched. It is to be noted that Eq. 3 shows a general relation that apples to any axisymmetric indenter (i.e., it is not limited to a specific simple geometry). It was initially derived to solve elastic contact only; it has since been shown to apply equivalently to elastic-plastic contact and it is not impacted by any small disturbance from pure axisymmetry geometry.

2.5.2   Tip Geometry

The concepts that exist for an effective indenter tip are derived from observations of finite element simulations of indentations that have been carried out on elastic-plastic materials. These have been carried out using a rigid, conical indenter with a half-included angle = 70.3˚.

As it is well known, that during the initial phase of indentation both elastic and plastic deformation processes occur, at this point the indenter is exactly conformed to the shape of the hardness impression. It is during the elastic recovery that occurs during unloading that causes the hardness impression to change it shape. The resulting imprint is no longer in the exact conformation of the indenter tip and now displays a slight convex curvature. The importance of the observed curvature is that when the indenter is elastically reloaded, the contact area will increase gradually until the full load is eventually achieved. This process is the reverse of what happens during unloading of the indenter as both processes are elastic. The resulting continuous change in contact area produces the non-linear unloading curves. In addition, the pertinent elastic contact issue is, in fact, not that of a conical indenter on a flat surface, it is that of a conical indenter on a surface that has previously been distorted by previous hardness indentations.

The evidence for the curvature that is a result from an indentation was provided by Oliver and Pharr (68) where they displayed topographical images of a Berkovich indentation in fused silica. Their images were obtained from scanning the specimen laterally under the indenter tip with a very light load so that tip contact was maintained. The result was a 3D image and cross section which clearly displays the curvature in the faces of the indentation (68).

The mathematical model of the unloading curve can be inferred by the introduction of an "effective indenter shape." The shape of an effective indenter is that which produces the same normal surface displacements on a flat surface that would be produced by a conical indenter on the unloaded, deformed surface of the hardness impression. From this it can be found that the shape is described by the function:

$$Z = u(r)$$
<div style="text-align: right;">Eq. 4</div>

Where: $u(r)$ is the distance between the conical indenter and the unloaded deformed surface and r is the radial distance from the centre of the contact area. Therefore, if the shape of the deformed surface is known, the function $u(r)$ can be then be determined and the "effective indenter" can be constructed (68). It has been verified that constructing the effective indenter using this method gives an accurate representation of the unloading data. However, the shape of the effective indenter is complicated, and depends on the elastic and plastic deformation features of the material.

From Tabor and Stillwell's studies (59), several important observations were made including in the studies concerning the shape of the hardness impression after the indenter was unloaded and the material elastically recovered. This experiment displayed that, in metals, the impression formed by a hardened, spherical indenter retains the spherical shape, however the radius of the impression is greater than that of the indenter. Also, impressions formed by a conical indenter will, as with the spherical indenter, remain conical but with a larger included tip angle (59).

2.5.3 Applications of nanoindentation and correlative imaging

Biological materials such as bone and nacre are known for their stiffness and toughness, which arises from their structure which from correlative analysis, X-ray micro-CT, light and SEM, has been found to exist in a fully optimised hierarchical structure from the nano- to the macro-scales. The lamellar that exists in cortical bone are comprised of fibrillar units which are aggregated into laminate sheets that surround the haversian systems. This lamellar structure has a dramatic effect on the fracture toughness of the material. These lamellar structures induce crack deflection at weak interfaces or through alternating hard and soft layers with a difference in hardness of at least five times (50). Bone is known as a time dependent hierarchical biological material and has been studied in multiple length scales including testing techniques such as compression and torsion testing. Nanoindentation has been able to probe the time dependent nature of bone and the information obtained when applied to finite element modelling agrees with larger scale materials testing methods (70).

This correlation of multiple imaging techniques with mechanical property testing has led to developments in material manufacturing going on to recommend that if a tough multilayer material with a brittle base is required, the designing process should include that it is layered with anther material with a hardness five times lower than the brittle material.

Chen *et al.* (71) correlated transmission electron microscopy (TEM) with TEM-energy dispersive spectroscopy (TEM-EDS) and nanoindentation to investigate the relationship between microstructures and nanomechanical properties to evaluate the suitability of alloys used in nuclear reactor materials as the irradiation assisted corrosion is known to promote stress crack initiation and formation. These cracks have been observed to easily penetrate materials that have been embrittled by neutron irradiation and thermal ageing. By correlating these techniques Chen *et al.* compared newly developed alloys to determine the suitability of the radiation tolerant material for long-term performance. They also state that by the correlation of these techniques to evaluate how the crystalline structure changes impact features such as hardness and creep further improved materials can be developed. This study then expressed the possibility of missed features in the irradiated samples as the strength of the unirradiated sample remains unknown (71). The recommended workflow of this thesis

recommends that samples are tested from the 0 state, i.e.: before heat, time, or in this instance radiation exposure. Although it is understood that availability is a major factor of this sample type prior planning via the workflow will recommend that this is sought after earlier on in the process.

The semiconductor industry continues to develop holding great potential for improving the performances of its different applications such as in flexible, and transparent electronics, photovoltaics, and sensors (72). To ensure these devices are suitable for their purpose they undergo rigorous testing using multiple techniques to probe the mechanical properties of the devices such as scratch testing and pop-in events (73) that can be performed in-situ SEM where the reaction of the materials can be observed in real-time for analysis (74,75). As new developments continually arise to combat issues such as the cost of manufacturing on a large scale of semiconductors new methods can have an impact on features such as crystal growth on the thin films (76).

With such growth in diversity of applications of each method great strides have been made in ensuring the suitability of each technique. This can be of note, particularly, in nanoindentation. The initial foundations and development of the technique was based on hard materials (77,78) but as the need to apply the technique to a wider array of materials the issue of nanoindentation in viscoelastic, time dependent, materials had arisen. The goal of being able to characterise this type of material is as for hard materials, understanding how it will perform in its intended application. The properties to be understood for these materials are how it will respond upon complex loading environments or to determine the stress relaxation modulus and creep compliance function. Over the past few decades significant research has been carried out in order to make the technique viable in the fields of natural and manufactured biomaterials, multiple polymer applications (functionalised surfaces and thin films), hydrogels, fuel cell membranes, thermoplastics, vulcanised rubber and microfluidic devices (78).

2.6   Accelerated Property Mapping

The further development of nanoindentation has not only led to in-situ testing for X-ray micro-CT and SEM, recently, brought to light is the ability to perform rapid tests in a region of interest in a sample decided upon by imaging techniques, this technique is known as accelerated property mapping (XPM). For example, in EBSD where changes in crystallographic structure is observed, targeting that region specifically for mapping to observe changes in hardness and modulus enables greater understanding on how those local structural differences can impact the properties of the material. Importantly XPM is able to generate large amounts of data for the mechanical properties of these regions in a short time this gives the user an opportunity to perform an array of statistical tests or selected regions including K-means testing, an industrial application of this is the investigation of welds (79).

Testing techniques on the micro- and nano- scales can result the presence of artifacts arising from sample preparation issues as different techniques have specific requirements. This is observed in SEM as samples are required to be conductive, if testing cannot be performed under variable pressure mode the non-conductive samples will need to be carbon coated, this coating can have an impact on techniques performed after SEM imaging such as nanoindentation. This affects XPM as to achieve a higher resolution map shallower indents are performed with a sharper probe such as a cube corner. The coating used on the sample for SEM in this instance can have an impact on the mechanical properties, thus minor details such as a repolishing step between SEM and nanoindentation are necessary to plan as a part of the workflow (7,79).

2.6.1 Map Resolution, Spacing of Indents

The spacing of the indents in a map determines its resolution and be able to reveal the properties of different phases in the material. When determining the spacing of the indents a crucial factor to be considered is that the stress that occurs in the material below the indent is 3D. The 3D stress field decays as a function of distance away from the location of the indent and the boundaries of this zone can be determined by specific stress or strain measurement (79). That is, that the properties will be different from the sample material based on how close they are measured to a feature such as another indent due to the 3D stress field.

When spacing indents, they should not overlap or be placed on the pile-up of a neighbouring indent as this will invalidate the semi-infinite half-space assumption as the actual contact is between the tip and the surface will be significantly from the assumed value (79).

Overlapping of the residual plastic zones between indents results in elevated hardness values as these zones are considered to be cold worked however, the hardness values may be reduced due to dislocations. The size of the residual plastic zone regarding the contact radius of the tip is dependent on the material. This is so as different materials have different plasticity mechanisms. The type of tip used to perform the XPM can also have an effect on the spacing of the indents thus affecting the resolution. The most frequently used tip geometry is Berkovich which has a tip radius of 50 nm has a contact radius to depth ratio of 3.5. A cube corner probe is sharper in comparison to the Berkovich geometry and has a contact radius to depth ratio of 0.7. As these tips have a self-similar geometry, that is that the tip shape has a constant ratio of contact area to depth versus the load applied, the size of the residual plastic zone is proportional to the contact radius and is also reduced by a factor of approximately 5 (79).

2.6.2 Strain Rate

With the benefit of such highspeed testing there exists the drawback of loosing the aspect of setting desired load rates. To be able provide the speed for XPM high loading rates are needed. The loading rate can affect the hardness values obtained from nanoindentation as hardness is strain rate dependent and is fit by a power law relationship by the parameter $m \sim \frac{\partial \ln H}{\partial \ln \dot{\varepsilon}}$ where $\dot{\varepsilon}$ is the strain rate (79). This effect is also dependent on other factors such as the tip shape, and type of material being tested. The strain rate for nanoindentation is defined proportionally as the rate of displacement of the probe in the sample over the total indentation displacement (79).

$$\dot{h}/h \qquad\qquad \text{Eq. 5}$$

$$\frac{1}{2}\dot{P}/P \qquad\qquad \text{Eq. 6}$$

As this is a power law relationship, that is where a change in the instance of XPM rate of loading will give rise to a proportional relative change on another quantity, hardness, which is not dependent on the original size of the quantities (80), The value m can range from 0.001 to 0.1 in crystalline materials thus it will correspond to a shift in hardness between 0.4% and 37% compared to single indentation testing (79).

When considering the use of XPM there is much more that can have an impact on strain rate sensitivity when considering the whole complex scenario. This is that strain rate sensitivity is affected by the main mechanisms of deformation and can be strongly affected by variables that can either help or prevent them. This includes the effects of temperature, crystallographic orientation and grain size. The existence of ultrafine grains within materials can cause high strain rate sensitivity due to the dominance of grain boundary diffusion mechanisms. For several material classifications the effect of strain rate sensitivity has been found to be insignificant.

2.6.3 Correlation with EBSD

Correlation of XPM with methods such as EBSD allows for understanding how localised crystal structures impact the local mechanical properties. Building on the key structure-property-function relationship necessary for evaluating materials.

A study by Chang *et al*. (2021) aimed to characterise the heterogenicity of hardness in a s ample with a complex microstructure with multiple phases, CP800. They applied XPM successfully by careful compromising between the map resolution and strain rate sensitivity factors to achieve a map showing the hardness variation in a scale suitable to correlate with EBSD maps of the material by matching up of phase boundaries to determine the phases responsible for faults (7).

2.6.4 Scanning Probe Microscopy (SPM)

SPM is seen to be a revolutionary technique in nanoscience which has been widened to a range of different fields, including materials science. SPM uses the sharp probe, e.g., Berkovich or cube corner, to physically raster across the surface of the sample in a predefined area, often selected using light microscopy. This technique allows form information such as the topography of the region to be captured with nanoscale resolution (81).

The probe is placed in contact with the sample surface and rastered across in a predefined direction under a very low load. Horizontal or vertical and is able to capture a range of different resolutions of the topography. The larger the are scanned and the higher the resolution will increase the length of time per scan.

2.7   The sample

The application of these techniques and their respective preparation methods can each have an impact on a material, this is mostly observed in biological materials due to their nature. Therefore, consideration of the demands of the techniques and of the sample itself must the thoroughly considered when performing tests.

An example of sample type suitability for testing procedure is that to ensure that SEM images produced for analysis are consistent and of a high standard a major factor to be considered is sample preparation. Volatile samples are not tested using SEM as they can compromise the vacuum and put the electron source at risk of contamination. Biological specimens, foams, emulsions, and food systems (as examples) contain gases, water, and oils within them. This requires such samples to undergo preparation techniques such as chemical fixing, alcohol dehydration, freeze-drying, and critical point drying. Samples that have a high liquid content are prepared for SEM analysis using cryogenic techniques and performed using cryo-SEM, this can ensure that the sample remains solid during the testing procedure. Another important factor to consider with sample preparation is the conductivity of the specimen. Biological samples need to be made conductive prior to visualisation in the SEM, this is done by coating the sample in a conductive material.

SEM analysis on a non-conductive sample can result in the charging effect as electrons cannot flow through the sample this effect can occlude observable microstructural features in a region of interest. This will cause difficulties in locating these areas in other techniques such as on nanoindentation.

2.7.1 Hydration State

Another common issue when applying multiple techniques to a biological sample is the hydration state as commonly in nature these structures are considered living and exist in a wet environment.

When testing biological samples to develop a better understanding of how the material functions in its natural environment it is important to consider the hydration state of the material. An example of this is seen in bone when the tissue is performing its regular function it is in a hydrated state in the organism. Antlers are bone that exist on the exterior of the body, during its growth phase it has a rich blood supply and is covered by a velvet layer which is shed before its use. Studies into the hydration state of antler when used for its intended purpose (combat) found that antler is as dry as possible at the point of use. This was confirmed as experiments into the loss of water by weighing antlers that had been removed from red deer at different time points after the velvet had been shed. Antlers in their dry state shows excellent mechanical properties for its use in combat. It can absorb shocks from initial clashing of antlers as well as having a relatively high modulus of elasticity and bending strength to prevent the tissue from bending too much or breaking during the pushing that occurs in their combat. Hydrated antler will not be suitable for fighting as the modulus is so low that it would bend and become distorted (82). Although antler is bone, if the mechanical properties being investigated are the properties that it exhibits when used it should be tested dry unlike internal bone tissue which should be tested in a hydrated state.

Hydrated testing can be achieved by soaking the sample in a suitable solution (phosphate buffered saline or Hank's solution) (83) prior to testing, the sample surface must not have a residual film of water as this may interfere with the optical focus. Testing should be performed in a suitable time to prevent drying over time. For Bruker Hysitron indenters a fluid cell with a specialised tip can be used to maintain a hydration balance in the sample.

The importance of hydration state is observed when testing of bone samples from an endoskeleton. The percent mineral content of this type of bone is, in weight, 65% the organic phase content is 25% with 10% of the composition being water, showing that

water is a major component. The water molecules exist between the collagen molecules and when dehydrated the spacing between the collagen molecules is reduced thus causing the mineralised lamellae to contract. This contraction occurs more in the perpendicular direction than the orthogonal direction to the lamellar boundary. This reduction in spacing of the collagen fibres results in an increase in bone modulus and the strength of collagen overall reducing the toughness of the bone (84).

2.7.2   Time Dependent Materials

The classification of a material as a time dependent or viscoelastic material is due to the inherent properties of its structure (85) thus should be a vital factor to be considered in planning nanoindentation tests. Tests can be performed in either a load or displacement-controlled procedure. During nanoindentation the contact that occurs between the tip and the viscoelastic material displays both viscous flow and elastic behaviour simultaneously an not exclusively the elastic behaviour noted in non- time dependent, hard, materials (77). These effects have been observed via the vast volume of creep data obtained from the indentation of polymers (77,86). Testing a time dependent material using a load-controlled test requires the maximum load to be held over a set amount of time through which the change of indentation depth is measured as a function of the holding time of a maximum testing load. In displacement-controlled tests on time dependent material the previously set maximum indentation depth is maintained over a set amount of time and the difference in the load applied during the holding segment is measured as a function of the holding time of the displacement of the indentation (ISO 14577-4:2016).

Nanoindentation *P-h* curves of hard materials will typically display a positive unloading curve with a slope that follows the gradient of the loading curve. For viscoelastic materials using the same loading profile as hard materials will result in a *P-h* curve in which the unloading slope is negative. This is shown in figure 2.7, where plot A represents the indentation curve for a viscoelastic material displaying a negative unloading slope highlighted by the arrow, this is compared to plot B which displays a curve with a positive unloading curve for an elastic-plastic material.
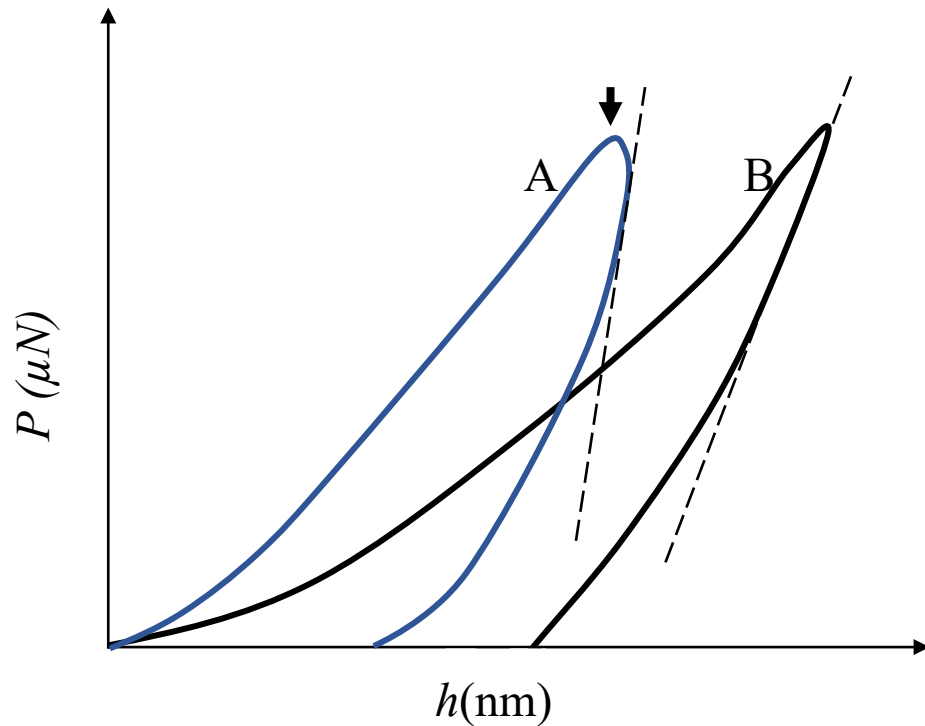
Figure 2.7. Nanoindentation *P-h* curves of a viscoelastic material A and elastic plastic material B. The dashed lines show the slope of the upper portion of the unloading curve, the contact stiffness (S). The time dependent nature of material A has resulted in an increased gradient, which goes on to cause an increased estimation of modulus.

For materials such as asphalt binders it is important to understand their material properties for their practical applications, it was found that to do this, increased holding times at the maximum load is effective in reducing the 'nose effect' of the unloading portion of the *P-h* curves. The loading rates were also an important factor due to lower rates showing increased viscous effects resulting in negative slopes in the unloading curves (77).

Bone is a viscoelastic material of interest particularly in health care as failure of bone in aging populations are a major cause of morbidity (49), nanoindentation measurements of bone are sensitive to the indentation profile this is true for testing in both hydrated and dehydrated states as drying can affect the time constant of the material (70). To obtain reliable results from the unloading segment previous tests on bone have found that when a creep old segment was incorporated into the indentation test profile the quality of the hardness and modulus parameters were improved (87).

2.8 Innovation

The development of new materials suitable for an intended practical application undergoes testing to determine whether they are able to withstand the use for which they are designed. For instance, titanium (Ti) alloys have significant attention in biomedical purposes due to their qualities, such as low specific gravity, high corrosion resistance, and low elasticity modulus enabling them to be suitable for use as bone plates or joints (88–90). As more Ti alloys are developed with non-toxic elements such as Molybdenum (Mo) for biomedical purposes the focus of the materials analysis is on the microstructure and mechanical properties multiple studies have correlated different techniques to elucidate phase transformations, stress release, and differences in mechanical properties between Ti-Mo alloys (88,90–93). The correlations of multiple techniques SEM, SEM-EDS, XRF, and XRD to analyse these new alloys provide a more comprehensive understanding of how the device will perform its intended purpose, in this example ultimately improving the quality of life for a patient.

2.8.1 Bio- Inspiration

One of the advantages of using correlative analysis allows for the elucidation of how established materials such as natural materials carry out their multifunctionality in nature (3). Biomaterials have an incredible advantage of billions of years of evolution and have, through selection, created efficient materials which are assembled under mild conditions from limited resources (94,95). The key to such effectiveness has been determined to come from their hierarchical structure. This hierarchical structure ranges from the nano- and micro- to the macro- scale and significantly amplifies the properties of the components which, individually, are considered weak (10).

This is observed in nacre which comprises of individual units in a 'brick-and-mortar' arrangement and is known for its extraordinary strength and toughness, however, the individual components will not be able to withstand the organism's natural environment on its own. It is this hierarchical arrangement of the micro and nanostructures that gives such properties to inspire scientists and engineers to progress biomimetic processes and inspire fields of materials science such as coatings to be used in biomedical applications (96,97). Along with the recent development of graphene, coupling this new material with the hierarchical structure of nacre has resulted in the development of new body armours and high performance composites with superior mechanical toughness behaviour (98,99).

Creation of the nacre inspired composites have been developed through multiple different techniques as seen in figure 2.8. The protein base layer and the uppermost layer comprising of micro platelets in natural nacre can be replaced with synthetic polymeric matrices and metallic micro platelets respectively in the creation of artificial nacre. The centre layer of natural nacre is composed of chitin nano fibres, which in the manufacture of artificial nacre can be replaced with different multifunctional nano fillers. The synthesis of artificial nacre with the layers displayed in figure 2.8 has been shown to display extraordinary strength and toughness qualities even compared to natural nacre qualities (98).

Aragonite micro platelets	Alumina(Al_2O_3) micro platelets
Chitin nanofibers	Graphene oxide Nano sheets (GO)
protein structure	Poly(vinyl alcohol) (PVA)
(a)	(b)
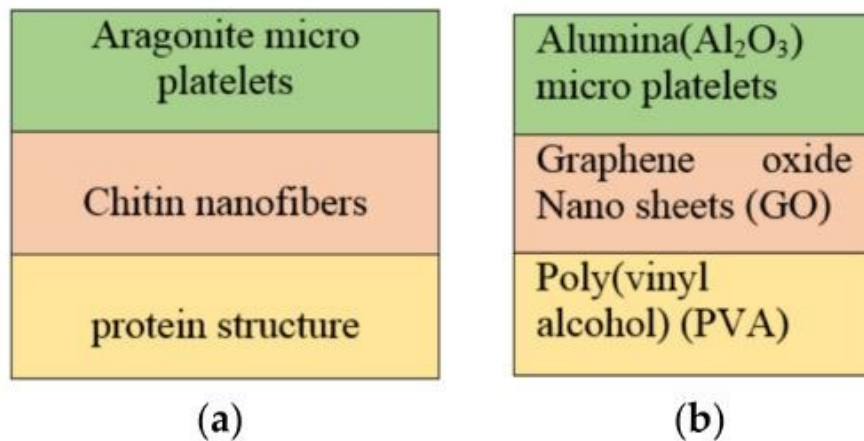
Figure 2.8. Schematic comparing the layering sequence between (a) natural nacre and (b) artificial nacre. Taken from (98)

Recent developments in de novo fibre reinforced composites have been inspired by the multiscale nature of bone in order to amplify the toughness in a balance with strength. The inspiration for studying internal bone is due to the continual loading it undergoes regularly as well as providing large fracture toughness, damage tolerance and self-repairing. There is an added degree of complexity in mimicking the complex structure of bone as seen in figure 2.9. Due to the challenge of creating different arrangements with differing levels of precision. It has been determined that the microscale level is responsible for the largest contribution to its toughness. Of the microstructures of bone, the most studied feature is the Haversian system which has a composite configuration with repetitive tubular units known as osteons that are made of concentric lamella (100).
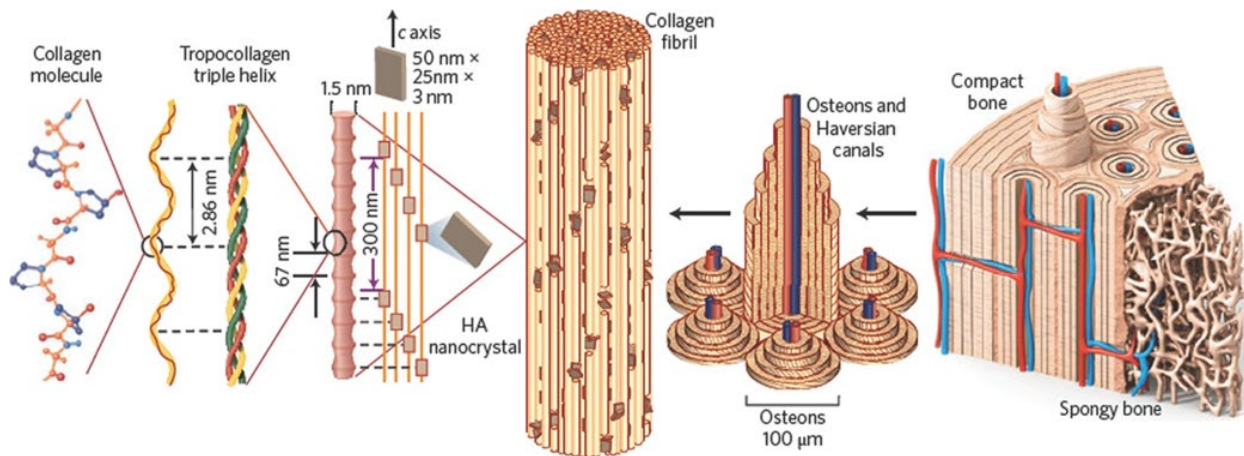
Figure 2.9. The detailed organisation of bone from the macro- to the nanoscale. Taken from: (101)

The osteon of bone is comprised of the mineralised fibrils that have been self-arranged into fibril arrays that scale from 1 – 10 μm. The lamellar structures are planar layers of bone tissue, with an approximate thickness of 5 μ in which the fibrils vary in orientation per individual layer , in a stacked arrangement found in both compact and trabecular bone (102). Figure 2.10 shows the organisation of the lamellar structure of bone with on multiple scales with a schematic to represent the direction of fibrils in the lamellae.

Novel manufacturing techniques have mimicked the structure of the haversian system through use of carbon and glass fibres and an epoxy matrix with bundles of unidirectional glass fibres embedded into fabric to mimic the osteons and the outer sheaths of Haversian systems. This bio-inspired material was able to impact material failure as the cracks deviated its path from a straight line to follow the synthetic osteon curvature. Although the scaling of the synthetic material was larger than a haversian system it was determined that the toughening mechanisms have been correctly mimicked (100).

The study of nature natural materials has resulted in the development of bioinspired products. The development of these products demands a comprehensive understanding of the natural material that inspires the design thus it is understood that many techniques are required to probe these multiscale hierarchical structures to be able to get the full picture of the structure-property-function relationship of these materials. Particularly as these materials can provide appealing to solutions to issues faced in many sectors especially energy and transportation industry.
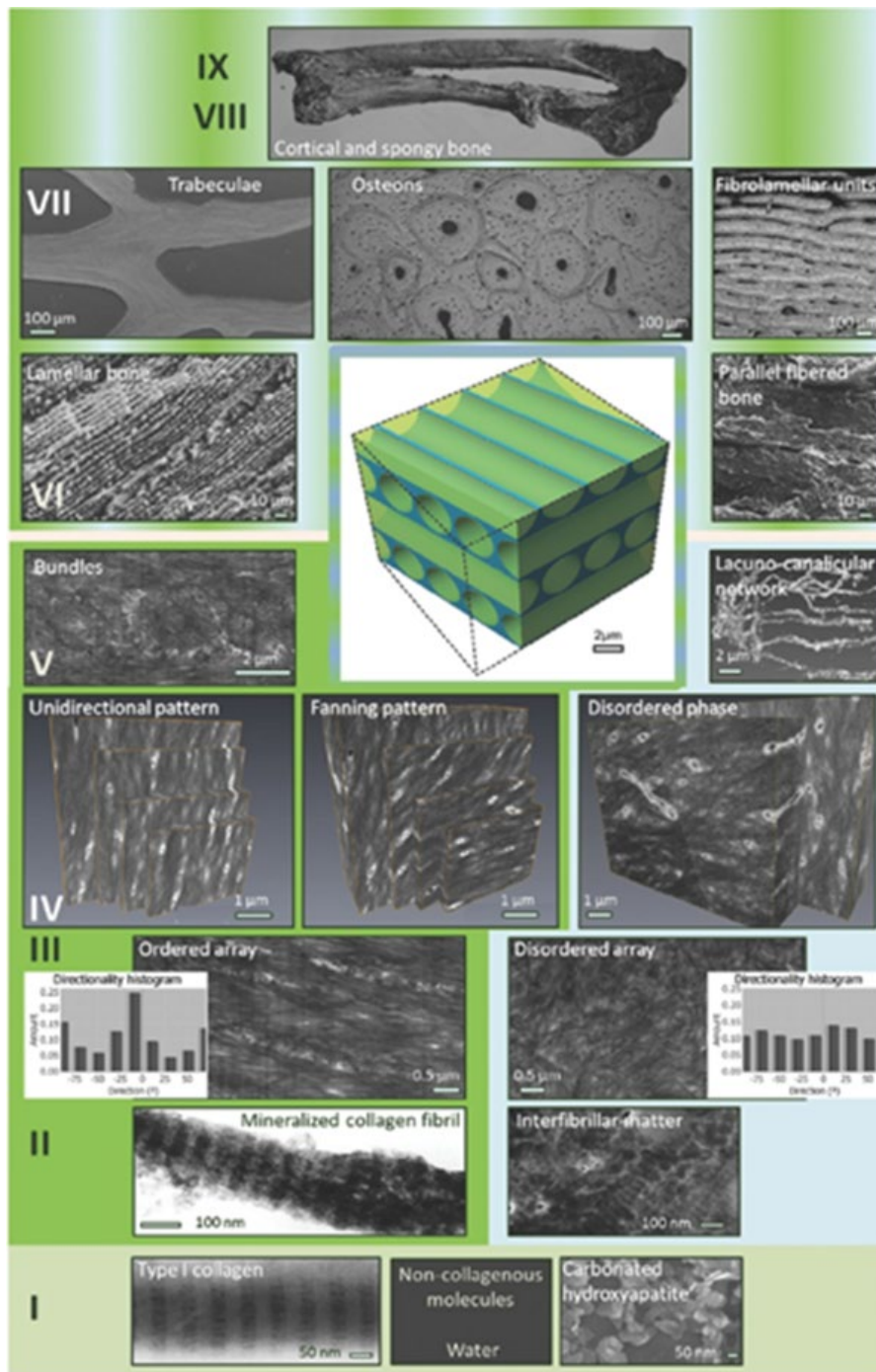
Figure 2.10. Transmission electron microscope images displaying the different hierarchical levels of bone. To visualise the ordering of the material the borders of the images are color-coded: green: ordered material, blue: disordered material and a graded colour scale: both materials are present. Taken from: (103).

2.9   Barnacles

Barnacles are crustaceans that are characterised by their sessile lifestyle in adulthood by attaching themselves to a hard surface which can include other organisms (104). They are commonly seen inhabiting the high-energy intertidal zones. To cope with this extreme environment and the threat of predation, they have adapted over millions of years of evolution. This involved changes over multiple scales from plate structure and composition to the architecture of the exoskeleton (3). The outer shells of different barnacle species have been studied extensively, from crystal orientations of calcite in the operculum, the strong adhesive qualities and mechanical properties of the base plate and the process of biomineralization during plate formation by the involvement the organism's extracellular matrix. Checa *et al*. (105) performed analysis on both the barnacle radii and alae, the manner which they both contact with their adjacent plates and the contact of these regions with the matrix created by the organism through which calcium carbonate diffuses for deposition, their investigation therefore suggests that the growing front are the alae and radii regions, they also performed EBSD into the two regions of interest which also showed similar results to Mitchel *et al*. (3). Mitchel *et al*. (3) found that from previous literature there was little understanding in the manner by which the different levels of structures in the barnacle shell from nano- to macro- scale were linked. They performed this analysis by correlating multiple imaging techniques to discover the multiscale interactions that occur in *Semibalanus Balanoides* (acorn barnacle) which is common on the British coastline (3). They also concluded that the alae were growth fronts which concurs with Checa et al. (107) in their later publication (3,104).

The acorn barnacle possesses a conical shaped exoskeleton that comprises of 6 plates (plate quantities differ according to species) that overlap at joints with a part of one plate over lapping with the adjacent plate these internal overlapping regions are the alae, the external region is known as the radii as seen in figure 2.11. The mineralised plated are composed of calcium carbonate in its calcite polymorph. As the organism grows the exterior shell increases in size to accommodate for its host.

The techniques they applied were, X-ray microscopy, SEM, EBSD, light microscopy, and focused ion beam SEM . Through the application of these techniques, they found that the barnacle exoskeleton was comprised of six interlocking plates. They

highlighted the structural interlocks (alae) which allow for growth while maintaining a seal to ensure safety of the organism. Their crystallographic analysis found that the alae possessed functionally graded crystal orientations, with elongated grains at the outer edge. In addition to the differences in the crystallography they identified the 3D networks of pores only visible at the tip of the ala which are orientating in the same manner as the crystallographic structure. Thus, they recommend that these pores that will normally possess organic matter that influence the biomineralization process (3).
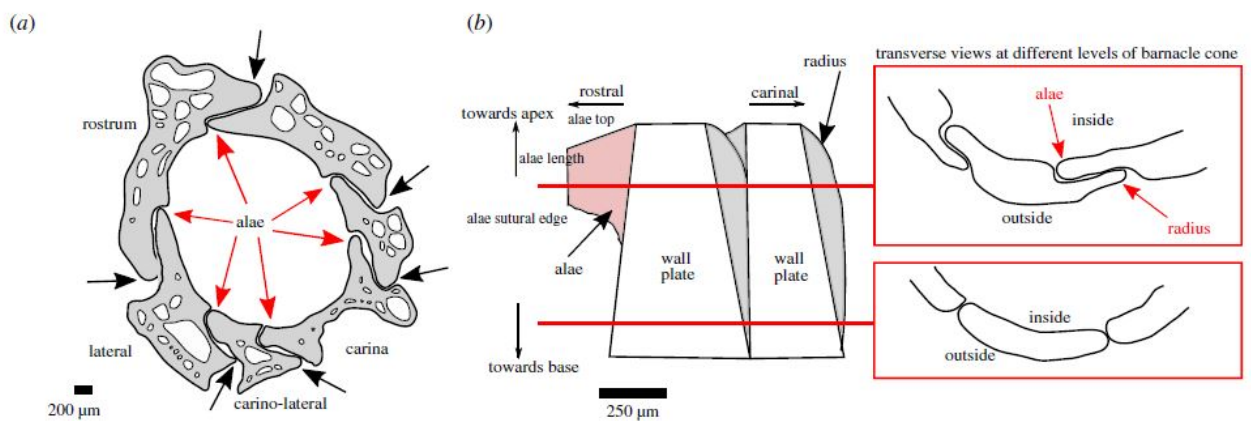
Figure 2.11. The Morphology of barnacle *Semibalanus balanoides*. (*a*) A section through the six wall plates that constitute the exoskeleton. The alae structures are highlighted, (*b*) Longitudinal internal view of adjacent wall plates interlocking. Insets illustrate morphological differences of the ala at different points of the interlock. Taken from: (3).

2.10 Antler

A trademark of most deer species is the magnificent antlers that protrude from their heads. These extraordinary features grow on the male species and are used in the rut as they compete for dominance to mate. The exception to this is the species *Rangifer tarandus* (Reindeer) where the females also possess antlers (36,106,107). Male reindeer shed their antlers after the rutting season in autumn whereas the female reindeer keep their antlers throughout the winter and will use their antlers to defend patches of food against other reindeer and shed them in the spring, after calving (36,108). Antlers have gained interest in bone studies as they have been found to have the greatest work to fracture and impact energy compared to all known bones, to the point that they are known to be almost insensitive to breaking by impact (109).

Antlers have also gained much interest in studies one of the reasons for this is due to their ease of accessibility and their annual regrowth that allows for sequential studies to be performed on the same individual over a period of several years. In addition to this the periodic growth and shedding cycle of antlers is the only example of complete regeneration of large bony structures in mammals, thus sparking great interest in the field of regenerative medicine as it works towards the promotion of regenerating tissue from single digits to entire limbs in humans (110).

2.10.1 Growth

Antlers are organs that are comprised of bone which are grown on the frontal bones of the deer species they ultimately harden and are shed every year (111,112), the physiological cost for their growth is high. The rate at which antlers grow is approximately 2 to 4 cm a day making it one of the fastest tissue growth rates of any animal (12,113) and the fastest growing bones in the animal kingdom, thus making them an ideal model for the study of bone growth and the process of bone mineralization (110). The Growth of antler is accompanied by a form of reversible osteoporosis within the skeleton. This phenomenon is similar to that which has been observed in maternity and lactation of many mammalian species (111).

The annual antler growth and shedding cycle is considered a phenomenon that few other periodic processes compare, as the processes of formation and growth have a greatly increased demand of minerals (114). The internal structures, histology, mineral composition and mechanical properties of antlers are strongly influenced by the environmental conditions of the deer. Therefore, they can be used to compare variation in different factors such as the availability of nutrients in different habitats, the presence of contaminants in the environment with an affinity to mineralised tissue or factors that can result in antler breakages (110).

Growth of antlers requires a modified form of endochondral ossification (111), this is the process by which bone formation occurs by the creation of a cartilage scaffold which is gradually replaced by bone, this form of bone growth is also seen in embryonic development (115). In antler growth, the steady formation of the trabecular bone though out much of the growth phase occurs and a large terminal increase in bone deposition results in the formation of compact bone in the antler cortex just prior to the completion of antler development (111). During the process of growth, the cylindrical pores are orientated along the main axis of the antler, within this framework the primary osteons fill these longitudinal tubes after the deposit of lamellar bone. The mechanical performance at the structural level of the antler is connected to the honeycomb like structure which determines the thickness to the cortex region of the antler (36). Thus, measurement of the cortical region of the antler is important in determining the mechanical performance of the antlers.

The two types of osteons that are present are primary and secondary, the secondary osteons result from the remodelling of bone and are often observed to intersect each other they are described as having a more rounded formation compared to primary osteons. It is important to note that unlike skeletal bone antlers do not undergo loading and experience mechanical force while developing, thus it would appear unlikely that secondary osteons would develop under such conditions. If secondary osteons do develop it is likely due to a process of modelling instead of remodelling. The hyper mineralised lamellar structure that exists around the primary osteons in cervids concurs with the lines of cement around secondary osteons that form after mineralisation. The role of these structures are proposed to be reinforcements by mitigation of the propagation of microcracks (36).

The nutritional impact on antler growth begins in the maternal environment, *in utero* and during and after lactation (the effect of the levels of nutrients supplied during lactation could extend up to two years in the growing deer), this has been found in studies that investigated birthweight of the red deer species and the length of their antlers (116). These studies found that red deer calves that were fed milk with a higher protein concentration or if the lactating mothers had diets supplemented with minerals resulted in an increased spike in antler weight and altered mineral concentrations of their spike antlers, this could be attributed to better milk production resulting in a greater intake of all nutrients. Notable changes in antler mineral compositions, Ca, P, Na, K and Mg were explained by the calf's weight gain to weaning (116). The post-weaning nutritional influences in multiple deer species has been investigated as the length of the initial spike antlers grown by yearlings provides a good indicator for their survival over the winter months as those that grew antlers in their first year were three times more likely to survive than those that did not (116).

The natural diet of reindeer is not able to support this rapid growth, consequently, to supplement the antlers, 20% of the minerals from their skeletal mass is used, resulting in a process that is similar to temporary osteoporosis. This takes place through the spring and early summer during the major growth phases of their antlers (12,111).

A study by Baksi and Newbrey (117) evaluated the effect of antler growth on bone metabolism specifically in female reindeer. For their study, they purchased two female reindeer which they reared on campus, they took rib biopsies in July and January. July was selected as this is the time where antler growth has achieved approximately 75%

of its maximum length, their rationale was that the Ca demand for growth of the antler would be high at this time therefore the endocrine and bone metabolism would be higher. They found that the during the antler growth phase female reindeer undergo bone loss that corresponds to the changes in plasma calcaemic hormones and oestradiol levels. This bone loss is eventually repaired when the antler growth stops (117). This study determined that as with male deer female reindeer undergo the similar temporary osteoporotic and recovery effect annually. However, the study was limited to two female reindeer only, as they were reared on campus their diet comprised of a reindeer feed mix, this does reflect how they would occur in nature. Biopsies were taken at only two intervals; this meant the point by which the osteoporotic effect ends could not be closer determined. Another effect of the two reindeer being reared on the campus is that they would not be calving later in the year, therefore the effect of maternity was not determined.

During the growth of antlers, they are covered in a skin known as the velvet which is different from the skin that covers the rest of the head region. The velvet has a thicker epidermis, the hair follicles lack arrector pili muscles and has in increased number of sebaceous glands. Importantly, it needs to keep up with antler growth there is a high rate of creation of new hair follicles in the velvet. Deer species evolved to shed their living velvet annually, depicted in figure 2.12 before the winter period to prevent freezing of the living tissue that could lead to necrosis of healthy tissue. The cycle of shedding and regrowth may be due to an evolutionary trait acquired to ensure that complete antlers are available each year. However, it had been determined the main reason for the annual regrowth of antlers is the fact that the finished, hard antlers that have shed their velvet used in the rut and the bony structure is considered dead (110).

Figure 2.8. Male reindeer (named Morse) shedding his velvet before the rut exposing the hard bony tissue below that will be dry before use in fighting. Image credits: Hen Robinson use approved by Cairngorm Reindeer Herd.

As finished antlers are composed of dead bone, hard antlers are not able to repair fractures obtained from use in fighting. If the antler tissue were alive during use it would be able to undergo periodic regeneration to ensure that a fresh set of antlers were ready for use every year, however, growth of the antlers will only be achievable if the structures are cast and completely regrown (110). Many studies have been carried out to thoroughly establish the fact that finished antlers are dead bone. This detail will affect the hydration state and thus the mechanical properties of the bone. It was found that water content of antlers at the time of use is equal to the relative humidity of the air (36).

The process of shedding is due to a process of antibacterial sequestration of dead bone, if the antlers were to remain in their current state the junction with pedicle on the skull has been noted to become infected with the possibility for fatal consequences (110). The cycle of antler shedding is different for female reindeer as it is synchronised to their reproductive cycle, via endocrinological regulation by oestradiol, although their antler are fully developed by autumn and winter they maintain their antlers until the spring (36).

2.11 Structure

The internal structure of reindeer antler shows 4 distinct regions, from the outer region towards the centre (i-iv): (i) the outermost region is the sub-velvet compact region, then, (ii) the osteonic bone that composes lamellar compact, cortical, bone, the structure begins to change in the transition zone (iii) to the centre region (iv) of the antler which comprises of trabecular bone (36). These zones are labelled in figure 2.13.
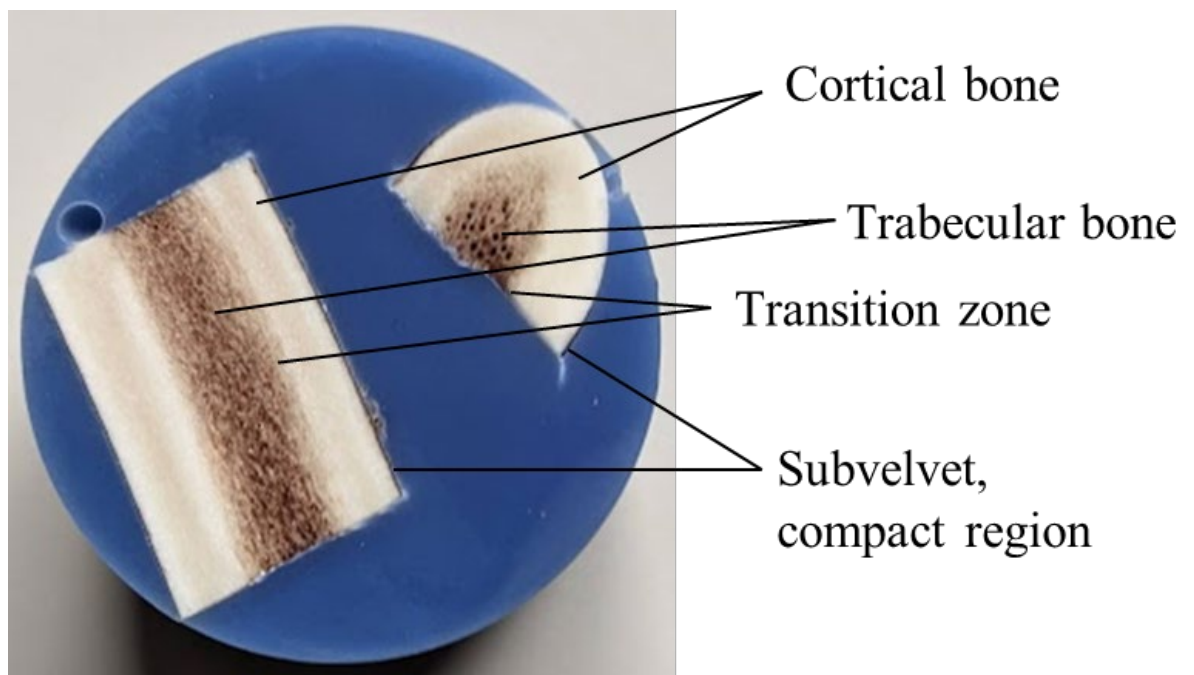
Figure 2.13 Image showing a cross and transverse section of antler labelled with the four histological zones.

The antler cortex is mostly made of primary osteons that are highly variable in shape and may contain more than one vascular canal. Transverse sections of antlers when observed with polarised light the bulk of the wall of the primary osteons will appear dark, showing that the direction of the fibres is orientated in a longitudinal direction. Along the periphery of the osteons the seams that appear bright indicate that the orientation of the collagen fibres are perpendicular to the path of the light (110).

The anatomy of reindeer antler comprises of the burr which connects to the pedicle on the head of the reindeer, the main beam which is the axis of growth of the antler (118) and the multiple tines that extend from the main beam. Figure 2.14 displays the multiples tines that can occur during antler growth for reindeer specifically as different species will have different configurations.

The brow tine extends to the front to the antler immediately after the burr forming a junction with the frontal tine and the main beam which extends towards the back and upward without further tines until near the end of the main beam. At this point multiple tines protrude from the main axis of growth and the main beam extends forward to its terminal outer tip.

Studies have found that the chemical composition varies in different anatomical positions in the antler in a standard range of conditions. This may be due to different parts of the antler having different functions thus suggesting that there will be differences in mechanical properties as the degree of mineralisation impacts on this (109).
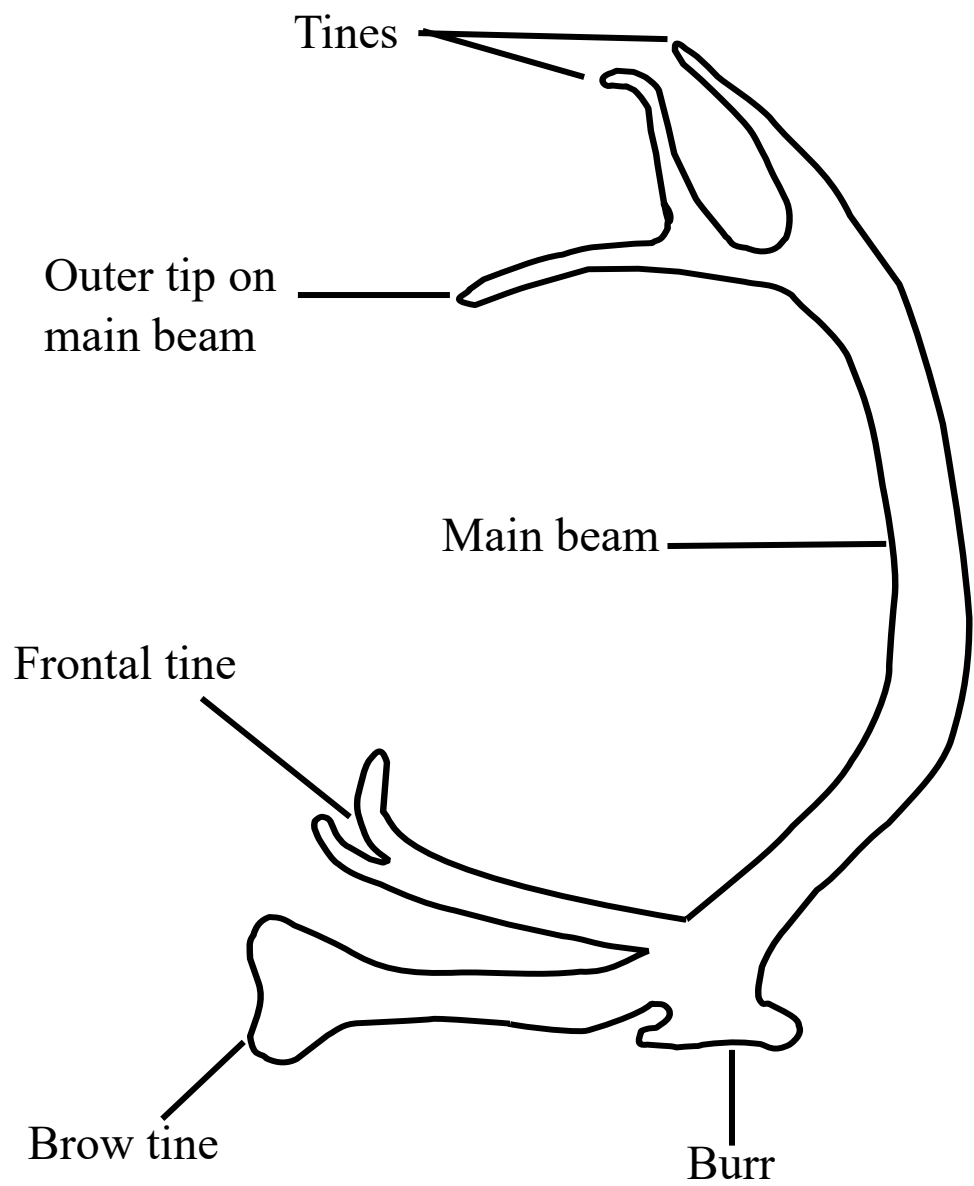
Figure 2.14 Anatomy or reindeer antler, labelled with the observed structures on samples obtained for testing and observed in images provided by the Cairngorm Reindeer Herd.

2.12 Mineral Composition and mechanical properties.

In the world of biomineralized bones, antlers have been found to be the most resistant to impact and absorbs the most energy (110). Studies have found that the modulus of elasticity and strength increases with an increasing mineral content while the work of fracture is reduced (36,110).

 A study (110) has shown that the antlers obtained from three deer species reared in captivity and who were fed the same diet showed that there was little interspecific variation in mineral profiles as seen with Cu but no other trace minerals showed this. Multiple studies (109,113,119–124) have gone on to show that antler mineral composition have been found to be indicators of environmental pollutants that have been absorbed through the diet such variations has led to the surveillance of antler composition in game management (110).

As previously established minerals obtained via dietary means impact on the growth and content of antlers. A study by Landete-Castilljos *et al.* (121) found that a particularly harsh winter causing a reduction in plant growth greatly impacted the chemical composition and architecture of the whole antler and thus its overall mechanical performance, becoming more brittle. They found that there was a 31% reduction in an antlers weight, the cortical region was thinner, lower density, and the main beam diameter was reduced. These structural effects affected the mechanical properties, the absorption energy was reduced by 27% and Young's modulus values were found to be lower at the ends of the antlers. The mineral that has an effect on the mechanical properties of antlers growing after a harsh winter is Mn, as it can increase the absorption of impact energy, fracture resistance and possible also the density of the cortical bone (36,121). Thus, there exists ample evidence that the mineral composition of the antlers is vital to the structure, properties and thus the functionality of the antlers.

The impressive mechanical properties of antlers may depend upon them having the lowest mineral content of all mammalian bones. Studies have shown work of fracture reaches a maximum at 59% mineral content which is that of antlers, after this point the work of fracture falls rapidly. Along the length of the antler from base to the top tines, there are differences in mineral compositions in Ca, P, K, Fe and Zn (110). As the mineral content is different at different points along the length of the antler: near

the base, the mineral composition is 56% thus the work of fracture in this region is greater than the tines which has a mineral content of 49% (109). This is predicted to be due to the fact that the base of the antler is more likely to bend in impact by fighting than any other part of the antler, therefore this region requires as close as possible mineral content to the maximum for work of fracture (109). Work of fracture is a material constant that is independent id sample geometry and the plane-stress or plane-strain transition is found to be dependent on the nature of the material being tested (125).

2.13 Male and Female Antlers

The toughness of antlers from several deer species has been the subject of many investigations across multiple scales from bulk testing to the nanoscale (36). These studies were able to determine multiple factors that have roles in the toughness of antlers, including histological specific characteristics such as, species (and overall antler morphology), and its mineral composition (120) particularly the role of manganese (Mn) in mineralisation (126). A study by Shah *et al*. (12), hypothesised that there may exist a difference in the stiffness between male and female reindeer due to their physiological and behavioural difference. The growth of male and female antlers bears similarities in that minerals from the skeleton are redirected to the antlers. However, the differences between male and female reindeer include the duration that females retain their antlers until spring unlike that of the males, who shed their antlers after the rutting season in the autumn. The females also appear to prioritise the growth of their antlers more than the males, particularly when resources are limited (127). Deer from tropical habitats retain their antlers all year and will use them for fighting throughout the year. A previous study comparing variations in the stiffness of antlers from different species found that antlers from species that retained their antlers to use them to regularly engage in combat (this longer-term retainment is similar to female reindeer) were stiffer than those that were retained for a shorter time (11,128). Shah et al. (130) conducted 3 point bending tests on the samples from male and female reindeer from different geographical locations but did not identify any significant differences between male and female antlers (128).

Due to the differences in antler growth between male and female reindeer, it can be hypothesised that there will be differences in the mechanical properties. Although the previous analysis by Shah (130) determined that there were no differences in the stiffness values, further properties should be investigated (36,128). Comparing the differences between male and female reindeer on multiple scales and using various techniques can unveil any differences between the structure-property-function relationships between the sexes. An added factor not considered was the calving status of the female reindeer, and how this physiological condition may have an impact on the growth and quality of their antlers. The following question had arisen from investigations of previous literature and communication with the herd keepers: Does the mineral provided by the lactating females, which is vital in calf survival, come at a sacrifice of their antler quality? This will be discussed in detail with the support of the results obtained.

The correlation of imaging techniques and chemical analysis with nanomechanical property testing will develop a greater understanding of the structure-property-function relationship in reindeer antlers and distinguish where the difference in growth between the male and female of the species results in material property differences.

2.14 Conclusion

Having the whole picture of the characteristics of material via correlative analysis of either biological, natural, or manufactured material is vital for progressing the understanding, and future developments. As demand for new materials continues to arise, future advancements will be guided by testing methods, from chemical compositions and deliberate crystallographic formations within the material to multiscale hierarchical structures created through techniques such as additive manufacturing. The performance of these materials in their practical applications is a key feature to keep in mind. As these materials will go on to be used in many different applications from replacement joints which can greatly impact the quality of life of a patient to semiconductors used in solar cells. These techniques are not only exclusive to materials science, but such correlative studies have been applied to the field of medicine for example to determine the associated risks of mineralised atherosclerotic plaques for a patient. It is not until all the pieces of the picture are put together that a

true understanding of the material is reached. As advances in technology continues to be made in materials characterisation, from new methods to progresses in equipment development materials characterisation techniques will be woven into the correlative workflow in the future.

3 Methods

Two different, mineralised, biological sample types were obtained for analysis, the acorn barnacle exoskeletal shell and reindeer antlers. The recommended workflow is able to be tailored to the unique demands of each of the samples to provide insight into the structure-property-function relationship of these materials.

The sequence which these tests were performed in the workflow are important as preparation may impact following techniques. This section will therefore go into detail about the different methods that were selected to analyse each sample from collection, preparation to testing.

3.1 Barnacle

The Barnacle specimens were previously collected from the coastal region at Bracelet Bay, Swansea, UK (51.5660° N, 3.9801° W) (129). Multiple barnacles, individually and in clusters, were adhered to a piece of driftwood. All samplers on the driftwood were dried in ambient room temperature and humidity. Testing was completed on the dried samples.

The workflow for this sample is shown in figure 3.1. XRF was not used to test this sample, which is represented by the box being greyed out. In-situ mechanical testing was used as a part of X-ray micro- CT imaging to evaluate crack propagation.
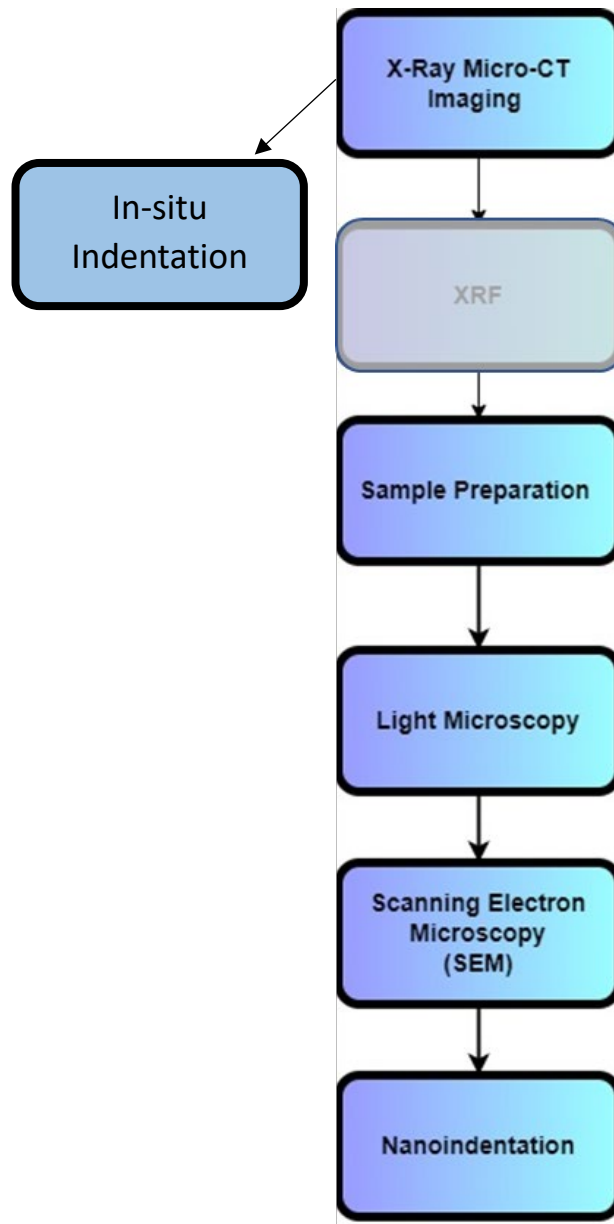
Figure 3.1. Workflow used to test the barnacle sample. XRF was not used and in-situ indentation was performed as a part of X-ray micro-CT.

3.1.1   Mounting

Care was taken in deciding the best approach for mounting the samples. Biological samples may be affected by the heat and pressure used in compression or hot mounting; therefore, samples were cold mounted using different resins based on previous literature.

Barnacles were delicately removed from a cluster on a piece of driftwood using tweezers and a scalpel in a manner such that they remained intact to maintain their plate configuration, allowing for easier mounting than single plates which may slip or change orientation when the resin is poured. The barnacles selected were in three sets of two, this was selected as they showed good external macrostructure and were not able to be separated.

The acorn barnacle was cold mounted in Epoxy 2000 from Optimal Scientific Ltd. The resin mixture was poured into the 32 mm mould very slowly along the edges to avoid the barnacle being pushed to one side or falling onto its side from its face down orientation. It was orientated in this manner such that there would be uniform exposure of the alae in the grinding and polishing process.

Vacuum impregnation was used to remove any residual air that may have become trapped within the empty cavity of the barnacle. The pump was set to 25 Pa for 45 minutes. After 45 minutes the valve was released slowly and the barnacle in resin was left on a stable surface within the fume cabinet overnight. The manufacturer guidance for the setting time was 16 hours.

Once set the barnacles were scanned using x-ray micro-CT. The purpose of setting the barnacle prior to scanning was to prevent movement of the plates during the scanning process.

3.1.2 Grinding and Polishing

Table 3.1 shows the grit of the SiC disks used in grinding, with their corresponding surface finish. The table is divided into coarse (yellow) and fine grinding (blue).

Grit number	Micron
P60	269
P80	201
P100	162
P120	127
P180	78
P240	58.5
P280	52.2
P320	46.2
P360	40.5
P400	35
P500	30.2
P600	25.8
P800	21.8
P1000	18.3
P1200	15.3
P1500	12.6
P2000	10.3
P2500	8.4
P4000	5

Table 3.1. The grit of SiC disks and their corresponding micron finish.

Polishing was performed with a water-based diamond pastes and finished with colloidal silica to achieve a surface finish of 0.05 μm.

The samples were carefully ground with increasing values of silicone carbonate disks up to 4000 grit with water as lubricant. The initial grinding steps with the lower grit disks was performed cautiously with regular observation using light microscopy between each step to prevent the removal of too much material causing the ala not to be observed. Between each stage the barnacle sample was washed with water and was observed under a light microscope to ensure that the surface finish was improving and most importantly to ensure that the ala region had not been lost in the process by grinding the sample too far. Water based diamond paste was used to polish the sample to a 1μm finish and colloidal silica was used to lastly to give the 0.05 μm finish. The sample was again examined under the light microscope between each step after washing.

3.1.3 X-ray micro-CT

This technique does not require detailed sample preparation as minimal disturbance of the material is preferred to achieve a true representation of the internal microstructure, however, there are factors to be considered when setting up the scan such as mounting.

X-ray micro-CT was used on the individual sample separate from Mitchel et al. to apply different aspects of the workflow X-ray micro-CT to sample preparation to nanoindentation, this was to ensure that the region of interest's location was known prior to grinding the sample.

The barnacle samples were scanned in resin prior to grinding and polishing to identify movement, if any, of the barnacle that may have occurred during mounting.

The Nikon X-Tek XT H225 Micro-CT was used to visualise the barnacle. The resolution at small sample sizes is 1 μm and has capabilities of 150 geometric magnification. The acceleration voltage range between 25kV – 225 kV allows for analysis of a wide range of materials and sample sizes. The images were reconstructed with CTPro software. Visualisation was completed with Drishti to view the 3D structure in detail.

3.1.4 Light Microscopy

The light microscope used is the Zeiss Primotech (Carl Zeiss Microscopy GmbH). The mounted sample was examined between each fine grinding step and polishing step to observe the quality of the barnacle surface. The presence of multiple microstructural features such as the trabeculae and haversian systems were observed using increasing objective magnification 5 – 20x magnification. The use of the 20x magnification allowed for a better understanding of the microstructure that would be visible using the onboard optics in the Ti950 Triboindenter such as the locations of the alae regions on the plates.

3.1.5 Scanning Electron Microscopy

The Carl Zeiss EVO LS 25 was used to image the barnacles with a back scatter detector at 15kV, 750 pA and a working distance of 10 mm.

The EBSD of the barnacle sample was performed on a JEOL 7800F FEGSEM and a NordlysNano EBSD detector controlled via Aztec (Oxford instruments) software were used to obtain crystallographic information.

3.1.6 Nanoindentation

Nanoindentation was performed with the stand alone, Bruker Hysitron Ti950 Triboindenter (Hysitron, Eden Prairie, USA). The tip used was a diamond Berkovich with a tip radius of 150 nm.

3.1.7 Accelerated Property Mapping

The Bruker Hysitron Ti950 (Bruker Hysitron, Eden Prairie, USA) system located in Swansea University is equipped with the Performech II stage controls that enables this type of intricate testing to be performed.

Prior testing is performed in different regions of the sample to optimise the features such as map resolution, indent spacing and ideal load as this test is performed under load control feedback. The indent spacing was assessed by SPM of the surface post indentation, and it was ensured there were no interactions between indents. If there is insufficient space on the sample, if possible, another sample of the same or similar material should be analysed. It important to design the method specifically to the sample. Before performing any XPM mapping the "Bias offset" was set to 2000 nm and the transducer was calibrated via an air indent. Appendix B details the importance of indent spacing and the impact of indent overlap on a standard material provided by the manufacturer.

Once the XPM settings were decided the following map was performed in the region highlighted in figure 3.2.

The indents were performed on the cross-section of the plates that included the body of the plate region found to have small grain microstructure as well as the ala which was found to have elongated crystals. To visually identify any differences in the mechanical properties between the plate body and the ala, XPM was chosen as the suitable technique.

To determine the ideal setting for this method the tests were performed on other barnacle samples prepared in the same way. Smaller maps were created across the junction between the fine equiaxed region of the plate body and the elongated crystal region of the ala as well as on the plate body alone.

The final settings were determined for XPM. The load was 1200 µN with a spacing of 2 µm between indents to total area to be indented was 240 µm by 240 µm this was achieved by chaining 144 maps of 20 µm by 20 µm area, the maps were spaced 20 µm apart from the centre to avoid overlapping of maps. Overlapping or too large spacing between maps can cause artefacts that are seen in the maps. Overlapping maps have the same effect as overlapping indents, maps spaced too far apart show gaps between the maps when the data is presented. This resulted in a total of 14400 indents for statistical analysis.
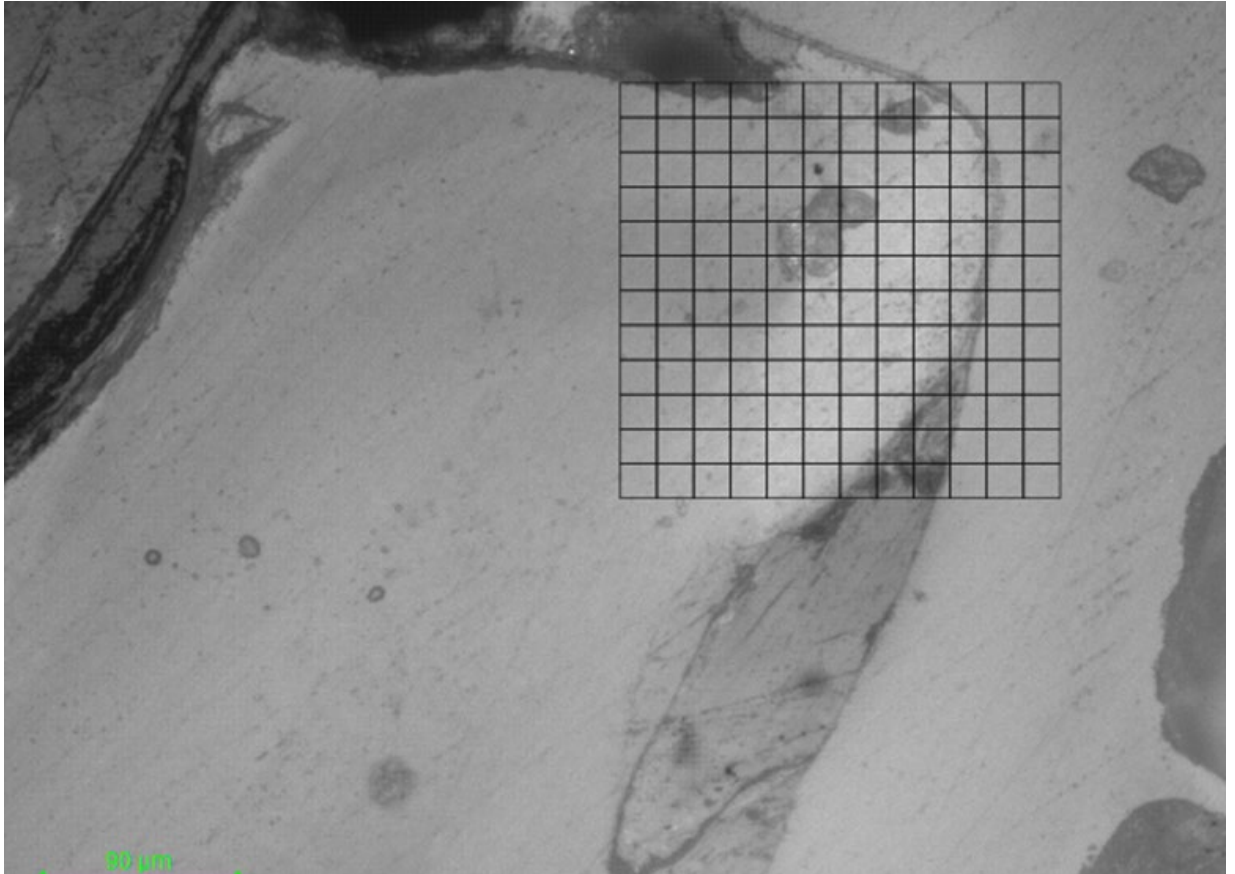
Figure 3.2. Optical image of the barnacle ala interlocked with the adjacent plate with a grid showing the location of the chained XPM maps.

3.1.8   In-Situ 4D Testing

4D testing is able to provide a detailed insight into the behaviour of a material. For this work it was utilised to explore the propagation of cracks through the barnacle plate and alae. Fractures that occur within a material are 3D structures, and assessment of the behaviour during formation is key to understanding mechanisms that are in place to prevent failure, as seen with biological materials.

The IntraSpect 360 (Bruker Hysitron Eden Prairie, USA) is an in-situ indenter for the Zeiss Versa 520 which enables 4D analysis of materials, with a peak load of 10 N and maximum depth at 80 μm. It utilises a piezoelectric load cell design with capacitive depth sensing and performs both load- and displacement-controlled testing methods using the Performech digital controller. Different probe geometries can be installed on the device including a diamond Berkovich, wedge, or titanium punch geometry to cater to the differences in materials. Unlike indentation in the Ti 950, the sample is not required to be flat or smooth, as long as the sample is small enough to fit on to the specifically designed stage piece, chuck, approximately 10 mm x 10 mm, it is suitable for testing. Significant handling and altering the shape and size of the sample may interfere with the internal microstructure causing deformations that may lead to a false understanding of the behaviour of the material.

One of the barnacle plates was carefully removed from a new specimen with tweezers. The plates were selected based on previous x-ray micro-CT and light microscopy data; the plates chosen were side plates which have a single ala. The barnacle plate sample was approximately 4 mm in length 1 mm thick and 5mm in width, figure 3.3 displays the dimensions and the parts of the plate. A cyanoacrylate adhesive was used to attach the plate to the chuck, the plate was orientated such that the ala was the highest point by adhering the radius to the chuck. This orientation was selected to prevent possible interactions between the indenter tip and other regions of the plate.

The loading increments for each scan was decided from prior testing. In the preliminary testing, the load was applied to another barnacle ala with an increase of 500 μN per increment, starting from a load of 0 μN. The increments were found to be too large as complete failure of the ala was found at 1000 μN, after 3 scans.

As each scan was in excess of 14 hrs a compromise was necessary with the number of scans to be made. It was decided that increments of 250 mN would be sufficient to observe crack formation to the point of complete failure at 1000 mN.

Prior to beginning each scan the reference images were taken without the sample housing part of the IntraSpect 360 in-situ. This was due to it being too large to move out of the field of view to gather the reference with nothing in the field of view. There were 2 scans performed at 0 µN load to use for digital volume correlation. To do this between each scan the sample was unloaded and the tip was moved away from the sample. The following scans were performed at 250 mN, 500 mN and 750 mN loads, i.e., until failure was observed. The indenter was set to hold the load for longer than the expected scan time to reduce the likelihood of movement during the scan.

The scan was performed with the 20X objective at 140 kV, Binning 2, 71.5 µA with a voxel size of 0.6278 µ and the field of view was 624.66 µm. The exposure was set to 30s per projection, making the length of each scan 14 hrs and 17 minutes. The source and detector were brought in as close as possible to the IntraSpect 360 with sufficient space for it to rotate through 180° during the scan. Set up of the IntraSpect 360 in the Zeiss Versa is shown in more detain in appendix A.

X-ray micro-CT exposure over the lengths of time were found to make the biological samples more brittle. The barnacle alae were thoroughly dried at room temperature. The samples were stored at room temperature in the lab for several months prior to testing with this method to avoid any changes that may occur from drying out.

The tomograms from each scan were reconstructed from 2D projections using a Zeiss Microscopy commercial software package (XMReconstructor) and an automatically generated cone-beam reconstruction algorithm based on filtered back-projection. The reconstructed data was then analysed to observe the fracture behaviour using Avizo (Thermo Fisher Scientific). Digital volume correlation was performed with DaVis 10 (LaVision).
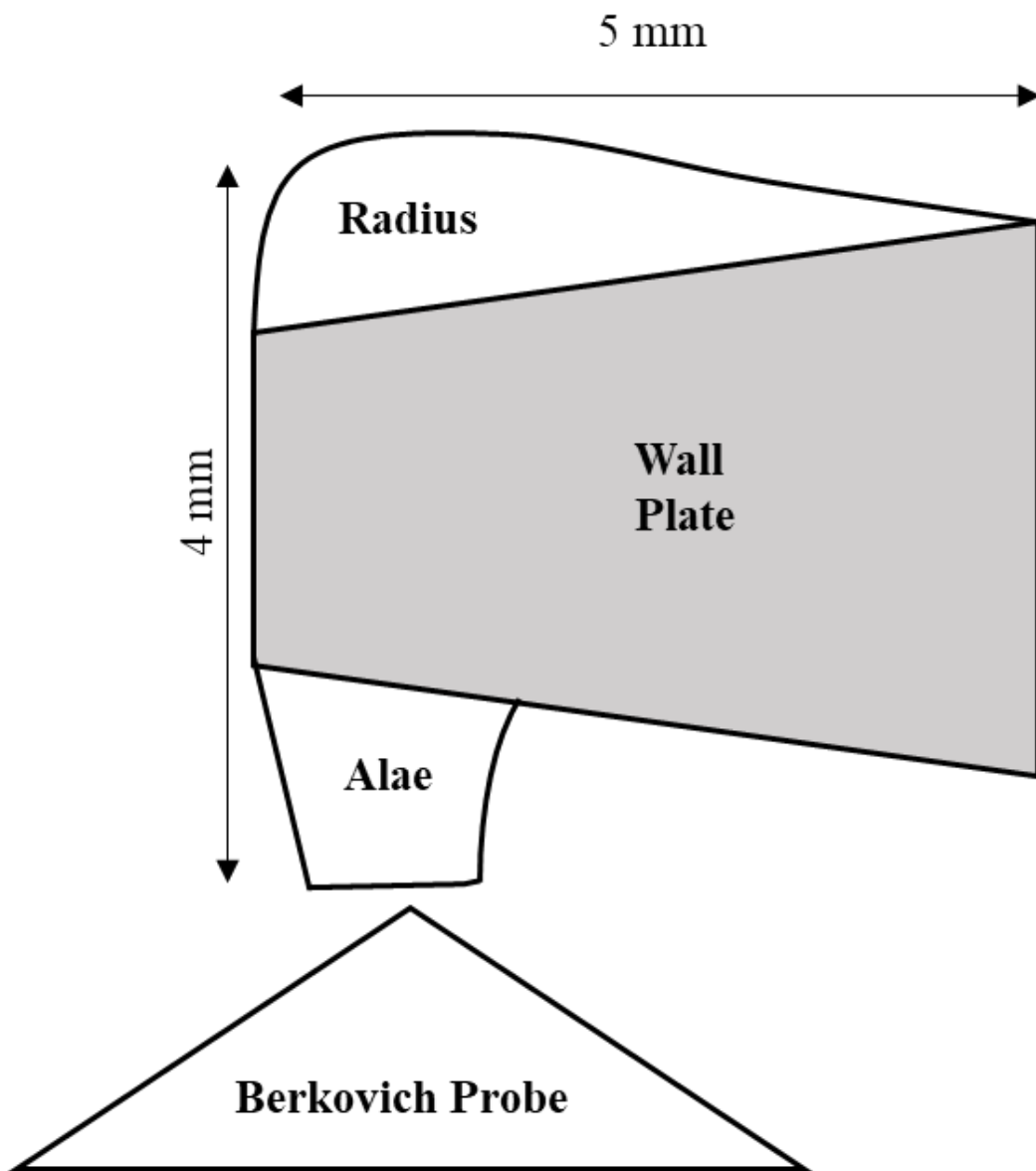
Figure 3.3. Schematic showing approximate dimensions of the barnacle plate and the orientation set up used for in-situ indentation.

3.2 Antlers

Antler samples were obtained from the Cairngorm Reindeer Herd, Reindeer House, Glenmore, Aviemore, PH22 1QU. This is Britain's only free ranging herd of reindeer, located in the Cairngorm mountains in Scotland where they have lived since 1952 when the native species was reintroduced.

The antler samples were shed naturally and collected by the herd keepers, who labelled the antlers with the name of the reindeer who shed them. One antler was not shed naturally, Keats antler was removed after the velvet was shed and the bone had dried out in order to prevent injury in the rut. The antlers were stored in ambient temperatures prior to being posted to Swansea University for testing. The list of names of the reindeer antler samples were sent in advance by email along with further information including the year the antlers were shed, age, sex, and for those who are female their calving status the year of shedding. This data was collated in table 3.2.

When received at Swansea University the samples were sorted according to the following groups based on sex and calving status Male (M), female without a calf (FNC) and female with a calf (FWC).

Preparing these samples for analysis presented their own unique series of challenges to overcome, such as contamination prior the chemical analysis and selecting the ideal resin to determine the mechanical properties of the samples, without interference from the resin within the porous structure of the antler.

The workflow used to analyse the antler samples is shown in figure 3.4. As this sample was not an addition to previous work as the barnacle was. The full workflow was applied to these samples.
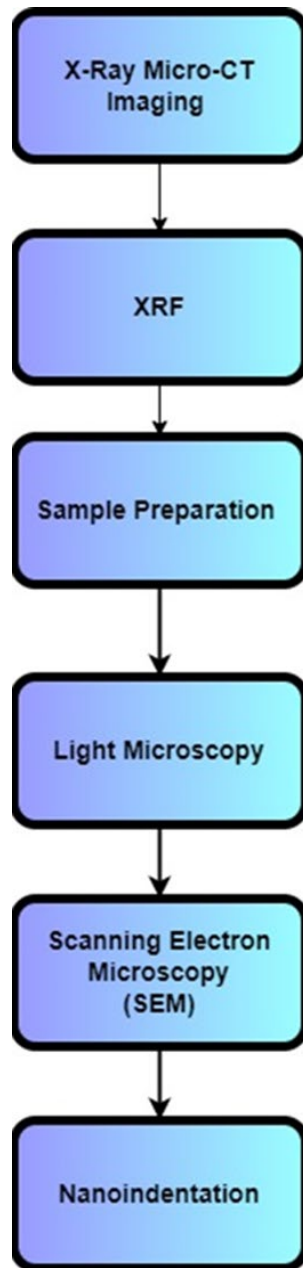
Figure 3.4. The full workflow as applied to the antler samples.

Name	Year Grown	Age during antler growth (years)	Sex (M/F)	Calf (Y/-/N)
Galilee	2018	5	F	N
Angua	2019	1	F	N
Caterpillar	2020	9	F	N
Sika	2019	11	F	Y
Ibex	2017	9	F	Y
Dante	2020	3	F	Y
Brie	2019	6	F	Y
Jenga	2020	9	F	Y
Oatcake	2020	11	F	Y
Clouseau	2019	1	M	-
Sherlock	2020	2	M	-
Frost	2020	2	M	-
Carnethy	2017	2	M	-
Keats	2018	1	M	-

Table 3.2. List of names and details of antlers received for analysis. The antlers were labelled with this information to prevent mismatching.

3.2.1   Mounting

10 – 20 mm sections were cut by hand using a hacksaw along the transverse section of the antler, hand cutting was used to avoid contamination from water with the available automated cutting wheel in the lab.

They were then embedded in CEM1000 Blue from Optimal Scientific Ltd., a non-infiltrating resin in a 32 mm diameter mould. A vacuum was not used to prevent the resin from infiltrating into the fine pores of bone. The antler sections were orientated such that a cross transverse section was exposed for nanoindentation. To prevent the antler samples from moving or changing orientation while the resin was being poured into the mould, wooden stirrers were used to hold the sample in place and removed before the resin set (manufacturer setting time 12-15 minutes).

3.2.2   Grinding and Polishing

The samples were carefully ground with increasing values of silicone carbonate, starting as a coarse grit as the surface was sectioned with a hack saw and progressively moving up to 4000 grit with water. Water based diamond paste was used to polish to a 1µm finish and colloidal silica was used to lastly to give the 0.05 µm finish. Additionally, between each stage the antler samples underwent a cleaning step in the ultrasonic cleaner for 5 minutes to remove debris and artefacts from the previous grinding and polishing stages. Each of the grinding and polishing steps were completed manually. After each step the samples were observed under a light microscope to ensure that the surface finish was improving, and the microstructure was becoming more visible as the process continued. After finishing with colloidal silica an additional ultrasonic cleaning step was performed to prevent the formation of a film on the sample surface.

Of specific note when preparing this sample type it was important that between each step the samples were cleaned in an ultrasonic cleaner to remove larger particles before moving onto the next, finer step (130,131). Although it has been stated that ultrasonic methods should be used with caution (132) previous sample preparation attempts on antler samples showed large scratches along the surface due to particles not being

efficiently removed by washing under running water. An ultra-sonic cleaning step was also performed after the final stages to remove remaining residue (133). If not cleared, the residue that remained from the preparation of reindeer antler formed a brittle film over the sample surface that would affect the nanoindentation results, as seen in figure 3.5 (a) which shows the *P-h* curve that displays pop-in effects and figure 3.5 (b) the after effect of the indent showing cracks in the layer originating from the site of indentation, the nature of the composition of the film was not determined due to time constraints, however, it can be determined by application of techniques such as Raman or XPS. This stresses the importance of this final ultrasonic cleaning step as without it the resulting residue can affect the nanoindentation testing.

After grinding and polishing the samples were dried to their original pre-prepared state at standard room temperature and humidity. This is due to the fact that reindeer use their antlers post velvet shedding and the tissue is considered to be dry during its functional use during the rutting season for males in deer species (82).
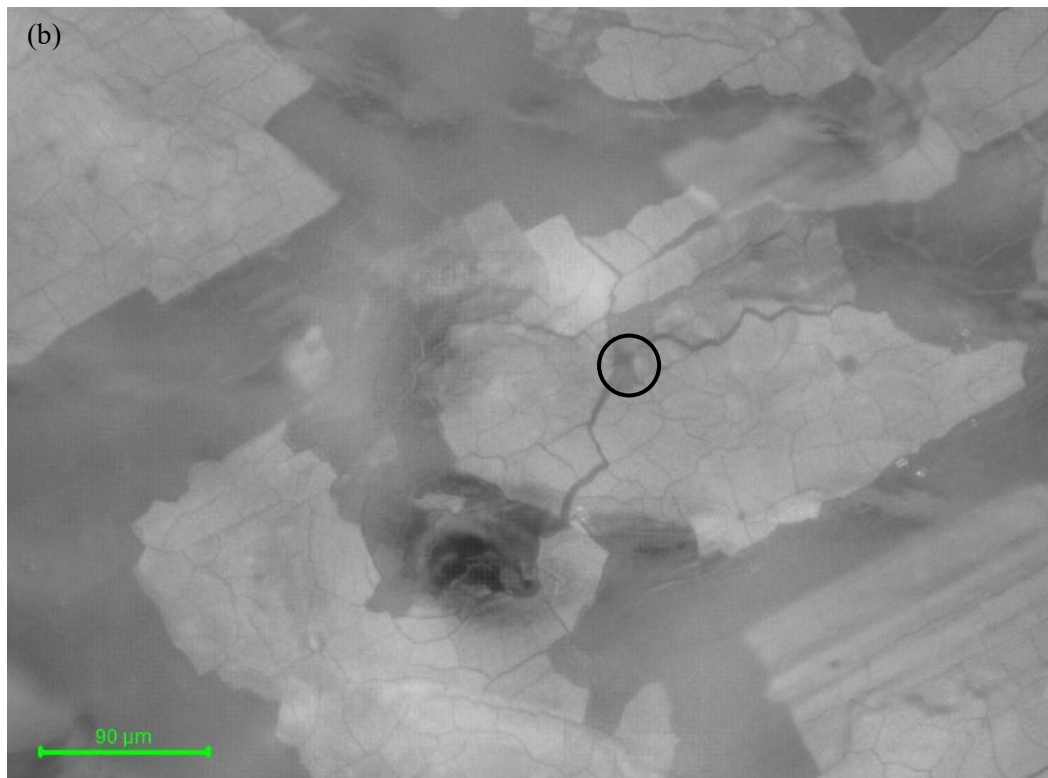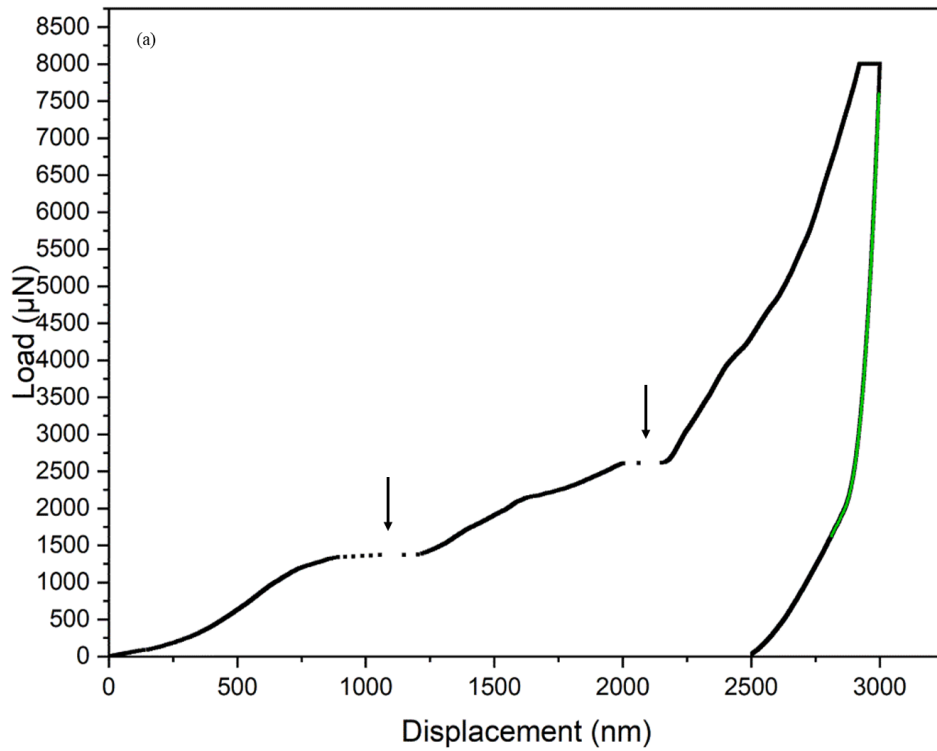
Figure 3.5 (a) P-h graph showing the pop-in effects caused by the brittle layer which remained on the sample with washing only. (b) Image from the onboard optics of the Ti950 indenter which shows cracks radiating from the point of the single indent which is circled on the image.

3.2.3 X-ray micro-CT

Sections of the main beam of the antler were cut by hand with a hacksaw for analysis as shown in figure 3.6. Care was made in selecting the sections for analysis due to their uneven shape there is the possibility of collision of the sample with the source while rotating during the scan, while trying to maintain higher resolutions.

Unfortunately, due to unforeseen circumstances with the Nikon X-Tek XT H225 Micro-CT, it was out of operation for an extended time which resulted in not all samples being able to be scanned. Preliminary scans were performed on three samples Ibex (FWC), Carnethy (M), and Keats (M) of a low resolution to visualise the internal cortical and trabeculae regions.

Therefore, this section will detail the intended work to be completed on all the antler sections with a higher resolution.

The samples would be analysed with BoneJ which is a plug-in for ImageJ specified for bone analysis.

All samples from the three groups detailed previously M, FWC and FNC will be scanned. The parameters to be compared would be average cortical region thickness along the length of the main beam to observe any differences between groups.

Another feature to be examined would the ratio of bone to total volume or area volume fraction, where the fraction of bone in the image is calculated. BoneJ accomplished this by counting the voxels in the foreground, which is assumed to represent bone, it will then compare it to the total number of voxels in the image. This gives the volume of mineralised bone per unit volume (134).

Figure 3.6. Image of intact male antler (frontal tine is broken) with areas to be cut on the main beam highlighted. The regions of the antler are labelled. The area has some uniformity along its length to avoid collisions during scanning.

3.2.4 X-ray Fluorescence

X-ray florescence (XRF) is a technique that performs elemental analysis and is based on the principle the primary x-rays generated from the target source causes the different elements on the surface of the sample to emit secondary x-ray radiation which are detected by the device. The samples were all cut from a section of the main beam of the reindeer antler to approximately 20 mm or lower. This height would allow for the safety top to be placed on securely for testing in bench top mode.

Care was taken to prevent any possible contamination in the process of cutting and storing the antler sections. Contamination with Cl can occur from the cutting process as seen in Figure 3.7 where a water cutting blade was used in the sample labelled Carnethy and not used in the sample labelled Ibex which was dry cut with a hacksaw.
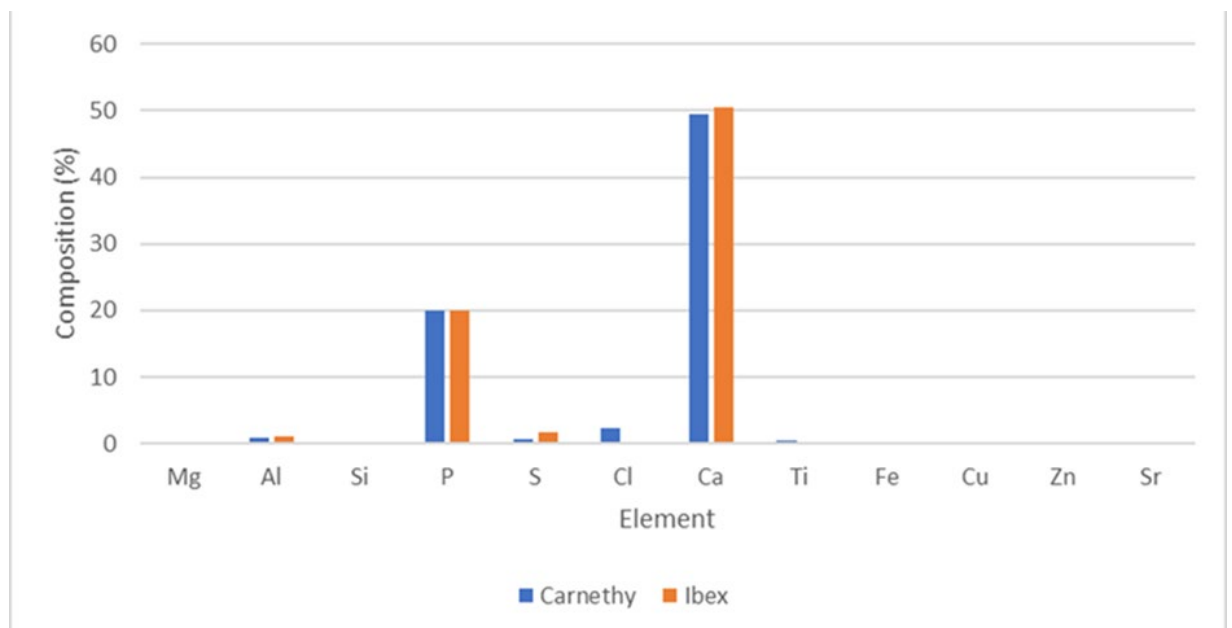
Fig 3.7 Graph comparing chemical composition between Carnethy and Ibex after using wet and dry cutting methods.

As with internal skeletal bone the main mineral phase of the antler is composed of Ca and P (36,106,107). Additionally, Mn was of interest in this study due to it being known as an important osteotropic element and in addition to stimulating bone matrix synthesis has an effect on calcification in general (135). The three antler groups, male (M), female with calf (FWC), and female without a calf (FNC).

The XRF equipment used for antler sample analysis is a handheld, 7500 XMet Oxford Instruments (Oxford instruments plc.) available at Swansea University AIM facility. The instrument was used in a bench top mode which will improve testing over longer times. Safety checks were carried out as outlined in the Swansea University Ionising Radiation Policy prior to further testing. The X-ray beam is at 40 kV or 40 µA.

Once switched on, the date and time for the device was set. The method selected for testing the antler sample was Mining LE FP which would present the presence of elements as a percent value of the area scanned. Based on previous literature the test time was set to 120 seconds per scan. With the understanding that biological materials have a heterogeneous composition (136) between each test the sample was orientated in a manner such that each scan would be of a different region of the antler cross section. This would enable an average across the area scanned to be determined.

The standard provided by the manufacturer was tested before the samples. Once the samples were tested, and the results were stored against the names of the reindeer to be able to better correlate the data.

3.2.5 Scanning Electron Microscopy

The Carl Zeiss EVO LS 25 was used to image the antler samples and perform EDS analysis. They were analysed using the variable pressure setting as the samples were non-conductive and were scanned without carbon coating. Multiple images were taken, and varying magnifications and the kV values were adjusted accordingly to capture suitable images and maps.

One sample from each of the three categories was selected for EDS analysis Clouseau-M, Galilee- FNC, and Oatcake -FWC. These samples were selected as they all had the presence of Mn during XRF analysis this is shown in table 3.3 along with their Ca and P percentage composition.

Name	Sex	Calf / No Calf
Galilee	F	No Calf
Oatcake	F	Calf
Clouseau	M	-

Table 3.3. One sample from each of the three categories were analysed in XRF to determine the percent composition of elements present in each of the antler samples.

3.2.6 Nanoindentation

The indents were performed across the cortical regions only of both the transverse and cross-sectional prepared surfaces to investigate the presence of anisotropy in the antlers as displayed in figure 3.8. The properties of the trabeculae were not assessed in this study.

Figure 3.8 Mounted, ground, and polished sample ready for nanoindentation showing a transverse and cross section surface.

3.2.7   Traditional Indentation

The peak load was 8000 µN with a loading time of 10 seconds, a hold time of 30 seconds to account for the time dependent nature of the antler bone and an unloading time of 10 seconds. The hold time of 30s was selected to account for the creep that can occur due to the viscoelastic properties antler cortical region. This will avoid the *P-h* curve as shown in figure XX where the initial segment of the unloading curve is steeper, causing an increased stiffness value which goes later results in an increased modulus value. Therefore, to acquire a true understanding of the material, this extended load time was used.

An array of 25 indents were performed using the automation setting they were formatted in 5 rows with 5 columns with a 10 µm spacing between each indent to prevent indentation interaction effects. The first indent in this array is the bottom left indent, before beginning the test a region clear of any pores or osteons greater than the expected test area 25 µm x 25 µm was selected to prevent the indents from falling into any of these features. Figure 3.9 shows an example of the location of the indents after the test was performed.
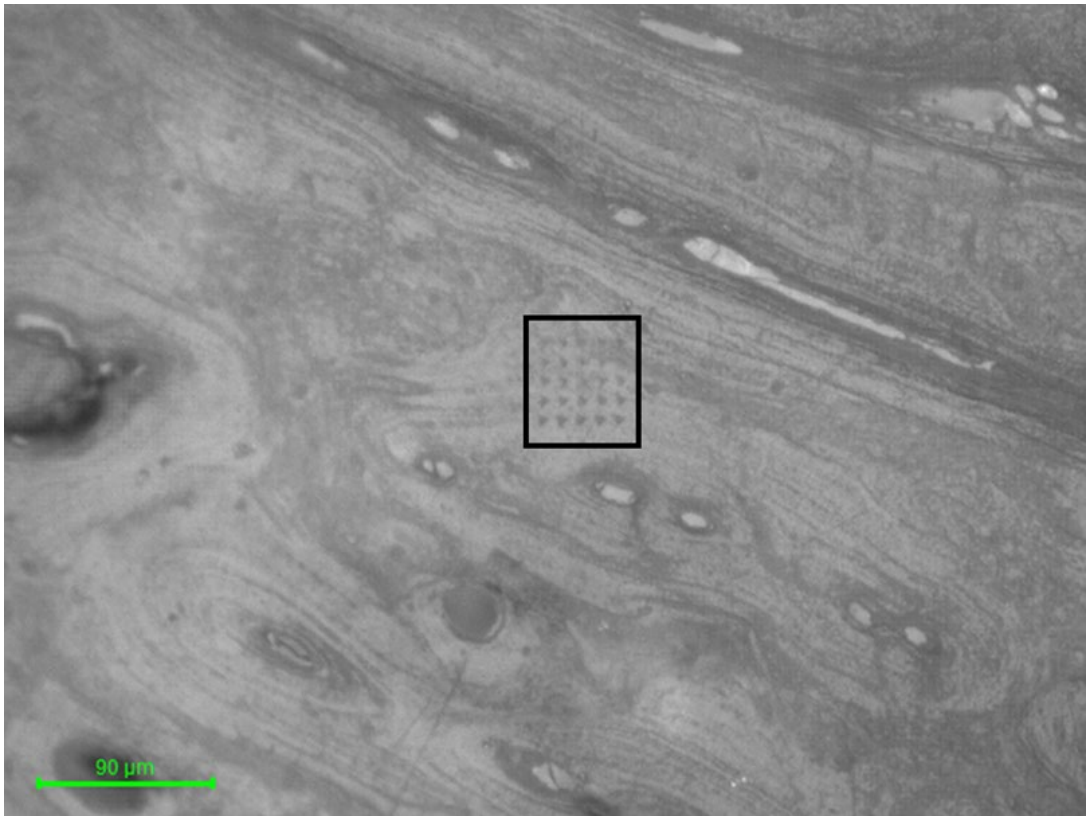
Figure 3.14. Series of 25 load-controlled indents with a 10 µm spacing between indents on an antler cross section.

3.2.8 Accelerated Property Mapping

This technique has been applied to the antler of reindeer not to perform comparisons between sex and the calving status, however it has been applied in this instance to understand the differences between the lamellar structure around the osteons – so identifying microstructural differences within samples. The tip used was a diamond Berkovich with a tip radius of 150 nm.

Prior testing in another region was performed to determine suitable depth from which the load would be selected the desired load was found to be 1000 µN. The spacing selected was 2 µm to prevent interaction and would provide suitable resolution to map the different lamellae. A single map comprised of 10 indents to cover a 20 µm x 20 µm area.

Regions were found on both the transverse and cross-sectional areas of the same sample that showed the lamellar structure. SPM was performed on a 50 µm x 50 µm, (larger than the estimated map size) area to display the presence of the lamellae as well as to determine the Ra value in the region to ensure the maps would provide reliable results.

Four of the maps were chained together using the automation setting in the Ti 950 in a 2 x 2 format. The maps were spaced 20 µm apart to prevent any overlapping from occurring. The total area covered was 40 µm x 40 µm. To correlate the area where SPM was performed with the maps it was observed that the SPM area is performed with the centre of the optics as the centre of the SPM. Therefore, only a small movement was required to orientate the new centre of optics to where the chained maps should begin. It should also be noted that the centre of the optics is the centre of the XPM maps.

The total number of indents performed was 400 per section to be analysed using Tribo IQ. This software is provided by Bruker Hysitron with Origin Pro 2017 (Origin Lab, Northampton Massachusetts, USA) as its platform. The version of OriginPro used is 2019.

4 Results and Discussion

The results of the different methods applied in the workflow for each of the samples, barnacle and antler, will be presented and discussed in this section. This work shows the advantages of how a distinct series of processes, when applied in a cohesive workflow, is able to reveal the structure-property-function relationship in two different mineralised biological samples, the acorn barnacle and reindeer antlers. The accumulation of the data obtained from the multiple testing methods is brought together here to reveal previously unknown characteristics of these different materials, giving insight into how they have evolved to survive harsh environments and uses and how their structure informs their properties and function in nature.

4.1 Barnacle

The ability to incorporate nanomechanical property testing into a correlative imaging workflow can address the necessity raised by previously completed research, as with the acorn barnacle work performed by Mitchell et al. (3). Weaving nanomechanical testing into the characterisation workflow allows us to investigate further into how the previously discovered structures and crystallographic and chemical information can contribute to the localised mechanical properties thus contributing to understanding the function of the individual regions in the barnacle plates.

4.1.1 X-ray micro-CT

The macro- to the micro- structure of the acorn barnacle shows a level of organisation that has arisen from the necessity to survive in an extreme environment. The different levels of the structural organisation were explored using multiple imaging techniques, x-ray micro-CT, light microscopy, and SEM (this includes previous work by Mitchell et al.) The initial analysis by Mitchell et al. analysed the alae in a horizontal section, which was the direction followed in this analysis procedure to continue to correlate the structure with the properties of the region of interest (3).

X-ray micro-CT allows for the non-destructive visualisation of the structure of the barnacle exoskeleton it clearly shows the organisation of the plates that would have been otherwise missed with destructive methods. Exploration of the structure in 3D

has allowed for a greater understanding of how the structure helps with the functionality of the organism, and how the properties of the regions contribute to this. For the purpose of locating the region of interest, the location of the ala is higher in the plate, this will reduce the amount of material removal needed to expose for nanoindentation, but care must be taken as the length of the ala themselves are short as the plate curves away from the interlock region towards the base of the exoskeleton.

X-ray micro-CT enables multiscale observation of the internal structures such as where the alae are located and how they interlock into the ridge of the neighbouring plate. The alae were located towards the inner region of the barnacle, they are sheltered by the radii of the adjacent plate and not directly exposed to the harsh external environments. Instead the environment is relatively constant, and both the radii and the ala are in contact with the proteinaceous biological matrix produced by the living organism (137). These protected interlocking structures were identified as regions of interest for analysis by Mitchell et al. (3).

Figure 4.1 shows a full 3D reconstruction (a) of the barnacle to be later analysed by nanoindentation. It also shows a slice through the 3D section to enable a better understanding of the location of the alae in relation to the macrostructure, interlocking with adjacent plates, any slipping or movement that may have occurred when mounting in resin.
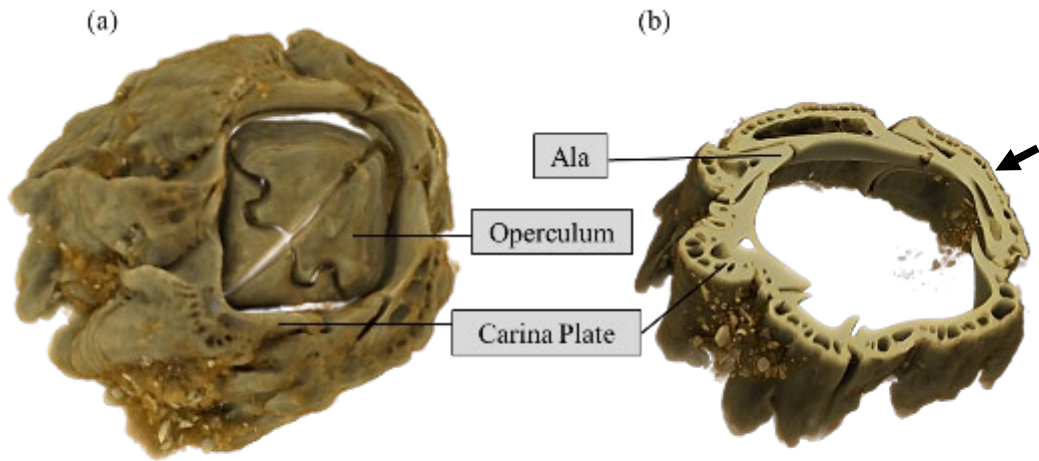
Figure 4.1. (a) 3D reconstruction of *Semibalanus balanoides* scanned using the Nikon X-Tek XT H225 Micro-CT displaying the external shell structure with the operculum fully closed. (b) slice through the 3D section of the barnacle to non-destructively show how the plates interlock and the function of the ala.

These protected, protected interlocking regions have been identified in literature as active growth fronts of the barnacle with the direction of the alae growth towards the rostrum plate (opposite the carina plate, to the anterior end of the barnacle). This plate is indicated by the black arrow in figure 4.1 b. The protection of the growth fronts by adjacent plates possibly allows for a greater chance of survival of the organism against the harsh inter-tidal environment, or against predators.

4.1.2   Light microscopy

Light microscopy allows for a wider field of view of the structures compared to SEM, therefore each plate could be mapped and labelled for further testing in SEM and nanoindentation. Light microscopy correlates well with both techniques, particularly for nanoindentation.

The barnacle cross section shows a distinct organisation of the plates easily visible from external viewing only. Figure 4.2 clearly shows the operculum, which is a collection of 4 plates that form a roof like structure that opens and closes accordingly to the demands of the organism.

The plates have been organised in a manner such that they interlock with the ala in an overlapping manner, as shown in figure 4.3 with large pore regions along the outer regions of the plate. The organism may have organic tissue in these pores (138) that can contribute to repair given the situation of the pore regions near the outside they will be prone to damage from the environment and predatory organisms.
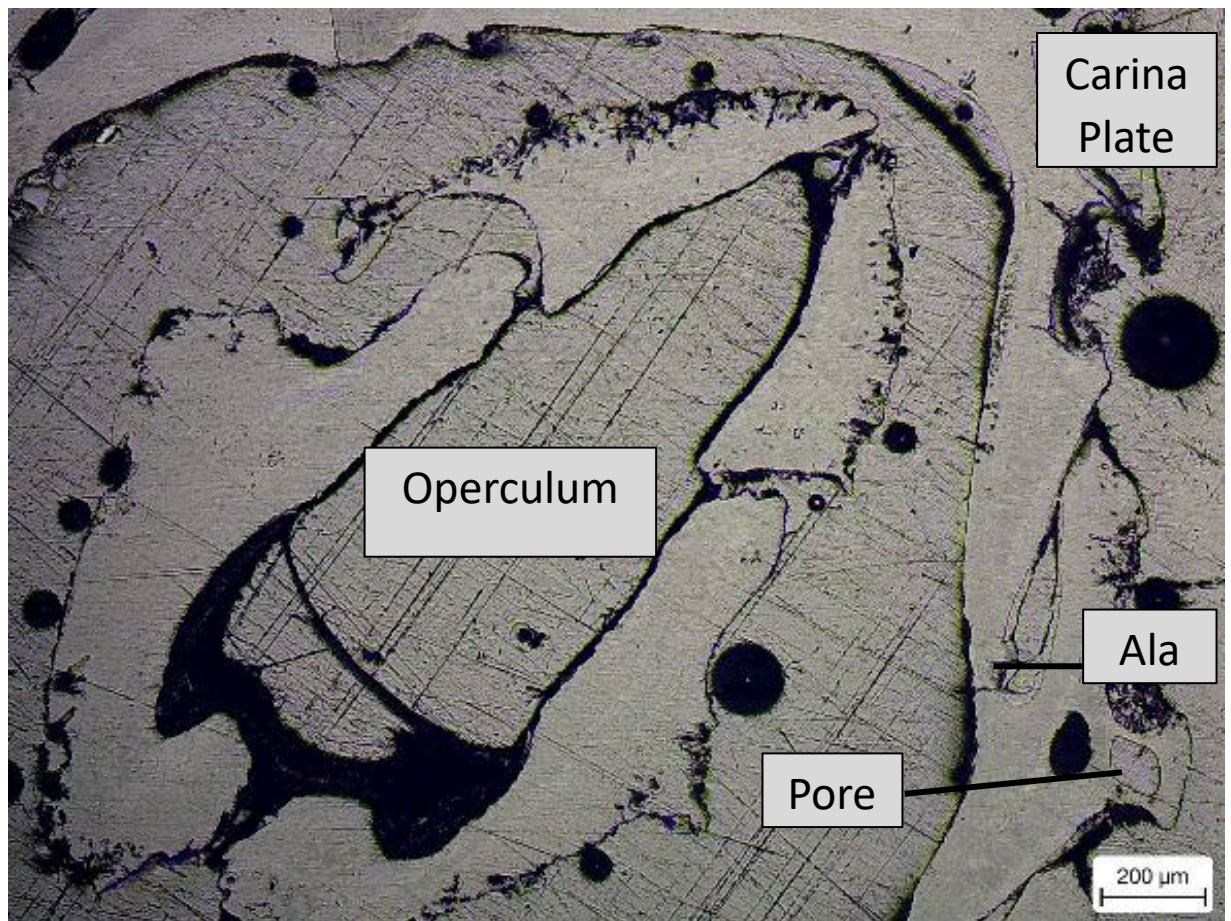
Figure 4.2. Light microscopic image of barnacle set in rein at a lower magnification feature such as a section of the operculum region and the ala of the carina plate intersecting with its adjacent plate. A large pore is highlighted on the sample.

Closer inspection of ala as seen in figure 4.3 the ala is towards the inner region of the barnacle therefore also exposed to organic tissue that may contribute to the growth front (129).

This protected growth front is also observed in x-ray micro-CT. The correlation between these two techniques is also able to verify that during the sample mounting process there were no movements of the plates, thus ensuring that an accurate representation of the alae cross sections in-situ is possible. Light microscopy is also able to confirm that the direction of growth of the alae is toward the anterior of the barnacle.
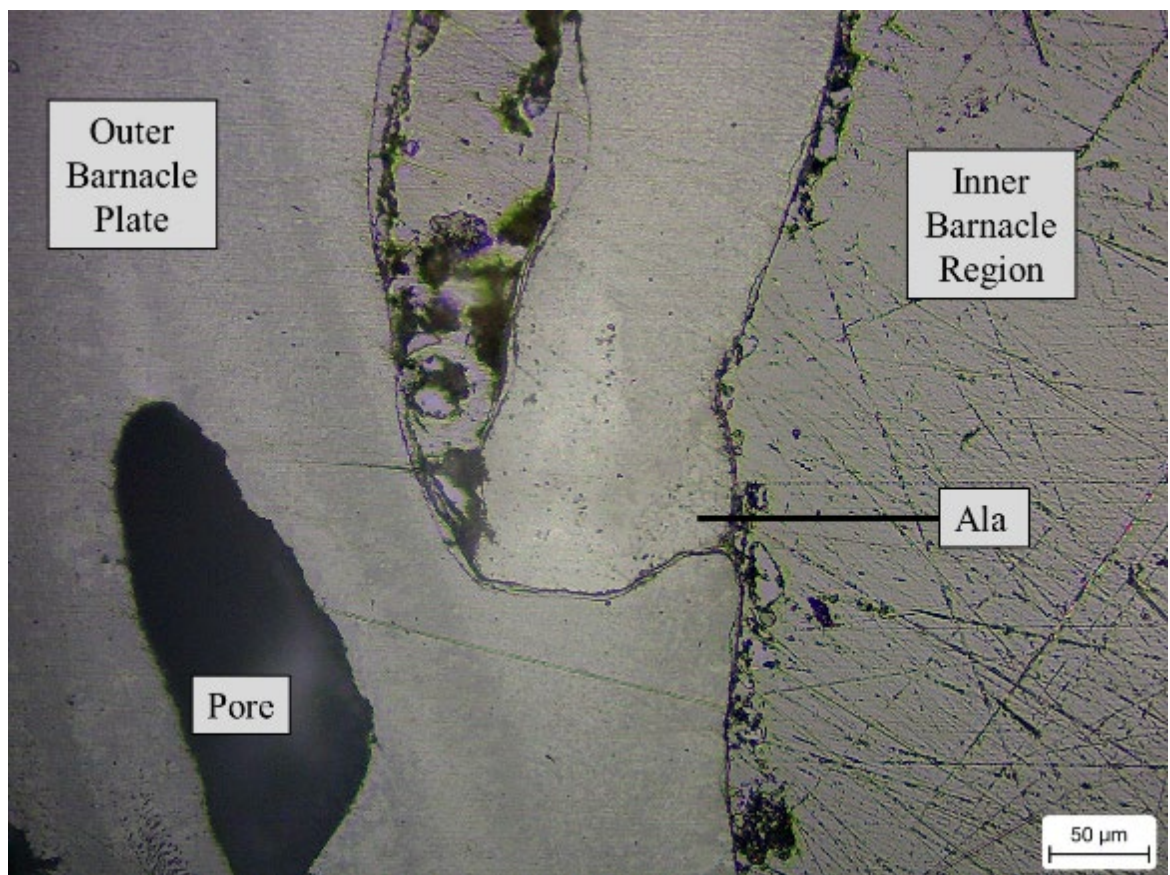
Figure 4.3. Light microscopy image of ala connecting to the neighbouring plate. The inner and outer regions of the barnacle are labelled to show the region in close proximity to the living organism and the region exposed to the harsh external environments.

Light microscopy aids in the process of nanoindentation where although the on board optics of the indenter system are only equipped with a 20X objective lens it is able to perform mosaic optical scanning where a series of images are taken and stitched together. Using the optical image map to locate the region of interest and clicking on the desired area on the mosaic on the Ti950 will automatically move to that region to perform testing.

4.1.3 Scanning Electron Microscopy

The EBSD presented here is from work published by Mitchell et al. into the macro- to nano-scale investigation of the ala (3). Figure 2.1 was taken from the publication, "Macro-to-Nanoscale investigation of wall-plate joints in the barnacle *Semibalanus balanoides*: a correlative imaging, biological form and function, and bioinspiration." In figure 2.1 an SEM image of the entire barnacle cross section is visualised in (a) the focus is narrowed down to two ala regions inset *a* and *b,* in (b) which are shown as individual regions of interest in (c) and (d). Both sections had EBSD performed on them to reveal the calcite crystallographic structure as observed in (e) and (f).

Figure 2.1 also shows the dual directional growth directions of the barnacle (a). Figure 2.1 (b) shows the alae fitting tightly into the socket-like grove in the neighbouring plate. The radii loosely interlock in the outer region of the plate which is also observed in figure 4.1 (b) and 4.6 (b). The interlocking of these regions may be for the organism to withstand the harsh conditions of the intertidal zones that they mostly inhabit (129). The proteinaceous matrix is in contact with both these two close regions of the abutting plates, this is evidenced by their smooth surface texture in comparison to the external surfaces which is inContact with the external environment (104).

Mitchell et al. found that at the ala region of the barnacle plate the calcite crystals displayed an elongated grain where in each case the c-axis of the crystal [0001] is in fact parallel to the long axis of each grain. The elongated calcite was also found to be perpendicular to the line where the plates join. The grains located in the main body of the plate were approximately 10 – 20 times smaller than the grains in the ala region. Mitchell *et al*. commented that the structure of the grains of the main body is more equiaxed and that there was no obvious texture (3).

Previous literature also reports a similar crystallographic structure in the radii of the plates, as both the alae and the radii are in contact with the matrix surrounding the living tissue inside and have both been identified as the active growth front (144).

From the details of the corelative imaging analysis, Mitchell et al determined that due to the distinct crystallographic features of the barnacle species the elongated crystals of the ala region represent a growing front where there will be active biomineralization by the organic tissue present from the living organism (3). The paper went on to identify the need for nanomechanical characterisation in a future workflow, in order to understand how the mechanical properties in the specific regions, plate body and alae are affected by the crystallography of the calcite.

4.1.4   Nanoindentation

4.1.4.1   Accelerated Property Mapping Correlated with EBSD

The correlation of EBSD with XPM for barnacle alae is novel, previous research on other biomineralized materials was performed using traditional indentation techniques, and mapping was previously performed on brachiopods by Perez-Huerta and Zhu who stated that variations in crystallography influence the properties of calcite shells (139). The scale on which XPM provides information of the mechanical properties of distinct crystallographic regions gives insight into the relationship of how region-specific orientations as observed in in the acorn barnacle contribute to the understanding of natural materials, and how this can go on to inform future developments in materials science.

Correlating XPM with the EBSD data for the barnacle alae shows that the orientation of the crystals in the ala region does have an impact on the local nanomechanical properties. This may be to cope with the high-energy environment in which they live or since the region is in active growth and in direct contact with the matrix which is also in contact with the radii.

Analysis of the map and data shown in figure 4.4 clearly shows two distinct regions of hardness between the elongated crystal ala (green highlighted region) and the main plate (red highlighted region).

The main plate region showed an average hardness of 3.8 GPa and modulus of 74GPa from 3493 points included in the red area highlighted for testing with a standard deviation 0.6 and 7.5 respectively. The ala region displayed an average hardness of 2.9 GPa and an average modulus of 65 GPa from 2367 indents in the green selected region for testing, with a standard deviation of 0.8 for hardness and 10.6 for modulus. This showed a distinct 25% difference in average hardness between the two regions. While the difference in average modulus was found to be 16%.

Apart from the mean modulus and hardness values the statistical data also presents the skewness and kurtosis of the data. The skewness of the red region for modulus and hardness are -0.2 and -1.1 which shows that the data is negatively i.e. the values are

more concentrated towards the higher end of the values on the scale. Similarly, for the green region the data is skewed negatively with -0.4 for modulus and -0.3 for hardness thus more values in this data set are higher but less so than the hardness of the red region.

Kurtosis refers to the number of points that fall within the normal distribution of the data, i.e. the thickness of the tails. The red region shows a kurtosis of 1.9 for the modulus and 3.4 for the hardness. This will reflect on a normal distribution chart as the modulus having very small tails either side of the peak with very little data in those regions whereas the hardness kurtosis value of over 3 shows that the data either side of the peak are similar to that of the peak itself. The Kurtosis of the green region, is 1.3 and 0.04 for modulus and hardness respectively, this shows that the data either side of the peak is very low comparatively.

Statistic	Cluster 1 Modulus (GPa)	Cluster 1 Hardness (GPa)
Mean	74.989	3.8086
Standard Deviation	7.486	0.60083
Standard Error	0.12666	0.010166
Number of Points	3493	3493
Variance	56.04	0.361
Skewness	-0.23257	-1.1478
Kurtosis	1.8936	3.4326

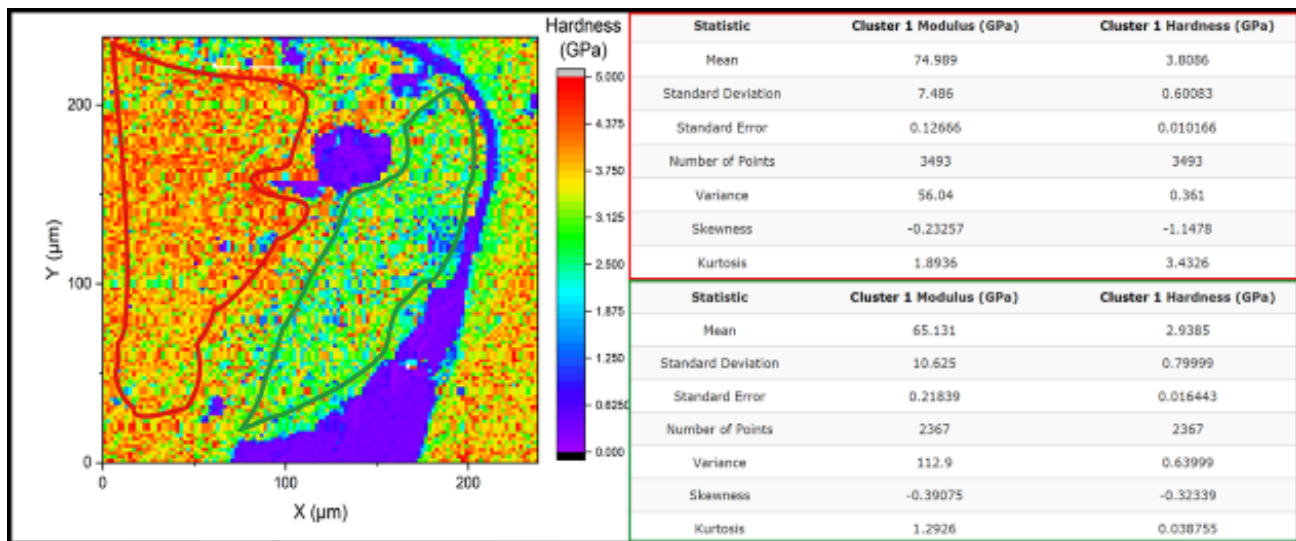| Statistic	Cluster 1 Modulus (GPa)	Cluster 1 Hardness (GPa)
Mean	65.131	2.9385
Standard Deviation	10.625	0.79999
Standard Error	0.21839	0.016443
Number of Points	2367	2367
Variance	112.9	0.63999
Skewness	-0.39075	-0.32339
Kurtosis	1.2926	0.038755

Figure 4.4. Showing hardness map of barnacle ala region. The regions analysed have been drawn in with the fine equiaxed grain region in the red region and the elongated grains within the green region. The statistical data for each region is displayed next to the map in colour coded sections.

Correlating the XPM with the EBSD data shows that the orientation of the crystals in the ala region does have an impact on the local nanomechanical properties. This may be to cope with the high energy environment in which they live or since the region is in active growth.

Mitchell et al. analysed the barnacle sample in the horizontal direction enabling the visualisation of this natural phenomenon of crystallographic structure. A study by Sly et al. 2020 analysed the hardness of calcite crystals at different orientations and temperatures using nanoindentation (140). The findings from that study show the calcite grains which are parallel or subparallel to the c-axis are harder than those which are normal to the c-axis. They further tested crystals that were orientated between normal and parallel and found that their hardness range between the two extremes of orientation (140) (these are the results from the room temperature data only, as all experiments conducted for this thesis were at room temperature). Further testing by nanoindentation of the ala in the vertical axis will enable a better understanding of how the crystallographic orientation of these growth regions contributes to the protection of the organism, potentially whether harder surfaces in that direction contribute to function at the interlocking interfaces.

4.1.4.2 In-Situ Indentation, 4D analysis

3D evaluation of changes in the ala region upon loading via nanoindentation provides insight into the behaviour of the natural material under the challenging conditions that they live in, the high-energy intertidal environment (129,141). It highlights the relationship between the previously observed crystal structure difference between the inner part of the barnacle plate and the interface ala region (129).

Once reconstructed the scan data was analysed using Avizo 9.5 (Thermo Fisher Scientific). The X, Y and Z axis were all investigated. The X and Y axis allowed for clearer visualisation of the cracks formed from loading, as seen in figure 4.5. On initial investigation a pre-existing crack was found in the 0 mN load scan. This pre-existing crack enabled the investigation of the propagation of the pre-existing flaw showed that regular increases in load encourages crack growth. At 500 mN load a secondary crack was observed. At 750mN load the secondary crack appeared smaller and no growth in the primary crack was observed. At 1000mN load, complete failure was observed as the tip of the ala fell away from the barnacle plate.

In the Y axis the pre-existing flaw observed at 0 mN load was compressed on loading and no longer visible on incremental loading until 1000 mN where there was complete failure and the section of shell had fallen away.
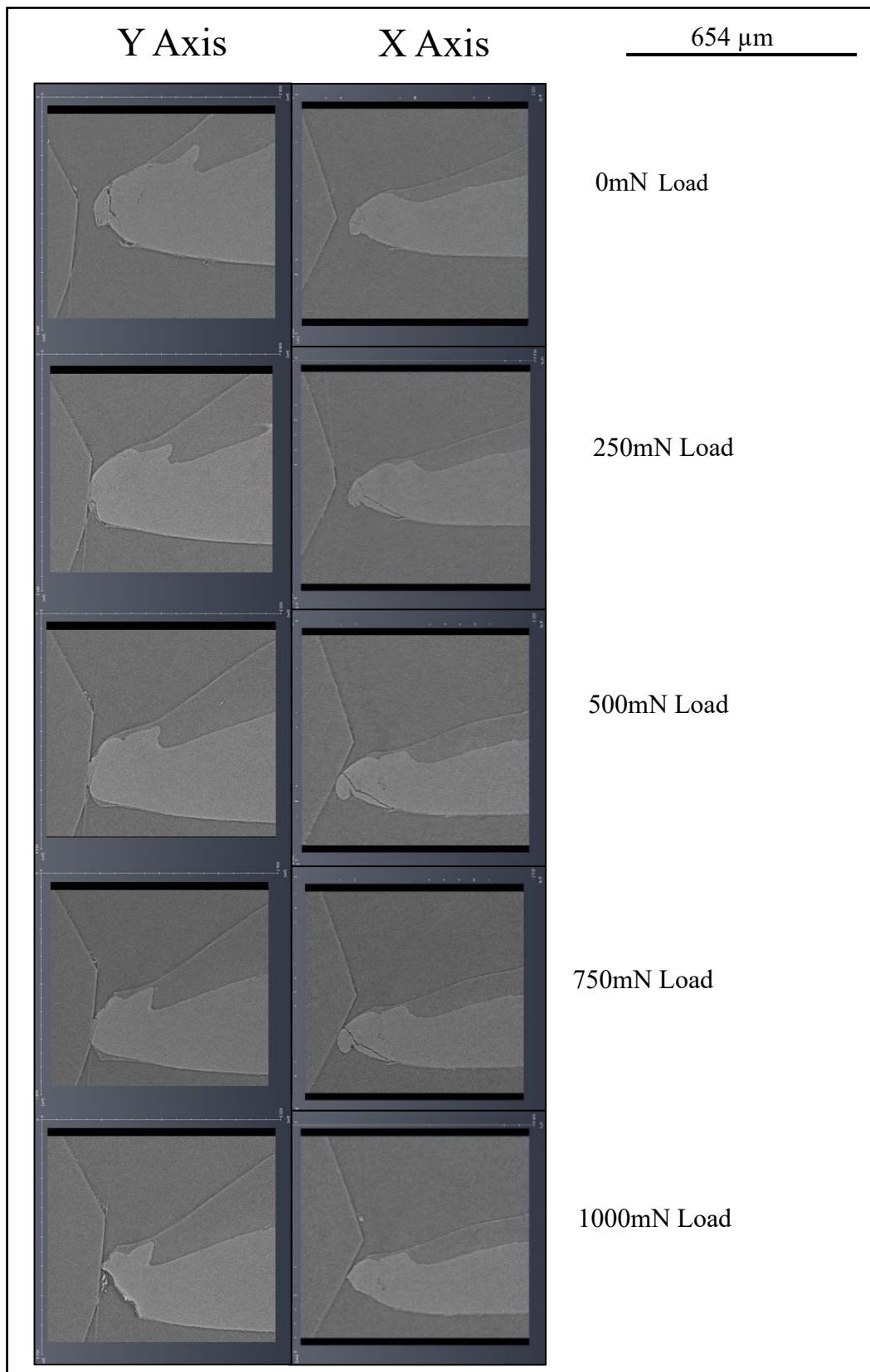
Figure 4.5. X and Y axis slices through the barnacle ala. Both the diamond Berkovich tip (left) and Ala are visible. The lateral movement is observed in the ala as the indenter tip slope pushed it on loading.

The location of the secondary cracks appears to be located out of or on the edge of the elongated crystal zone (129) approximately 118 µm from the edge of the ala. Mitchell et al, show that this region is not uniform along the tip (129). Figure 4.6 highlights the distance of the secondary crack observed at 500 mN loading.
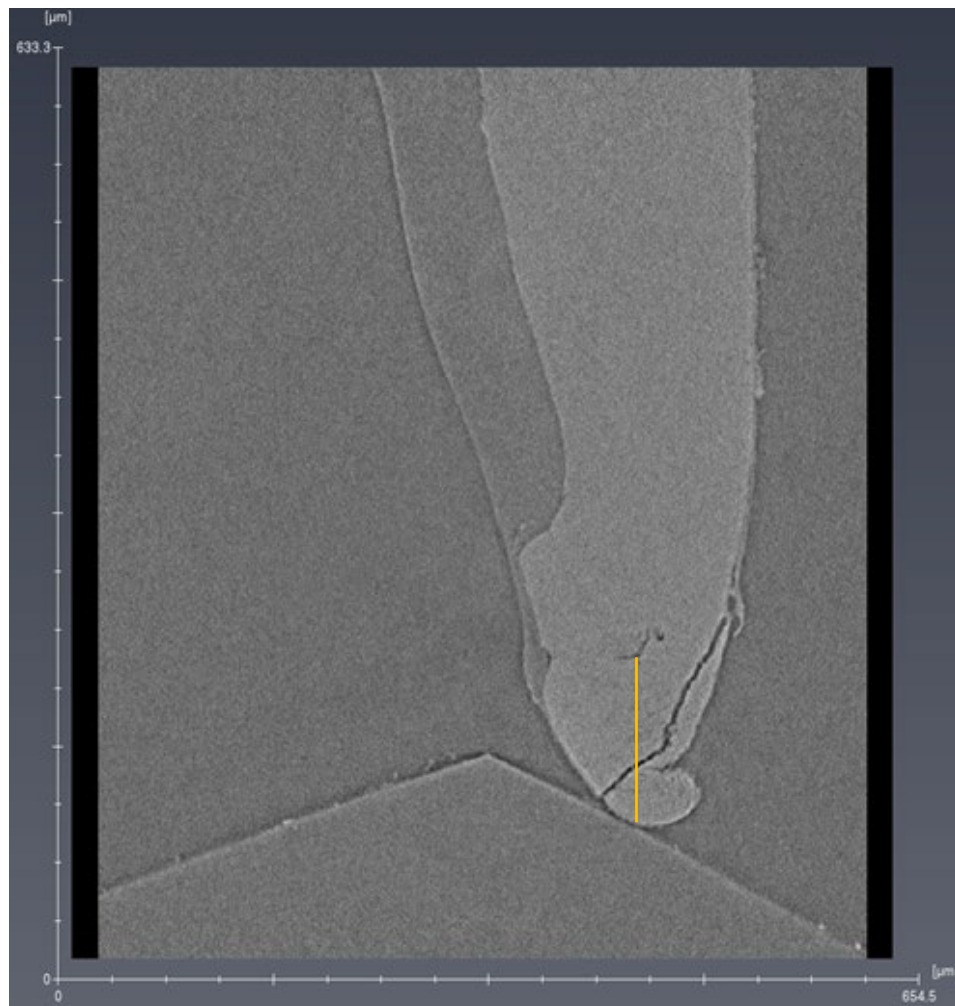

Figure 4.6. Location of secondary crack in the X axis at 500 mN load formed at 118.7 µm from the edge of the ala.

Previous literature found that while still occupied by the living organism the barnacle is able to recover from damage as the organism itself is integrated into the shell (138). Thus, it can be determined that the barnacle would be able to repair cracks formed in this region due to the increased presence of the organism's soft tissue in the pore network. This is incredibly interesting from a new, sustainable materials point of view if these mechanisms can be studied and replicated in human-made materials.

The formation of the secondary crack observed at 500 mN until past 750 mN loading reduced the growth of the initial crack observed in the plate before testing, suggesting that it was reducing the stress on the initial crack, preventing the total failure of the plate at the initial crack zone at a lower load. Although the rate of repair of barnacle plates is unknown the secondary crack may prevent failure of the plates from happening at lower loads to enable repair to begin in the damaged region.

To confirm the location of the secondary crack in relation the elongated crystal region in the plate may be difficult to complete. These regions are not uniformed and may be different from plate to plate. Due to this and the difficulties that will occur in attempting to expose the cracked cross-sectional surface for SEM-EBSD the average distance from the tip in work by Mitchel *et al*. was used as a reference distance in this work. They show that the elongated alae region ranges from approximately 25 μm – 90 μm from the tip (3). The location of the secondary crack at 500 mN loading was found to be at 118 μm from the tip.

As previously mentioned, variation may occur across different plates in the same organism and may occur between organisms of the same species based on growth, access to nutrients and age, etc. must be considered when averaging the distance.

Digital volume correlation was attempted with 3D data obtained from the in-situ testing. To perform this the files obtained from the scan which were in the .TXRM format needed to be converted to a .RAWW format for use in DaVis 10. This software operates by analysing the changes in size, shape and location of features in the internal microstructure during loading to provide strain and deformation measurements.

In the data obtained, there was no visible microstructure observed to be used. Although it is known that pores are present in the alae region of the barnacle (3), due to the achievable resolution of the scan these were not visible, therefore, this sample was unsuitable for digital volume correlation.

It is noted that the barnacle ala has moved laterally due to a very small misalignment with the tip of the indenter. Using another tip geometry could potentially resolve this issue. Either a wedge or flat punch shape would provide a larger contact area, reducing the possibility of this issue recurring.

The value of in situ indentation is that it is able to test non-flat (real life) morphologies, however there are some challenges, that come along with this. These challenges may involve manipulation for the size of the sample, i.e., cutting it to an appropriate size for the rig if the sample is too large. There is risk in cutting biological samples down as this process may cause damage to the internal microstructure, cracks, or delamination, which is the focus of study. Another challenge that faces 4D indentation testing is the length of time taken per scan, the scans performed in this study were all in excess of 14 hours as they performed in a laboratory setting. Laboratory based scans can be increased in time as longer scans will reveal a more detailed microstructure for analysis. The length of time for each of the scans performed in this study were a compromise between suitable times for a sufficient resolution, less noise and number loading steps, as two scans were performed at zero load 6 scans in total were performed for the final series of in-situ testing, and 4 scans for the preliminary testing. These can be overcome by using the IntraSpect 360 in a synchrotron. Use at a synchrotron can result in a better signal to noise ratio, and faster scan times. The shorter scan times open the possibilities of hydrated or semi-hydrated state testing by soaking the samples prior to loading and scanning, but this can still be difficult due to synchrotron causing drying and heating of samples even at faster scan times.

4.2 Antler

Dried, naturally cast antlers were analysed in this study, except for the Keats-M sample which was removed by the heard keepers after the velvet was shed. Antlers have been described as mirrors of life factors experienced by the deer during the period of growth (142); this includes the likelihood of survival of the calves during their first winter (128). As previously discussed, diet is a major factor in the growth of antlers, the milk received from the female from the point of birth to the second year of life has been known to contribute to strong growth and overall increased body mass of the deer (128). The following question had arisen from investigations of previous literature and communication with the herd keepers: Does the mineral provided by the lactating females, which is vital in calf survival, come at a sacrifice of their antler quality? This will be discussed in detail with the support of the results obtained.

The structure and properties investigated in this work provide an insight into how this natural material grown over a short time can perform to a high standard for its annual uses with different physiological demands. The workflow applied to the analysis of this sample constitutes the following techniques x-ray micro-CT, XRF, SEM, and nanoindentation.

4.2.1 X-ray micro-CT

The structure of antlers is greatly impacted by their short lives in nature, which does not undergo any remodelling during their lifespan (143). X-ray micro-CT allowed for the non-destructive visualisation of the internal structure of the antler main beam regions for two samples in the M category and one in the FWC category. Figure 4.7 shows the FWC scan of the lower junction of the main beam, the burr, and the junction for the brow tine. Figures 4.11 and 4.12 show images of the main beam of the two M-category samples. On visual observation of these preliminary scans, both M samples appear to display a thicker cortical region than the FWC sample. This may be due to the added mineral demand of calving meaning that there will be fewer minerals that are usually prioritised for antler growth, therefore the cortical region will be thinner for the FWC group. Due to not having the demands of calving it would be predicted that the FNC category will have a similar structure to the M antlers with a thicker cortical region and abrupt transition to the trabeculae.

Unfortunately, due to unforeseen circumstances with the Nikon X-Tek XT H225 Micro-CT, it was out of operation for an extended time which resulted in not all samples being able to be scanned. Preliminary scans were performed on three samples Ibex, Carnethy, and Keats of a low resolution to visualise the internal cortical and trabeculae regions. For these preliminary scans no female without calf samples were analysed as they were not yet sent by the reindeer herd to the lab.

Therefore, this section will detail the intended work to be completed on all the antler sections with a higher resolution.

The samples would be analysed with BoneJ which is a plug-in for ImageJ specified for bone analysis.

All samples from the three groups detailed previously M, FWC and FNC will be scanned. The parameters to be compared would be average cortical region thickness along the length of the main beam to observe any differences between groups.

Another feature to be examined would be the ratio of bone to total volume or area volume fraction, where the fraction of bone in the image is calculated. BoneJ accomplished this by counting the voxels in the foreground, which is assumed to

represent bone, it will then compare it to the total number of voxels in the image. This gives the volume of mineralised bone per unit volume (134).

Figure 4.7 is a slice of the preliminary scan of the pedicle and main beam region of Ibex - FWC this 3D visualisation was completed with ORS Dragonfly. It clearly shows the internal microstructure of the bone with the cortical and internal trabeculae region. This sample shows a large volume of trabeculae to cortical bone. It is seen in this sample that the transition to the trabecular bone from cortical bone is more gradual than exhibited in human bone.
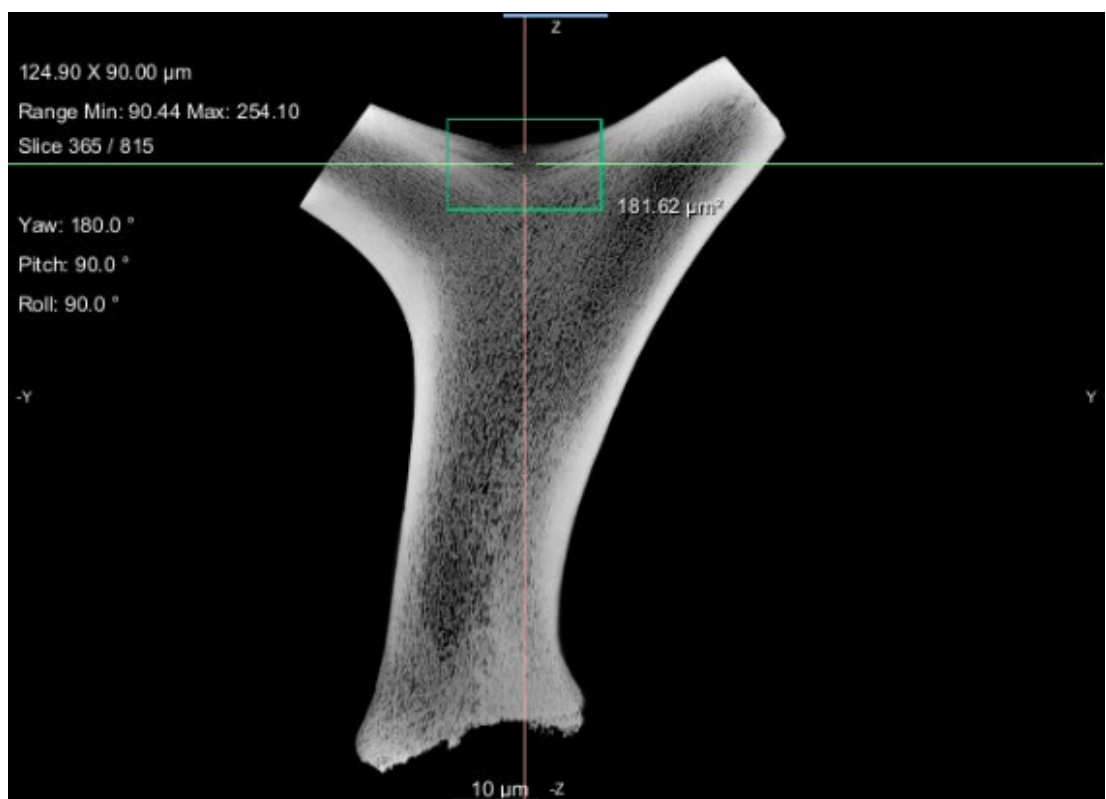

Figure 4.7. A slice through Ibex-FWC pedicle reconstructed on ORS Dragonfly. The cortical and trabeculae regions are visible in this slice.

A slice through a 3D section of the main beam of Carnethy – M antler is shown in the figure 4.8 in this figure it has been noted that there is a thicker cortical region compared to Ibex- FWC antler and the transition to trabeculae bone is also comparatively more abrupt with a comparatively smaller trabeculae region. This was also visualised using ORS Dragonfly.

Figure 4.8. A slice through a 3D volume Carnethy-M main bean section where the cortical and trabeculae regions are easily visible.

Keats-M main bean section, shown in figure 4.9 visualised with ORS Dragonfly, has similarities with the Carnethy-M sample where in comparison to Ibex-FWC the cortical bone region is significantly thicker as well as having an abrupt transition to trabeculae bone of which there is also a smaller area occupied by trabeculae bone than the Ibex-FWC sample.

It should also be noted that Keats's antlers were not naturally shed. They were removed by the keepers of the herd after the velvet was shed to prevent injury to himself.
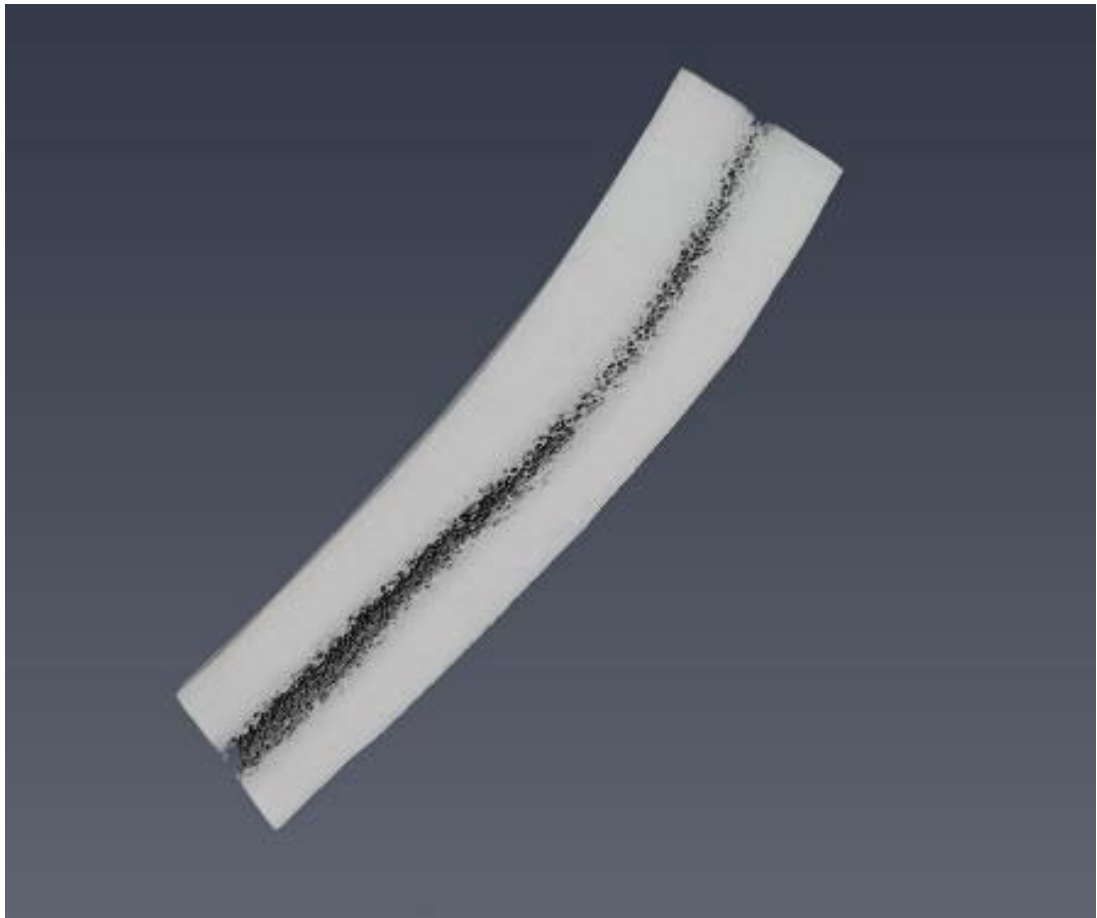
Figure 4.9. Slice through a 3D section of Keats-M antler main bean section where the cortical and trabeculae regions are easily visible.

The differences in cortical thickness, transition to trabeculae, and average volume of bone in general and after the initial investigations presented, the volume of trabeculae within the samples could provide insight into the difference between the categories studied M, FWC, and FNC. The two M samples show a thicker cortical region and the FWC had a thinner cortical region and larger trabeculae area.

 Further analysis is required, with more samples scanned to a better resolution to visualise the trabeculae in more detail to allow for analysis with BoneJ. Comparisons will also need to be made with the FNC category as the anatomical differences observed may be due to the female calving that year and a change prioritisation of minerals.

To investigate the role of mineral supply in cortical region thickness, further X-ray micro-CT scans of all samples within the FWC, M, and FNC groups will be necessary for comparison as the other groups do not have this additional mineral demand for growth. Female reindeer begin antler growth after calving in May during this time they are producing milk for their calf.

X-ray micro-CT will also be a valuable technique in the analysis of variation in the morphology and histology along the length of the main beam of the antler. This will require the thickness of the cortical regions which will affect the diameter of the trabeculae, which in bone is found to accommodate stresses from different directions, whereas cortical bone can accommodate stress mostly in a single direction (144). Further analysis is required, with more samples scanned to a better resolution to visualise the trabeculae in more detail to allow for analysis with BoneJ. Comparisons will also need to be made with the FNC category as the anatomical differences observed may be due to the female calving that year and a change in prioritisation of minerals.

Scans along a long section of the main beam as in Figures 4.8 and 4.9 would be preferred for this analysis to provide a better representation of the dimensions along the antler main beam, this could not be performed in the Carl Zeiss Versa also available in AIM, due to the asymmetry of the antler and the relatively small field of view available. The Nikon X-Tek is a device that has sufficient space in the chamber and a larger field of view.

4.2.2 X-ray Fluorescence

XRF was selected as the method for chemical analysis of reindeer antlers as it has been applied in different settings particularly for antler analysis, more recently for the identification and protection of different species in India (145).

After the samples were tested a standard report was generated, as this reporting format allows for each element detectable in the range to be displayed by the device and downloaded via direct connection between the instrument and the user's laptop. The data was saved as a .csv for use as an Excel file this enabled comparative analysis between samples.

To compare the mean values across the three categories the average values obtained for the Ca and P values were plotted. The average Ca, P and Mn concentration in percent across the cross sections, from table 4.1, was calculated. Average FWC: P = 18.1% Ca = 49.9%, FNC: P = 21.7% Ca = 49.4%, M: P = 21.7% Ca = 49.6%. From the average values there were no significant differences in calcium (Ca) composition between the three categories all were within the range of 49.4 – 49.9%. In comparison for the Phosphorous (P) composition there was no significant difference between the FNC and M categories however there was a 16% difference in phosphorus composition between FWC and the FNC and M categories, this is shown in Figure 4.10 (a) and (b).

The third element on interest was Mn due to, form the literature, its presence in antler having contributions to work to peak force and increased cortical thickness (146). Figure 4.10 (c) shows the differences between the average Mn values across the three categories, FWC: Mn = 0.011 %, FNC: Mn = 0.012 %, M: Mn= 0.03 %. Due to the possible heterogeneity of Mn across the surface the error in detecting Mn in the cross section has been found to have an extremely wide range.

Sample name	P %	±	Ca %	±	Mn %	±
Oatcake FWC	20.15	0.0062	50.86	0.048	0.02	0.007
Oatcake WC 1	19.18	0.064	50.79	0.051	0.03	0.006
Oatcake FWC 2	20.06	0.062	50.85	0.048	0	0
Average % composition	19.7966667	0.044067	50.83333	0.049	0.016667	0.004333
Brie FWC	21.03	0.059	50.77	0.045	0	0
Brie FWC 1	21.7	0.057	50.48	0.043	0.02	0.005
Brie FWC 2	21.48	0.056	50.3	0.042	0	0
Average % composition	21.4033333	0.057333	50.51667	0.043333	0.006667	0.001667
Jenga FWC	18.81	0.08	44.46	0.06	0.07	0.014
Jenga FWC 1	20.11	0.073	45.35	0.054	0	0
Jenga FWC 2	20.19	0.074	45.67	0.055	0	0
Average % composition	19.7033333	0.075667	45.16	0.056333	0.023333	0.004667
Dante FWC	16.43	0.067	51.82	0.058	0	0
Dante FWC 1	16.36	0.072	55.16	0.063	0	0
Dante FWC 2	16.3	0.068	53.17	0.059	0	0
Average % composition	16.3633333	0.069	53.38333	0.06	0	0
Sika FWC	17.32	0.07	50.28	0.058	0	0
Sika FWC 1	15.06	0.073	51.03	0.065	0.04	0.011
Sika FWC 2	14.7	0.073	51.18	0.066	0	0
Average % composition	15.6933333	0.072	50.83	0.063	0.013333	0.003667
Ibex FWC	0.28	0.028	50.08	0.045	0.02	0.006
Ibex FWC 1	23.25	0.063	48.16	0.045	0	0
Ibex FWC 2	23.2	0.065	48.68	0.047	0	0
Average % composition	15.5766667	0.052	48.97333	0.045667	0.006667	0.002
Caterpillar FNC	21.45	0.063	48.14	0.046	0.03	0.006
Caterpillar FNC 1	21.8	0.063	48.19	0.046	0.03	0.006
Caterpillar FNC 2	21.31	0.065	49.95	0.049	0.03	0.007

Average % composition	21.52	0.063667	48.76	0.047	0.03	0.006333
Angua FNC	22.36	0.057	48.37	0.041	0	0
Angua FNC 1	21.52	0.057	44.02	0.039	0	0
Angua FNC 2						
Average % composition	21.94	0.057	46.195	0.04	0	0
Galilee FNC	21.91	0.06	49.65	0.045	0	0
Galilee FNC 1	21.82	0.059	50.03	0.044	0.02	0.005
Galilee FNC 2	21.31	0.059	50.07	0.045	0	0
Average % composition	21.68	0.059333	49.91667	0.044667	0.006667	0.001667
Closau M	21.33	0.061	49.98	0.046	0.02	0.007
Closau M 1	20.48	0.064	50.82	0.05	0.03	0.007
Closau M 2	21.31	0.061	50.18	0.046	0.02	0.006
Average % composition	21.04	0.062	50.32667	0.047333	0.023333	0.006667
Frost M	21.74	0.057	48.66	0.042	0	0
Frost M 1	22.14	0.056	48.9	0.041	0	0
Frost M 2	22	0.057	48.63	0.042	0	0
Average % composition	21.96	0.056667	48.73	0.041667	0	0
Sher M	21.98	0.058	49.8	0.044	0.02	0.006
Sher M 1	21.61	0.058	48.27	0.043	0	0
Sher M 2	22.42	0.058	50.78	0.044	0	0
Average % composition	22.0033333	0.058	49.61667	0.043667	0.006667	0.002

Table 4.1. Percentage composition and averages of P, Ca and Mn in the antlers scanned from the different groups. The samples are also labelled as to which group, they belong to FNC, FWC, M.
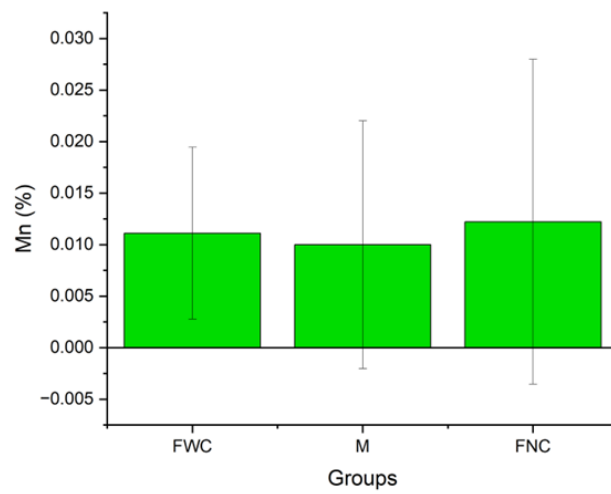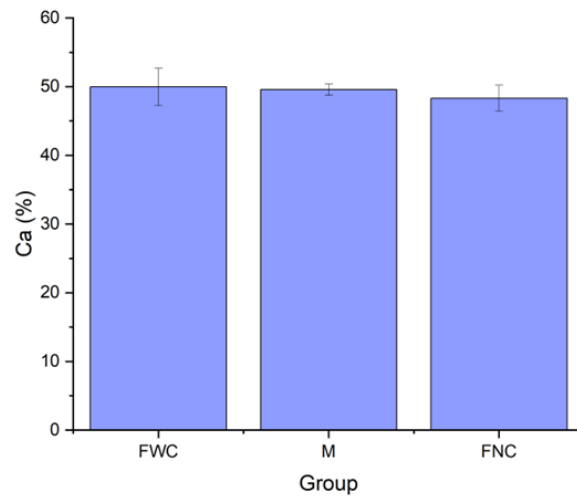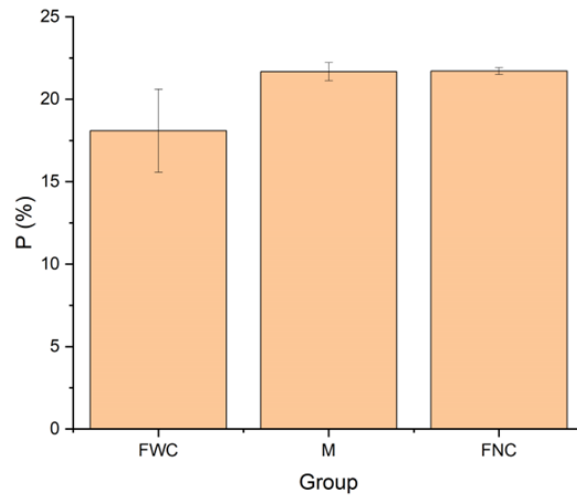
Figure 4.10. Charts showing average percentage composition of (a) P (b) Ca and (c) Mn of all scanned samples in the three groups FWC, M, FNC.

A 3-way ANOVA was performed on the data obtained for Ca, P and Mn, to compare the three groups (FWC, M, FNC). From the analysis there was no significant statistical differences found between any of the groups. Suggesting that although there is a change in demand for the FWC group the chemical composition of the antlers remains consistent.

Although not determined to be significant by statistical means the P percent composition of the FWC category is 16% lower than the M and FNC categories.

Previous studies found that Mn concentrations using XRF were also low and described to be present in traces when analysing solid and powdered antlers of different species (145). This has also been found in this study where Mn in the cross-section of the antler samples was low in all three categories with **FWC:** Mn = 0.011%, **FNC:** Mn = 0.012%, and **M:** Mn= 0.03%. Comparing the results obtained in XRF testing to previous literature the higher the concentration of Mn relates to a thicker the cortical region (146).

The method of testing with XRF assumes that there is a homogenous distribution of the elements throughout the sample being tested (136). Previous literature has stated that Mn is not evenly distributed in the cross-section of antlers and there exists the possibility that due to this, Mn presence could be simply missed in testing some samples leading to lower average values (136). To show the validity of using this method for the detection of elements SEM-EDS was used in conjunction as a key part of the workflow.

4.2.3 Scanning Electron Microscopy

SEM-EDS was performed on one sample from each of the categories to detect the distribution of the elements Ca, P and Mn.

The three sample sections were analysed under variable pressure settings therefore they did not require carbon coating. Images were taken of the areas mapped; these are displayed in figure 4.11. Depending on the sample requirements different kV settings were used to enable better visualisation (a), Clouseau - M shows a section 364.1 μm 20 kV was used to visualise the area showing the microstructure of the cross-section Haversian systems are clearly visible here as well as the lamellar formation of the tissue surrounding the canals.

Galilee – FNC (b) shows a significantly larger region with a 1.644 mm width of 15 kV was used to visualise the area. This region gives a clear overview of the organisation of the cortical region of the antler bone with its compact nature and distribution of Haversian systems across the cortical region are even with the presence of elongated regions in the outermost region. This may be an alternative morphology of a Haversian system; further investigations will be required to confirm this.

The region analysed for Oatcake - FWC (c), was 2.037 mm in width and 15 kV was used. The area, like that of Galilee, shows the cortical region for the outermost region. The distribution of Haversian systems is also evenly distributed however the elongated pore area observed in Galilee's sample is not observed in Oatcake's sample. However, the elongated regions are distributed through the cortical region.

Analysis of the elongated regions present in the Galilee - FNC and Oatcake - FWC samples with x-ray micro-CT will provide much more detail into the morphology of these features in 3D. As in the x-ray CT images captured previously it was observed that the other FWC samples had a smaller cortical region and a more gradual transition to the trabeculae.
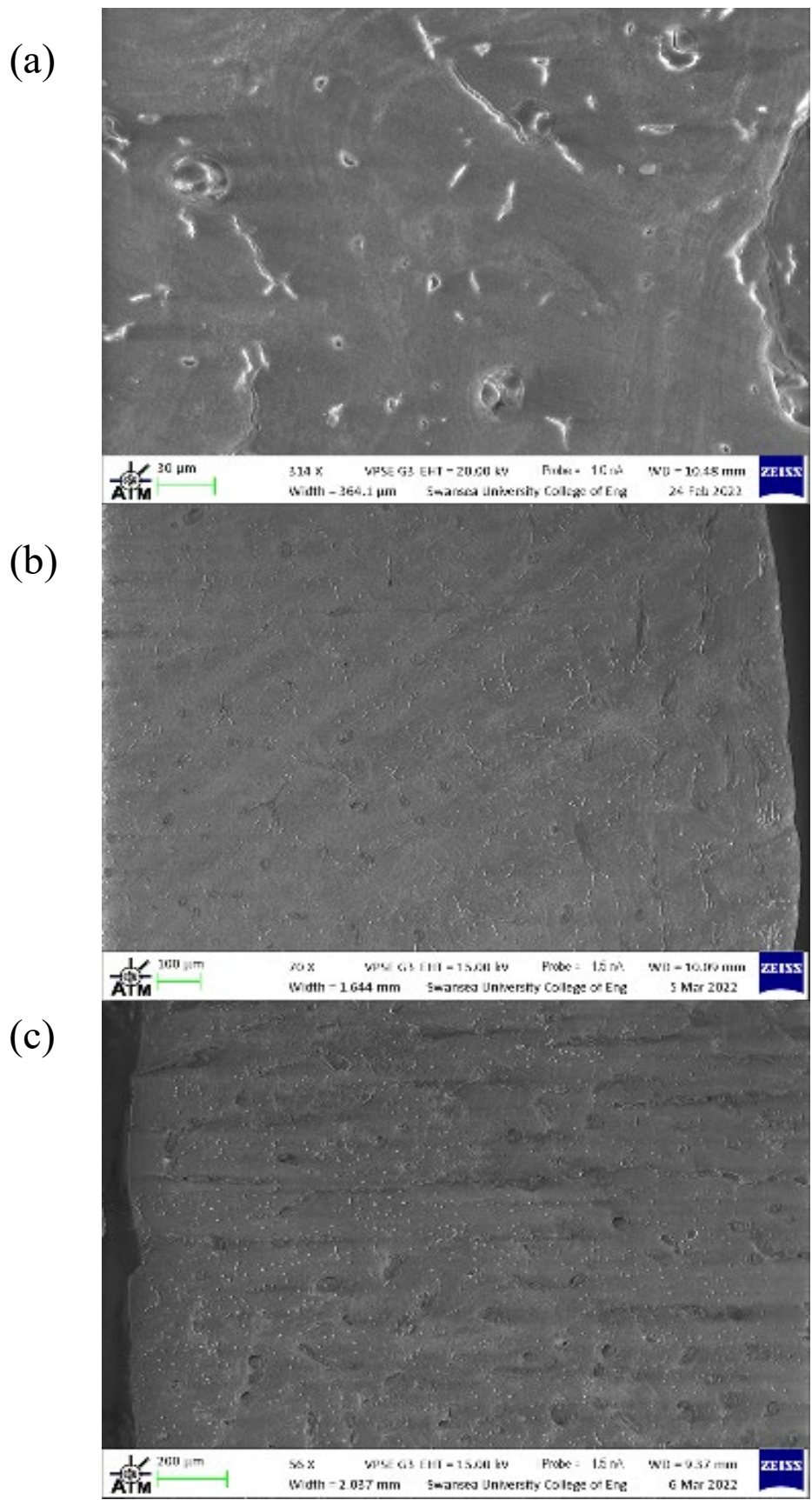
Figure 4.11. SEM images of the three site maps reported for EDS mapping on antler samples. (a) Clouseau - M, (b) Galilee - FNC and, (c) Oatcake - FWC.

4.2.5 Energy Dispersive Spectroscopy

EDS was used in this study to verify the use of XRF for the detection of minerals on the cross-sectional surface of the antlers.

Upon analysis of the XRF data there were inconsistencies with the presence of Mn in the cross-section with some regions of the same sample having Mn present and others there was no recorded presence. Therefore, it was decided to use EDS to evaluate the heterogeneities of the elements Ca, P and Mn across the surface of the samples where Mn was present.

Multiple line scans were performed across the cross-sectional surfaces of all 3 samples to observe any differences in the composition of Ca and P specifically in the cortical region of the antler as well as to detect any traces of Mn. All the scans show uniform distribution of Ca and P where the antler sample was present. However, Mn was not detected in any of the samples.

Clouseau was investigated in 6 locations the lines for analysis covered varying lengths. Figure 4.12 shows a 900 μm length scan across the cortical region of the antler cross section from Clouseau wherever the antler material was present the Ca and P counts were consistent and did not show a large degree of variation, where pores were present the counts dropped drastically as there was no sample present.
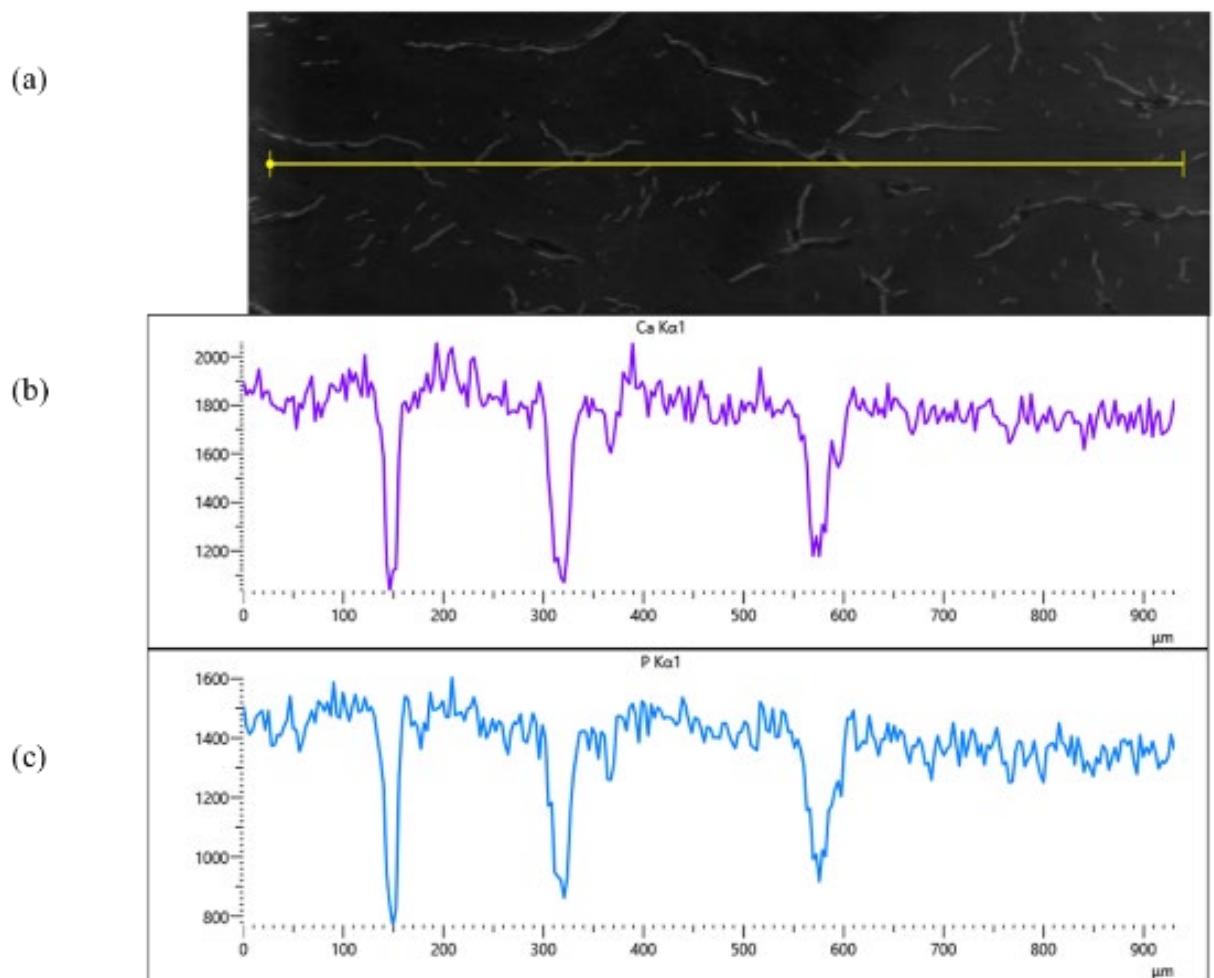
Figure 4.12. 900 μm line scan on Clouseau-M sample (a) SEM image and a line showing the area covered by the scan. (b) Graph displaying the number of counts of Ca in the area scanned (c) The P counts along the scan length.

On the Galilee - FNC sample 7 sites were scanned using line scans to sample and it was found that where the antler tissue was present there would be consistent levels of Ca and P and as observed on the Clouseau sample Mn was not detected in any of the scans. The only feature that greatly reduced the number of counts was the lack of antler tissue, either due to pores cracks or the end of the sample. Figure 4.13 shows an 1150 μm line scan from Galilee, it clearly shows the consistency of counts of Ca and P where a sample is present from correlation with the SEM line the locations of the features, and the corresponding drop-off in counts is observed.
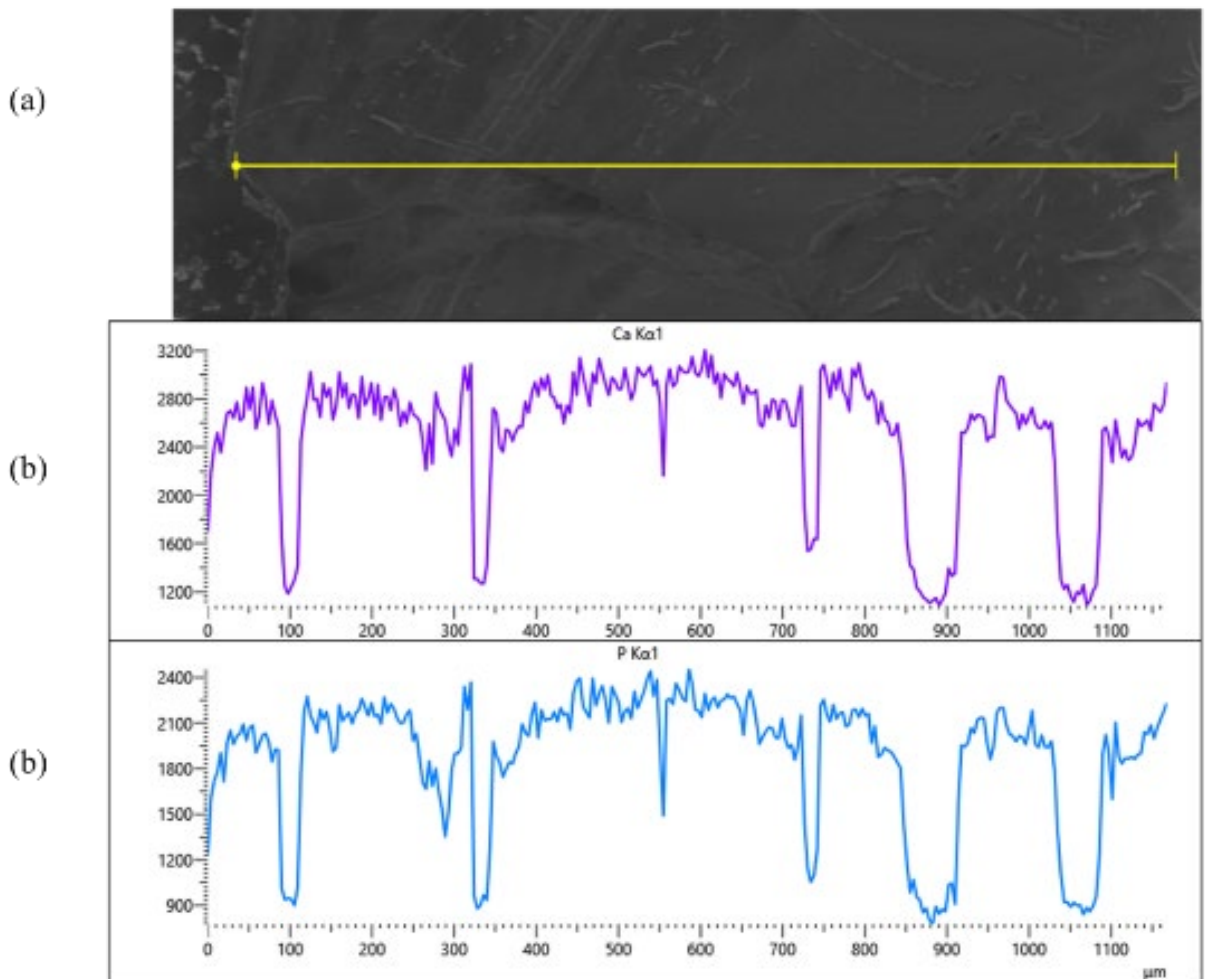
Figure 4.13. 1150 μm line scan on the Galilee – FNC sample (a) SEM image and the line showing area covered by the scan covering several features. (b) Graph displaying the number of counts of Ca in the area scanned (c) The P counts along the scan length.

Oatcake as with the previous samples showed consistency with Ca and P counts from scans along 7 sites with no Mn detected. Figure 4.14 shows a line scan of length 1450 μm, this line intersected multiple pores, and centres of Haversian systems, similarly to the previous samples there is an immediate drop in counts of Ca and P where no antler tissue is present and where the antler tissue is present the counts are similar and show little variation. Shallow pores are also visible in scans of all samples these are observed in the graph of element counts.
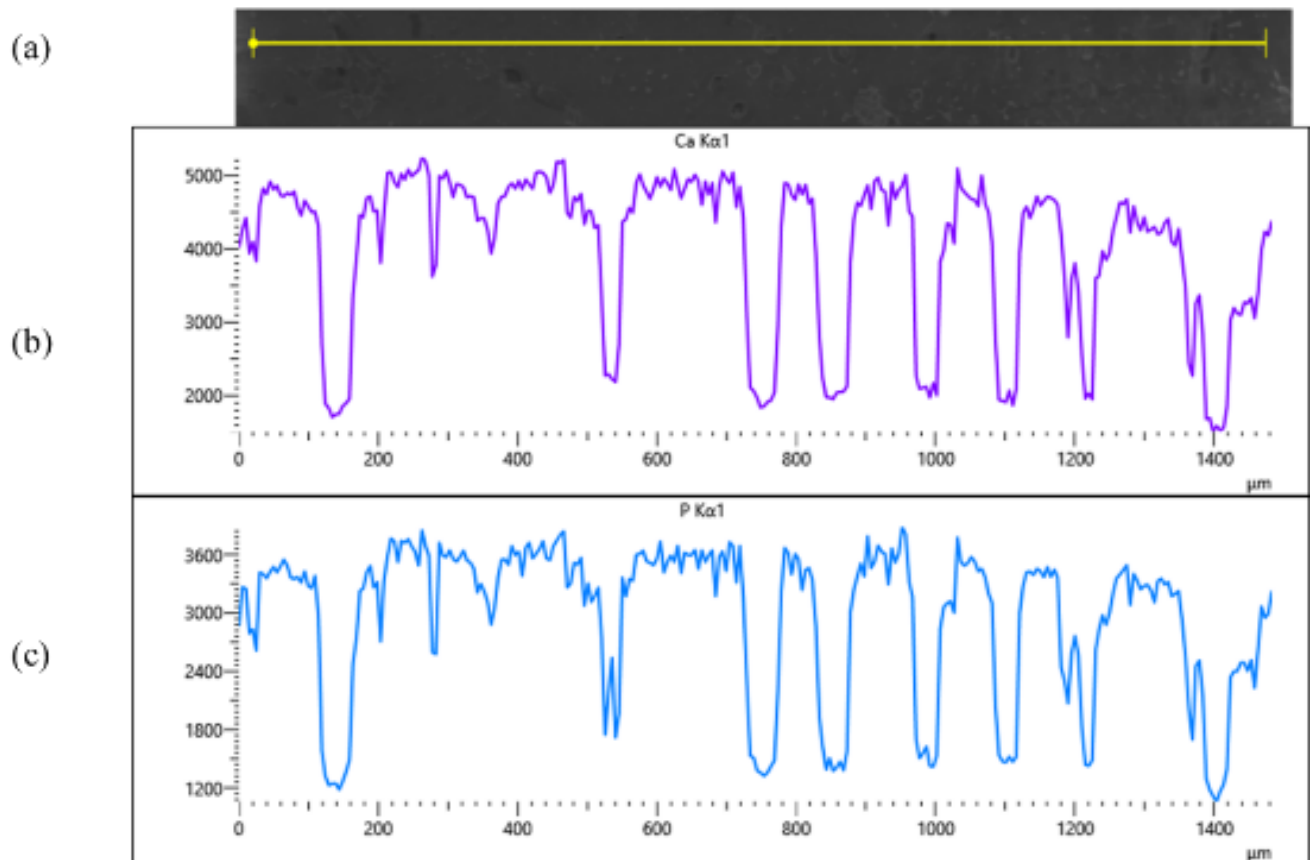
Figure 4.15. 1450 µm line scan on the Oatcake - FWC sample (a) SEM image and line showing the area covered by the scan covering several features. (b) Graph displaying the number of counts of Ca in the area scanned (c) The P counts along the scan length.

Areas of the cortical region of the antler were also mapped to detect the presence of Ca P and Mn. The maps were taken from the SEM regions in figure. The maps show a very uniform presence of Ca and P. The pores are easily visible as dark holes as there is no antler tissue present. Mn was not detected in any of the mapped regions on all 3 samples, the image received for Mn maps were blank. Figure 4.15 shows maps of all three samples with the presence of Ca and P being so uniformed across the surfaces of each it the morphology and distribution of the Haversian systems in the Galilee and Oatcake samples, as initially observed in figure 4.11, are more visible. With Oatcake – FWC (c) the elongated systems are spread through the area while on the Galilee – FNC map the elongated morphology is only observed along the edges.
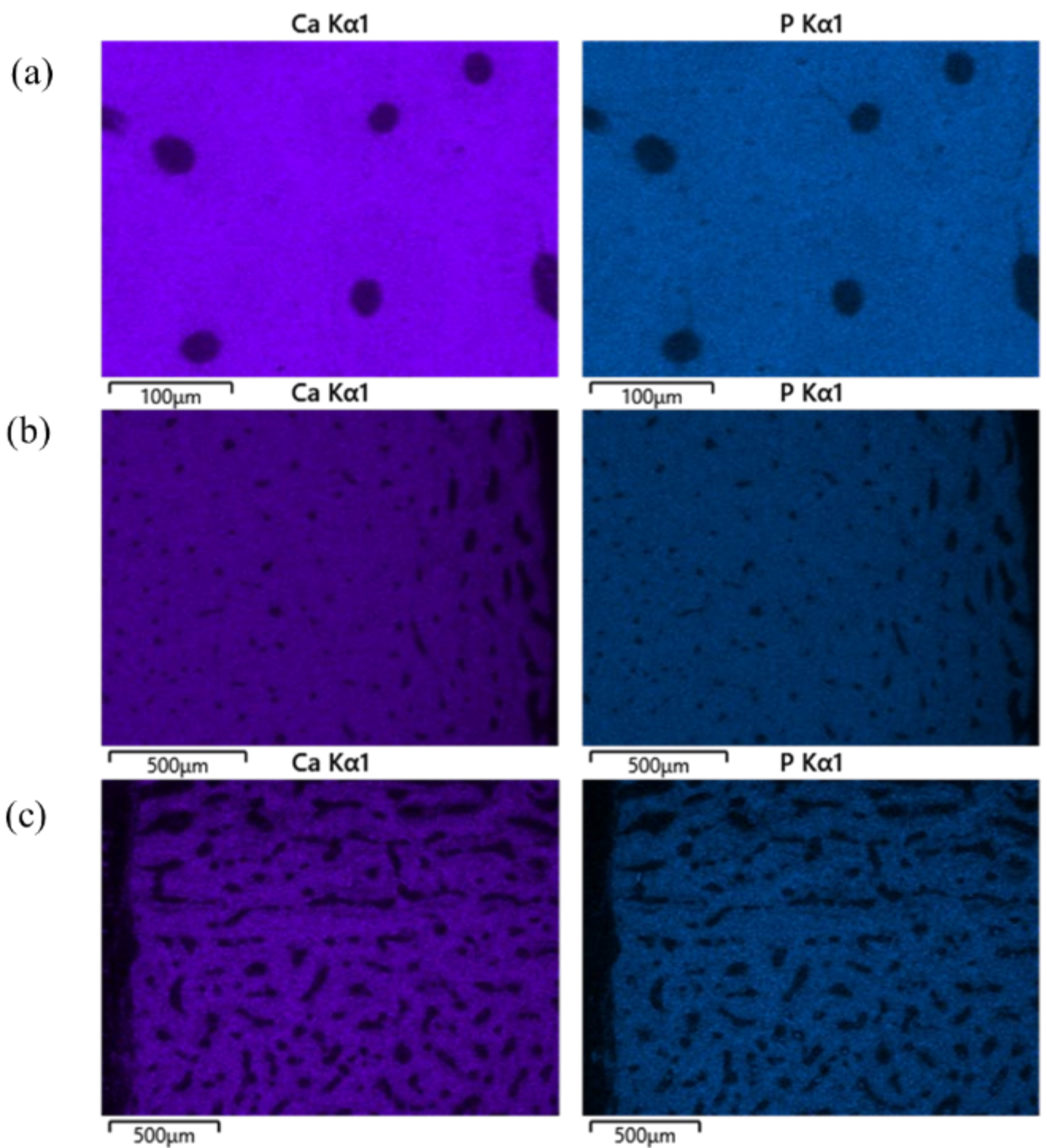
Figure 4.15. EDS Maps from three samples showing Ca and P distribution across the sample surface. (a)Clouseau -M, (b)Galilee- FNC and (c)Oatcake- FWC.

It was determined the Mn levels that were detected by XRF were too low to be detected by EDS. Wavelength dispersive spectrometry (WDS) was considered to achieve the detection levels to detect Mn in the antler samples, however, upon consultation information was obtained that the Mn levels detected from the cross sections of the samples in XRF were too low for WDS analysis as well.

EDS is sufficient to determine that XRF is suitable for accurate testing of the Ca and P composition of antlers. The results clearly show a uniform distribution of Ca and P across the cross-sectional surface which was also observed in a study of antler tines by Kierdorf et al. using similar methods (143). The concentrations of Mn were not detectable by SEM-EDS although small amounts were found in XRF.

4.2.4 Nanoindentation

4.2.5.1 Traditional Indentation

The application of nanoindentation on reindeer antlers was performed to establish an understanding of the mechanical properties of the mineral phase of the antler bone of the reindeer, particularly if there exists any difference between antlers of male (M) and female reindeer. Additionally, it was investigated whether if a female was calving there would be an impact on the mechanical properties of the antlers (female with calf -FWC, female without calf – FNC). Comparison of these three groups is of interest since the selective pressures of the sexes are different from each other, therefore so too is the resource allocated towards them (147). The additional pressure of raising a calf may also impact resource allocation due to the high costs of gestation and lactation which has been found to impact antler length (147).

As the antlers were tested in both the cross and transverse section both sets of data will be used for statistical comparison. Figure 4.16 displays the data of the average hardness and modulus values of all antlers tested on both the cross (X) and transverse (T) sections. The average hardness values obtained for the three categories, shown in figure 4.19 (a) were: FWC = 0.419449 GPa, M= 0.432261 GPa, FNC= 0.391465 GPa on the cross-sectional surfaces, and for the transvers sections the average hardness for each category was: FWC = 0.443019 GPa, M= 0.373816 GPa, FNC= 0.449336 GPa. Figure 4.19 (b) shows the average modulus values of all three groups on both the cross and transvers sections. The average modulus values for the cross-section samples were FWC= 14.39308 GPa, M=14.85138 GPa, FNC= 13.04855 GPa. The values for average modulus transvers section are: FWC = 10.76997 GPa, M = 9.976577 GPa and, FNC = 11.4379 GPa.
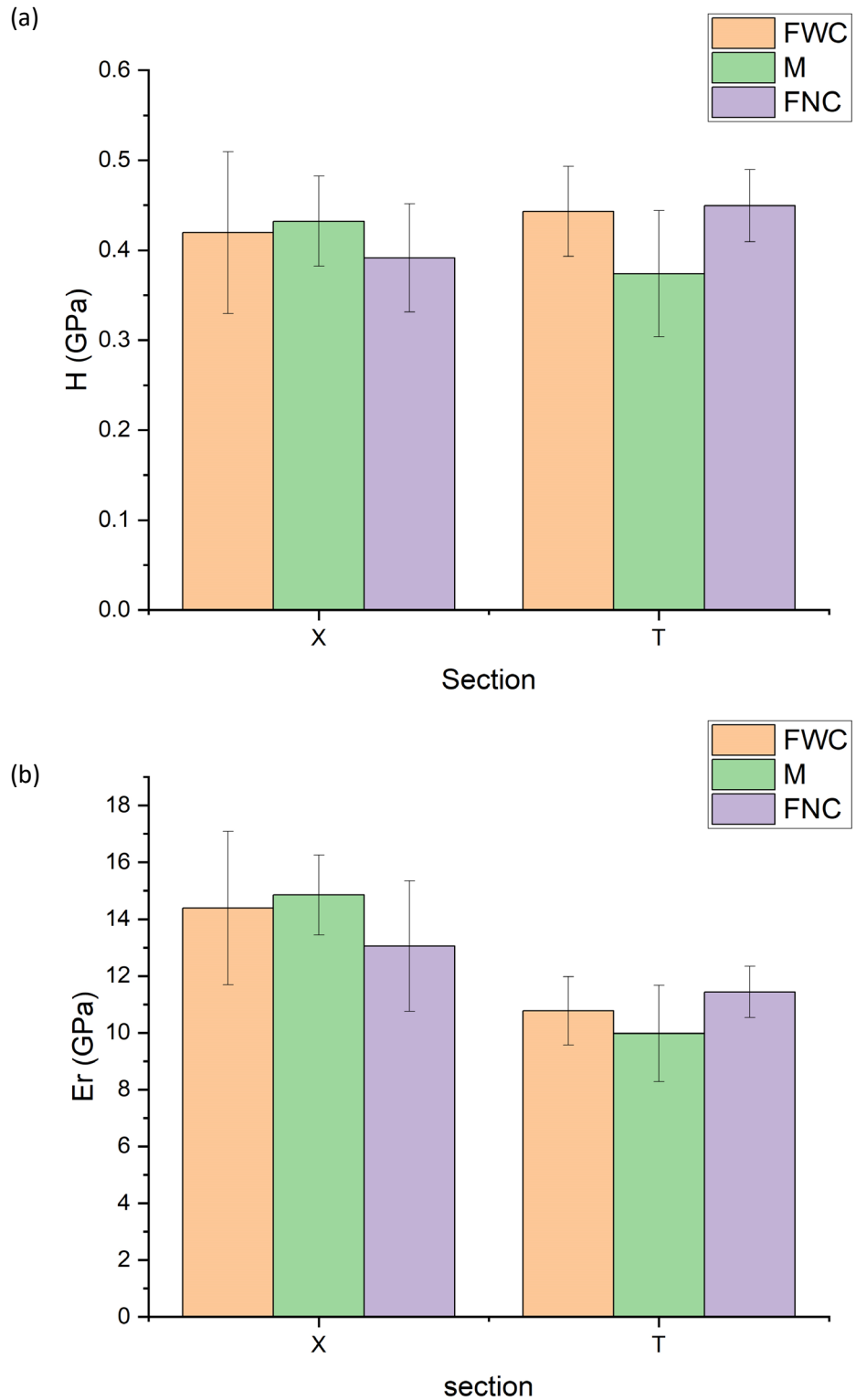
Figure 4.16. Chart displaying the average hardness and modulus values for the three groups (FWC, M, FNC) int eh cross (X) and transverse (T) sections.

Figure 4.17 displays the distribution of the averages of each sample tested in the cross and transverse sections and sectioned into their groups. This shows that although there are differences between the median values, they appear to not be significantly

different. A 3-way ANOVA was performed to determine the if there were any significant statistical differences between each of the data sets presented in figure 4.20. The 3-way ANOVA found that there were no significant differences between any of the three groups in either the cross or transverse sections.
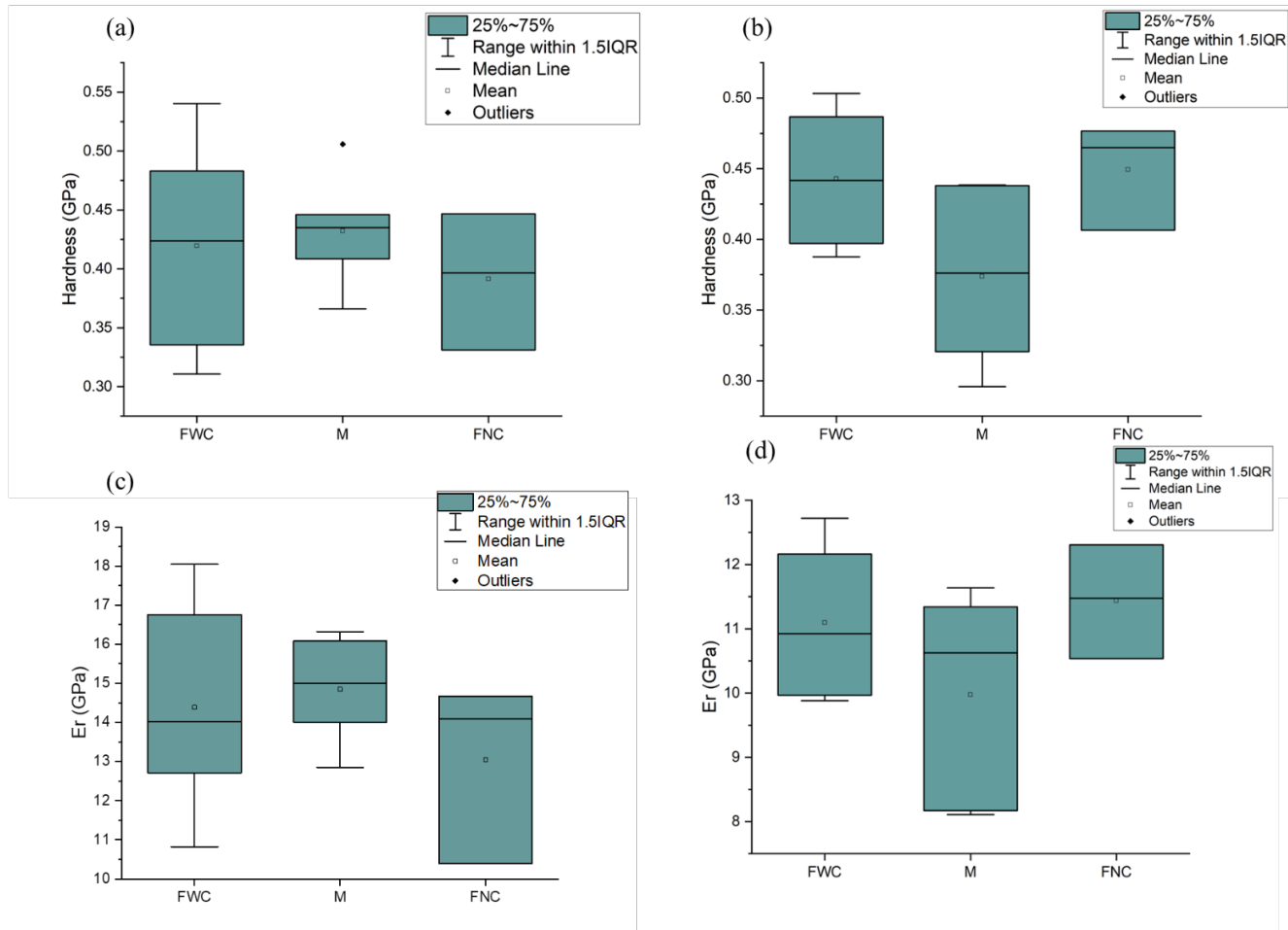

Figure 4.17. Box plots showing the distribution of the averages of all the samples allocated into their respective groups. (a) Hardness in the cross-sectional direction(b) Hardness in the transverse sectional direction (c) modulus in the cross-sectional direction (d) modulus in the transverse sectional direction.

It can be determined from the data that between the sexes and calving status there was no compromise in the nanomechanical properties of reindeer antler as no significant differences were found between groups in both the cross and transverse sectional data. Although, for females it is understood that calving has an additional resource allocation in minerals. It is understood that additional resource costs affect the length of the antlers only and does not affect the properties of the antlers.

Some research has been performed previously about the effect of lactation on the growth of male deer antlers, in that the consumption of maternal milk greatly increases their growth as well as the concentration of Ca and P and over antler weight (148,149). However, very little has been done to determine the effect of calving on female reindeer mothers on the properties of their antlers.

This study aimed at analysing the differences between the sexes and calving status of reindeer this included the nanomechanical properties. Nanoindentation found that the average hardness of the different categories was found to have no statistical significance between the differences in the hardness and modulus values in both the transverse and cross sections. This correlates with the data obtained in XRF where there were no significant differences in the mineral content between the sexes and calving status as a reduced mineral content would result in a reduction in hardness and modulus of the reindeer antlers which would increase their ability to bend under applied forces. If the properties were reduced it would therefore make the antlers unfit for their purpose, fighting. This is similar to the reason that antlers are used for fighting in the dry state and not hydrated state, i.e., that they will bend under loading not giving the advantage to the reindeer. Growing inefficient antlers due to a change in biological mineral demand would be seen as an evolutionary disadvantage possibly a waste in resources for the reindeer, therefore it is possible that the mineral content is kept consistent but the micro- and macrostructure, such a size, beam thickness, and number of tines is adjusted to ensure that the antlers grown are suitable for fighting for the three categories analysed in this study.

In the results across the three categories there is a large degree of variation, this could be due to that fact that the antlers were obtained in different years, as discussed previously diet has a major impact on the composition of the antlers this is greatly affected by annual weather as the herd from where the antlers were obtained are free ranging. Particularly poor weather in one year would result in less food on the hills where the reindeer will spend their time. A larger sample number for each category will be able to help observe if the differences in variability is outside of factors being considered in this study.

4.2.5.2   Accelerated Property Mapping

4.2.5.2.1   Transverse-section

The SPM shown in figure 4.18 shows the alternating dark and light bands of the lamellae present around the haversian system in the transverse section highlighted in the optical image in figure 4.20.

SPM was performed on the lamellar regions of the antler cortical bone to better visualise the direction of the collagen fibres on chich Ca and P mineralise. The differences in the directionality of the collagen fibres are known to defect cracks and arrest propagation. This is unlike other natural materials such as sea sponge spicules that utilise differences in modulus to prevent crack propagation which has been harnessed in innovative composite structures (150).

The light bands represent the regions where the collagen fibres are perpendicular to the surface, and the dark bands represent the regions where the collagen fibres are not perpendicular to the surface. Further research into the direction of the fibres in the dark regions will provide greater insight into the how the differences between the properties of the fibres at different angles change.
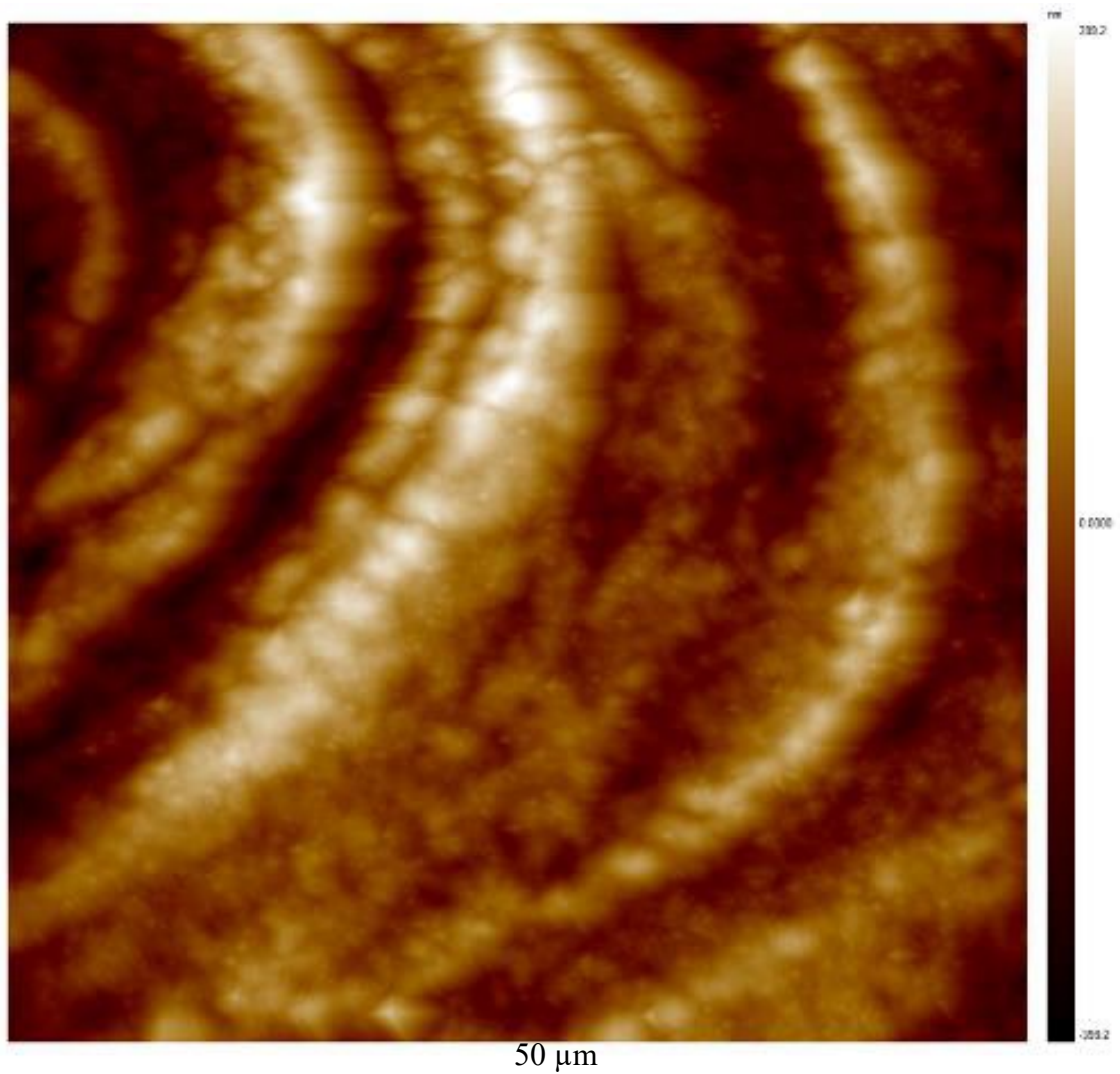
50 μm

Figure 4.19. Topographical SPM of a 50 μm x 50 μm area on the transverse face of an antler sample to be mapped with XPM. The image shows the lamellar structures present in the microstructure on the antlers in dark and light regions.

The XPM maps, figure 4.19, of the lamellae show a difference in both hardness and modulus values. These are seen in the thicker bands that have an average modulus of 11.5 GPa and an average hardness 0.3 GPa. The thinner bands have an average hardness and modulus of 0.7 GPa and 18 GPa respectively. The histograms display a similar distribution between the hardness and modulus. This shows that the material properties of hardness and modulus are both dependent on the direction of the collagen fibres.

The presence of these bands displays the anisotropic nature of the lamellae in bone which is suspected to reduce crack propagation in the bone tissue (151). This anisotropic nature derives from the foundation of the structure of bone, that is the basic building block, the mineralised collagen fibril previous studies into the microhardness of the lamellae found that measurements taken from a direction perpendicular to the direction of the layers of the collagen molecules and the crystals the values are lower than measurements taken in the parallel direction (on the edge of the layers) (152).

Therefore, it can be determined the mapped regions of lower hardness and modulus values the collagen fibres and crystals are parallel to the surface of the sample and the areas of higher hardness and modulus values the collagen and crystals are running in perpendicular direction to the surface of the sample.

This information is able to account for the directionality of the collagen fibres only and is not able the reflect on the differences in the quantities of fibres present in the region being tested.
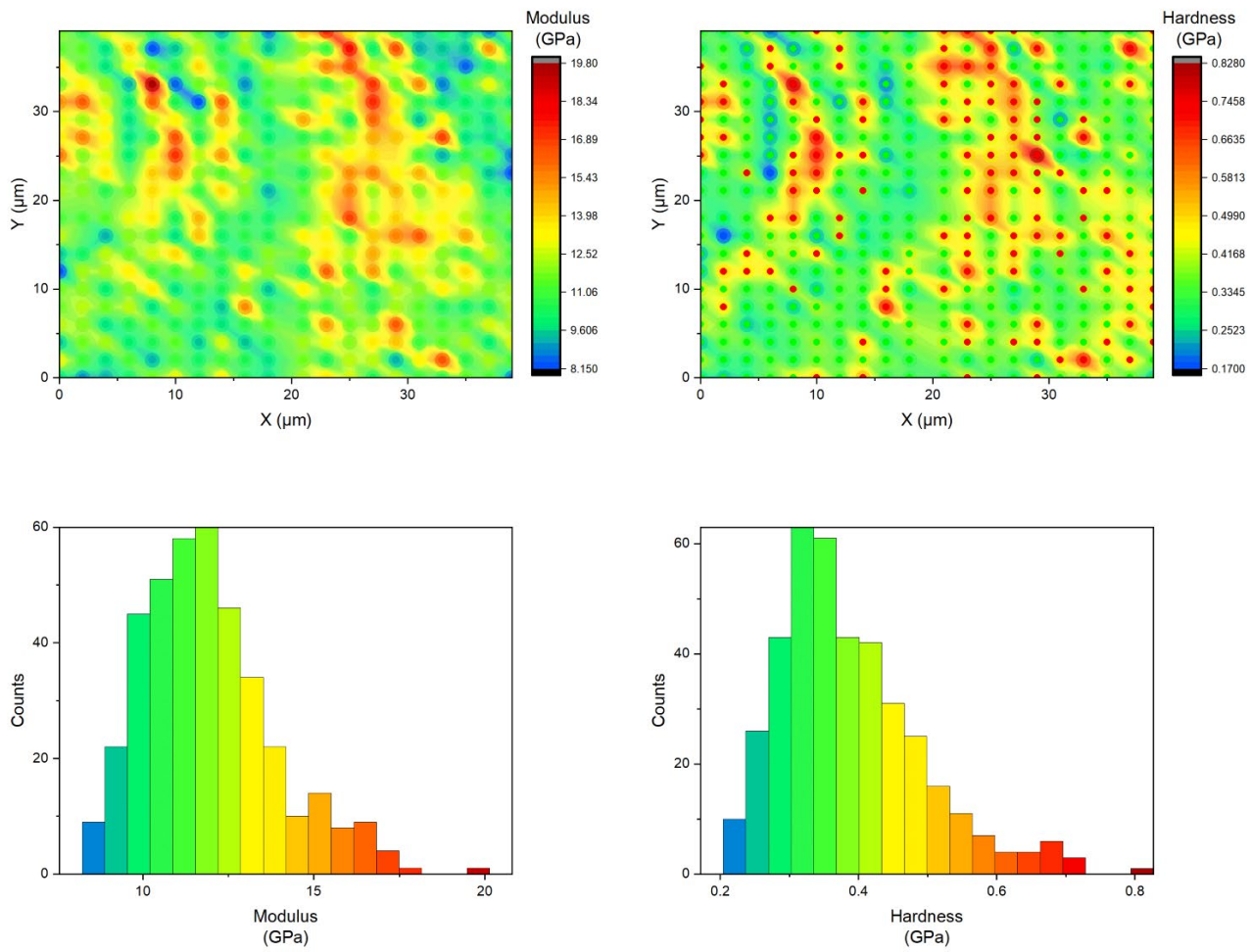
Figure 4.19. XPM maps and histograms of the transverse section modulus and hardness with histograms displaying the number of indents with the corresponding hardness values coordinated to the map.

The microstructural organisation in the transverse section is clearly visible in figure 4.23. In this section the lamellae appear to be spaced out more in an elongated manner and are much more clearly defined showing thinner, dark and thicker, light regions.
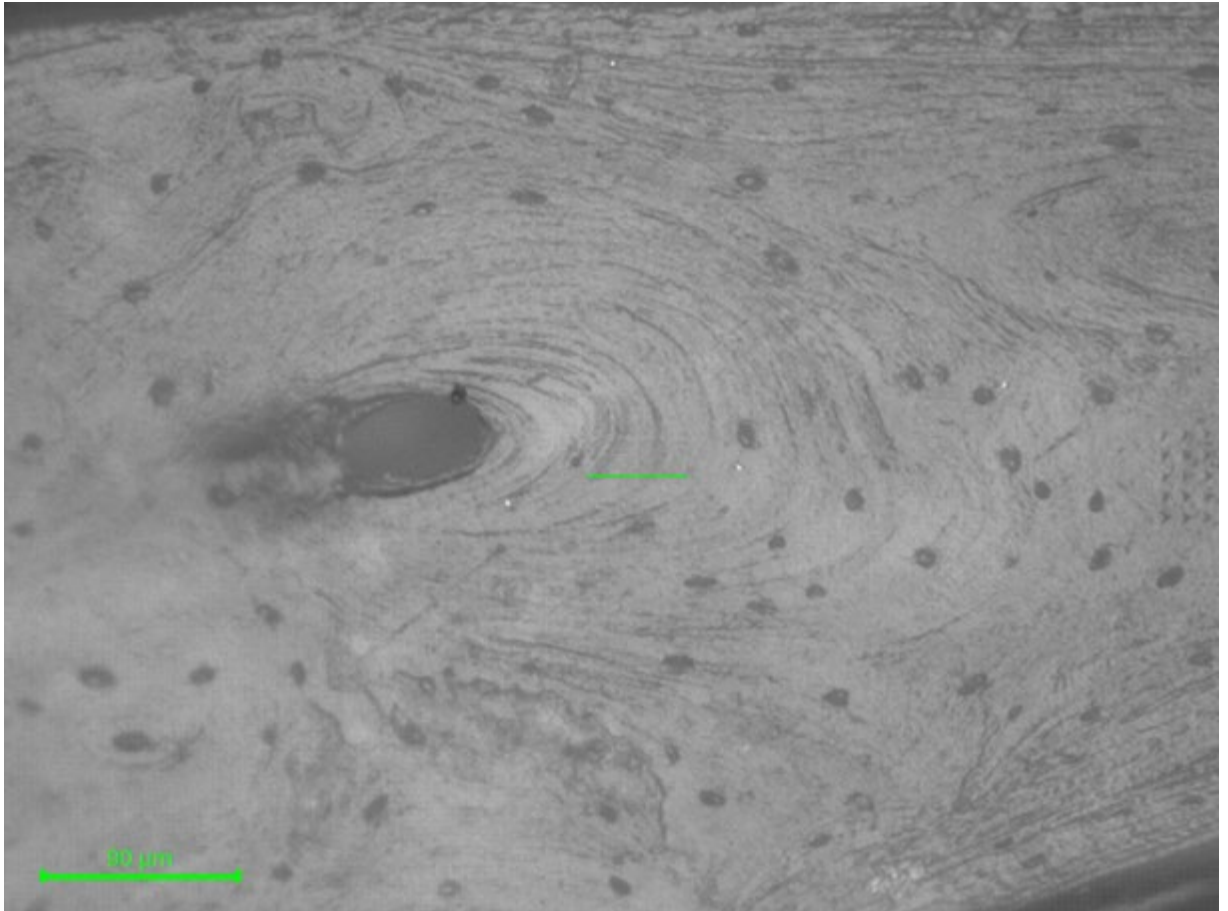

Figure 4.20. Image taken from the on-board optics of the Ti950 of the transverse antler section. The green line displays the bottom edge of the four chained XPM maps which are faintly visible.

4.2.5.2.2 Cross-section

It is observed from the SPM that the cross-sectional region selected for testing appeared to have a fracture highlighted in figure 4.20. It was decided that testing in this area would provide insight into the mechanical properties of the neighbouring bone tissue surrounding a fracture. This fracture was not observed in the optical image, figure 4.21 prior to selection of the area. This region was selected due to its clearly visible, uniformed lamellae structure around the haversian system. In this direction the lamellae appear closer and more tightly packed than the transverse section.
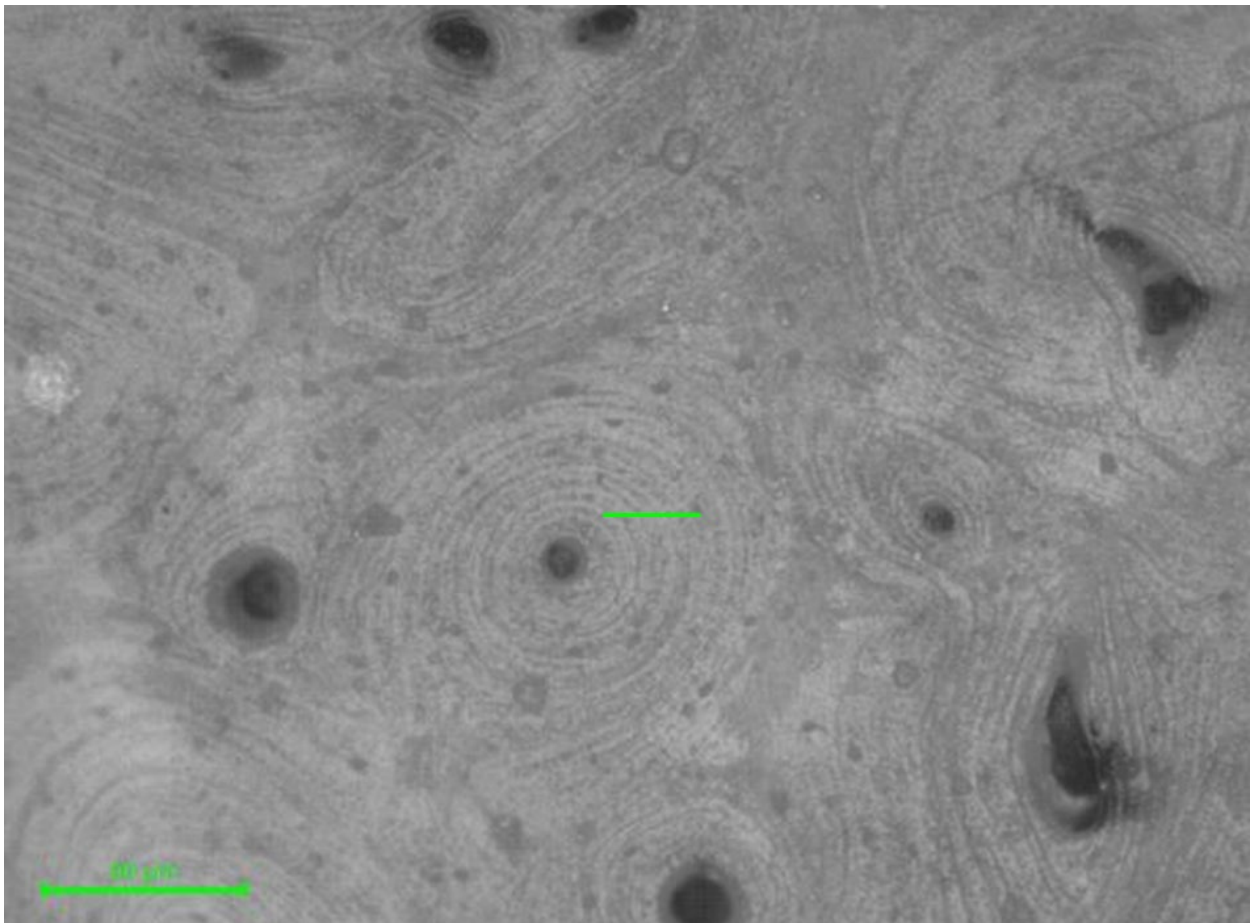

Figure 4.21. The location of the SPM and XPM region on the cross-sectional surface is highlighted by the green line the region shows uniformed and closely packed features.

Analysis with SEM would provide further detail into the properties of the fracture across the lamellae observed in the SPM image, figure 4.22. The SPM also shows the lamellae as very closely and uniformly packed with an approximate 10 μm width for the dark bands and 2.5 μm for the light bands.

50 μm

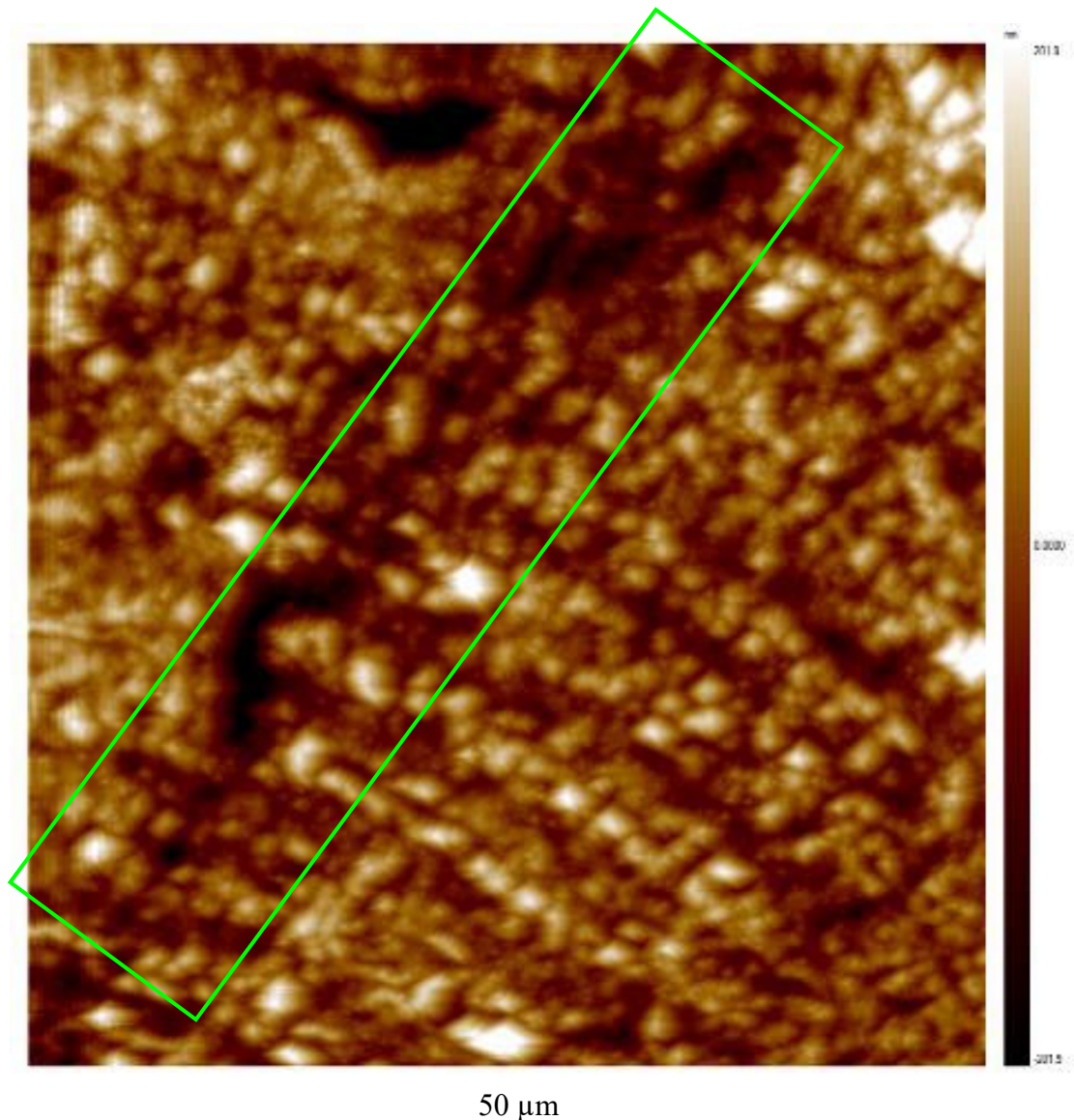**Figure 4.22.** SPM image of lamellar structure observed on the cross-sectional surface. The area covered is 50 μm x 50 μm. It is observed that in the cross-section of the sample the lamellae are more tightly packed than in the transverse region. The darker feature highlighted appears to be a fracture deflecting at the different lamellae which was not visible on optical investigation of the region.
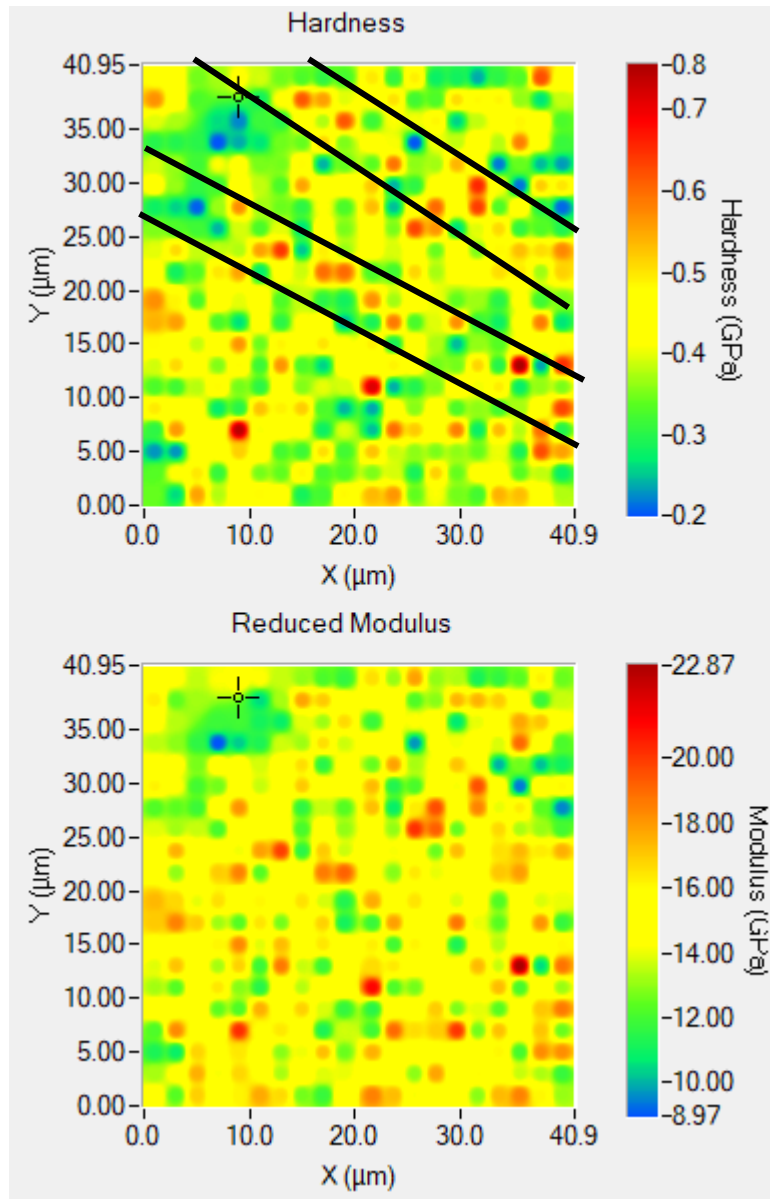
Figure 4.23. XPM maps showing modulus and hardness. The thin lamellar structures are drawn in by had to highlight the areas.

The XPM map in figure 4.23 very faintly displays a distinguishable difference in hardness between the lamellar. The bands are separated by the black lines. This may be due to the fact that the width of the lighter bands being almost the size of the spacing between the indents decided for the maps (2 μm). This means that the likelihood that the probe misses the lighter bands or lands on the edge of the features is increased. Therefore, the map will appear to have a more uniformed modulus and hardness and not show any statistically significant different between the lamellae as seen in the transverse section.

The thin lamellar structures appear to have a hardness of approximately 0.6 GPa and modulus of 17 GPa while the thicker bands appear to have an average hardness of 0.35 GPa and modulus of 15 GPa. Thus, it can be determined that as with the transverse section the collagen fibres and crystals perpendicular to the surface are the thinner bands due to the higher measurements. The thicker bands are the regions that the collagen fibres and the crystals are parallel to the surface of the sample this is determined from the comparatively lower measurements obtained.

There is no significant difference in the properties of the region around the sample with the apparent crack. The crack is shown on the map as the darker blue region on the top left. The properties of the antler directly surrounding the crack are the same as the properties a distance from the crack.

The cross section of another sample was analysed to confirm the lamellar structure in that direction. Figure 4.24 shows the on-board optical image with area tested highlighted by the green line. This also shows that in another sample that the lamellae are much more compact in a cross section.
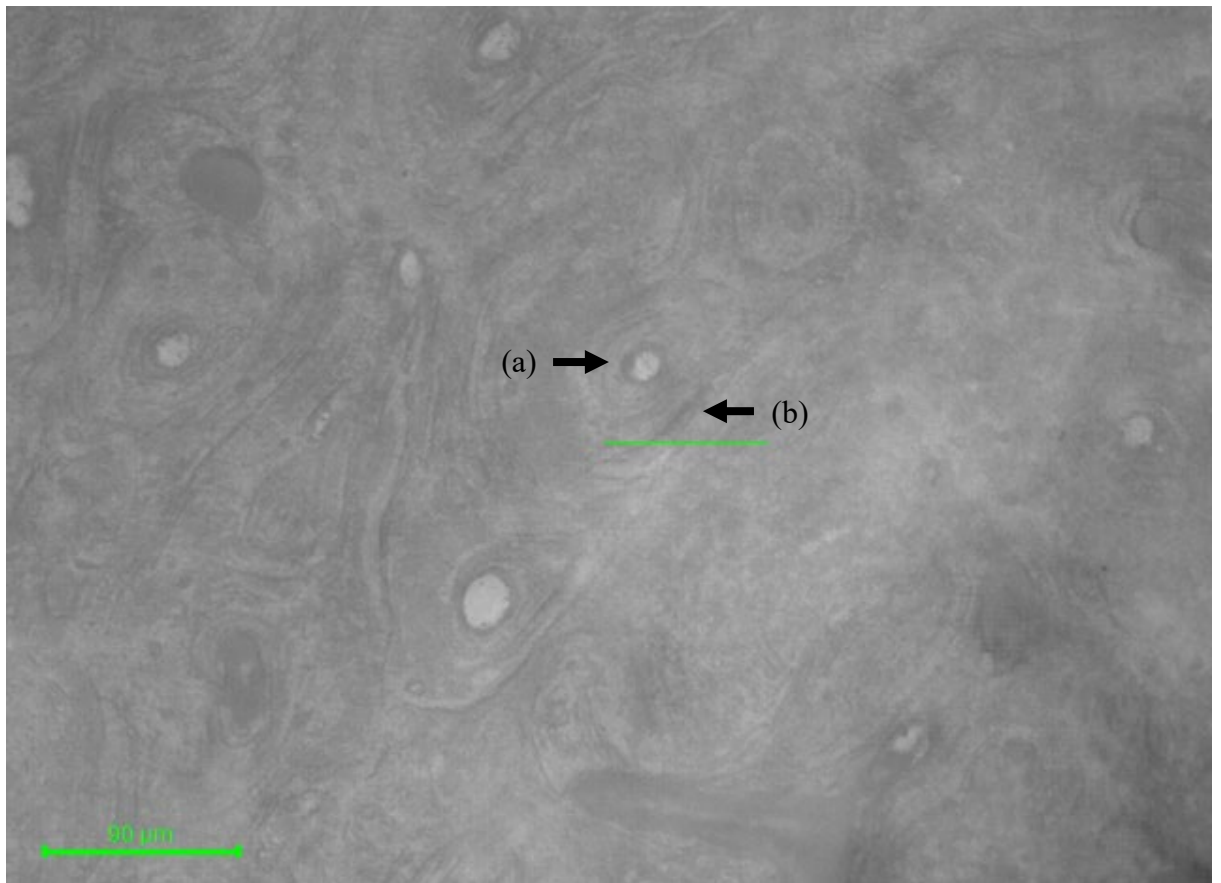

Figure 4.24. Image from onboard optics in the Ti 950 showing region mapped using XPM highlighted by the green line which would be located along the bottom of the stitched maps. The area shows a pore (a) surrounded by closely packed lamellae. Another larger band feature is included in the map (b) to distinguish the local mechanical properties of the band.

The maps of this region as seen in figure 4.28 show that the resolution selected is not sufficient to determine the difference in modulus of the lamellae in the cross-sectional direction, although differences in hardness were observed. However, the feature in figure 4.27 labelled as b is observed to have an average higher modulus and hardness than its immediately neighbouring regions.

This may be due to the feature b being a thicker region there the collagen fibres run perpendicular to the surface which will result in the higher measurements. The average hardness of these regions was 0.7 GPa with the regions of parallel collagen fibres displaying an average hardness of 0.3 GPa. In this map the pore structure, is clearly visible, the blue region on the top left of the map. On the hardness map it is particularly visible is that the lamellae immediately surrounding the pore runs perpendicular to the surface, that is in the same direction of the pore, which was (when the tissue was alive) the haversian canal. The haversian canal houses blood vessels that run through the tissue. These lamellae provided immediate protection to delicate blood vessels along the direction the haversian system would grow in the antler.
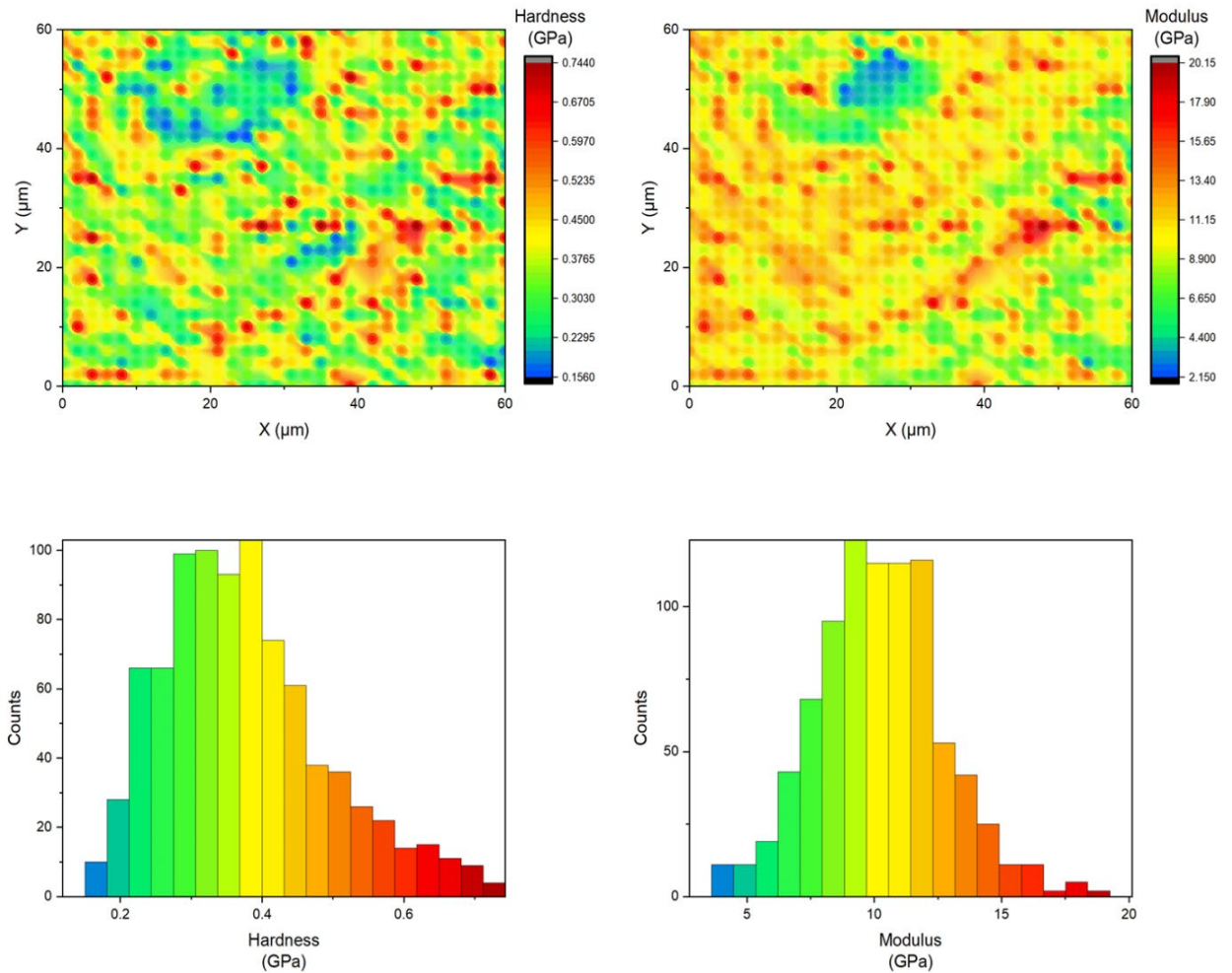
Figure 4.25. Section on another sample showing that the resolution is difficult to capture in the cross-sectional direction. However larger features observed with the on-board optics were clearly mapped.

The results obtained from traditional indentation performed on the same samples are very close to the values obtained from the XPM maps. The average hardness for the three categories in traditional indentation in the cross section is 0.4144 GPa and in XPM of the cross sections which show differences in the lamellae depending on the direction of the collagen fibres with a hardness of 0.6 GPa where the collagen is perpendicular to the surface and where the collagen is parallel to the surface in the maps, the hardness is 0.35 GPa. Close similarities were also observed for the modulus values and in the transvers section. The traditional indents were of a higher load resulting in larger indents than the XPM which may result in averaging of the property values. This shows that XPM is a valid technique for the analysis of variations in the lamellae of bone tissue.

5 Overall Conclusions

The organisation built from the nano- to macro-scale of mineralised biological tissues has been revolutionising the field of engineering, resulting in many bioinspired designs. The application of these naturally occurring materials into manufactured design first requires an in-depth understanding on multiple scales of how the morphology, structure, and properties give the material its functionality and the relationship between these features.

Correlative imaging of natural and biological materials can reveal the hidden mysteries that have evolved over millions of years, from which much can be learned to develop new materials. Biological materials display an elegant yet complex architecture from the nano- to macro scale- of individual smaller parts, that can be lightweight, and when combined display mechanical properties superior to their individual properties by orders of magnitude (101). Thus, it is important to assess the mechanical properties on the multiple scales of the material to enrich the existing knowledge of biological materials. Application of mechanical property testing in multiple situations such as in-situ mechanical property testing new avenues in understanding the behaviour of a material. Mapping of the properties, rapidly producing large amounts of statistical data, evaluating the individual localised regions with different mechanical, chemical or crystallographic properties interact.

This multi-scale understanding can be achieved by the application of a through workflow. The workflow must be a logical stepwise approach, considering important features of the samples. Biological materials provide a unique series challenges in characterisation that can be overcome by applying this workflow.

The order which these techniques are applied is important in a correlative characterisation workflow. A logical systematic approach as recommended by the workflow including nanomechanical property testing will enable a comprehensive understanding of the material.

5.2   Conclusion – Barnacle

The organisation of the microstructure of the barnacle alae shows specific crystallographic orientation in regions which are known growth fronts for the organism's exoskeleton. This growth region on the alae of the barnacles characterised from a horizontal section also shows a reduced modulus and hardness in this orientation.

The situation of the alae in the structure of the barnacle permits growth in a designated direction with the radii providing growth in the opposing direction. The equilibrium of the gradual growth of the barnacle exoskeleton possibly allows the organism to have consistent coverage to be protected from the external environment and predators.

Further testing is required on the tip of the barnacle ala, EBSD, and nanoindentation of the vertical axis can confirm how this specific orientation of calcite takes advantage of its known anisotropy in the interlocking regions of the plates.

Complementary testing in the radii of the plates, which according to previous literature also displays an elongated crystallographic orientation in different species, with EBDS and nanoindentation will highlight the importance of crystal orientation for these interlocks which are also growth fronts.

5.3 Conclusion - Antlers

Images from x-ray micro-CT are of particular importance to the study of bone materials, in understanding their behaviour under loading conditions via experimental finite element modelling of the CT data (153). When correlating the structure and properties of reindeer antlers to the function it must be noted that unlike internal skeletal bone which undergoes regular remodelling and is always in use, antlers do not bear load or are used until only after they have completed growth. Therefore, antlers must be grown appropriately for combat for success in mating for the male of the species, and survival in the winter for the female of the species.

There is no observed sacrifice in the nanomechanical response of antlers for females with calves compared to the female reindeers without calves and male reindeer in this study. This is supported by previous work on the testing of the bulk mechanical properties comparing male and female antlers. As far as the author is aware there are no previous studies into the differences in reindeer antlers with regards to the calving status of the female reindeer. This may be because antlers are key to survival in the winter for female reindeer as they use them to defend patches of food, for females that are expectant in the spring this is particularly important as the birthweight also affects the survivability of the calf, therefore appropriate diet is vital over the winter months, therefore, no sacrifices are made in the quality of antlers for the female of the species.

Future work for the analysis of the antlers would involve the testing of the mechanical properties of the trabeculae region of the antlers. Due to the differences observed between the FWC and the M categories in X-ray micro-CT, the FWC sample having a larger trabeculae region than the M samples, there may be differences in their mechanical properties. Possibly to hale the FWC category to cope with a smaller trabeculae region.

Appendix A

IntraSpect 360 in Situ Nanoindentation in the Versa Xradia 520

1.2   Installation of IntraSpect 360

1. Remove any sample mounts that are currently in place so that just the standard, fixed base is left.
2. Place the base plate so that the 3 large holes align with the three large holes in the Versa's standard base. Using the large screws and corresponding Allen Key (Provided in the kit) secure the IntraSpect 360's base plate into the Versa.
    - The base plate has a small guide spike protruding from the centre. This must remain straight.
3. Once the sample is roughly aligned (See alignment section) place the rest of the IntraSpect 360 onto the base plate making sure that the guide spike is aligned with the guide hole, and the Intraspect is lowered carefully to avoid any bending of the spike.
4. Once securely on the base plate, align the 3 small thumbscrew holes with the smaller holes on the base plate. Screw in the thumbscrews until finger tight.
    - When aligning the screws match up the marker on the base to the marker on the IntraSpect.
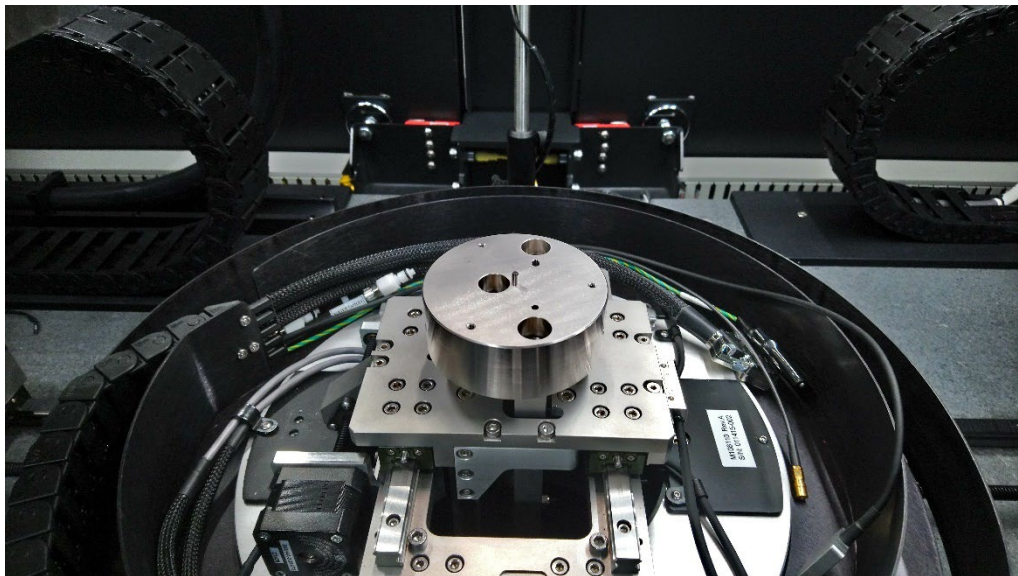
Figure 1: IntraSpect 360 base plate installed, displaying the location of three base screws and the guide spike

Dial to raise and lower
sample in cell

X-Ray transparent viewing
window, Samples are
placed on the top)

Edge of housing (Lifts up
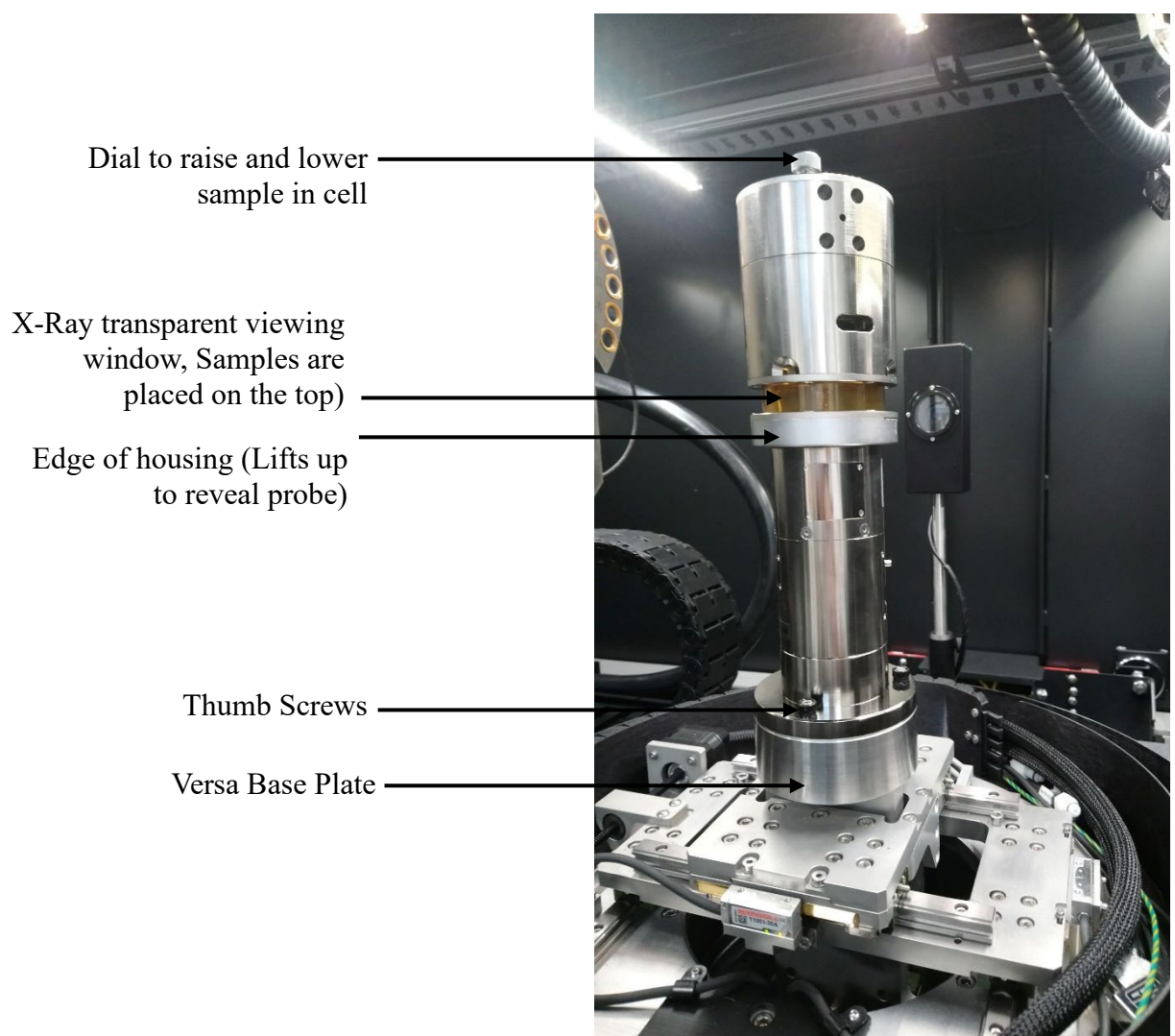to reveal probe)

Thumb Screws

Versa Base Plate

Figure 2: IntraSpect 360 fully installed into the Versa Xradia 520 showing key components of
the in-situ rig

1.3 Mounting and aligning the sample

1. The sample must be mounted on one of the stubs and screwed into the top of the housing.
    - Care must be taken to ensure that the sample is retracted far enough from the indenter tip when replacing the housing with the sample installed.
2. Alignment is done using the screws on the housing (See figure 3) and the hex key provided (located inside the Versa). They move the sample in two axes, in a direction perpendicular to the face of the screw.
3. Depending on the shape of the sample it is best to align it so that:
    - the indenter is towards the centre of the sample if it has a regular shape.
    - the indenter is over the required area of interest
    - If the sample is irregularly shaped align the specimen along one axis before attempting to align along the other axis.
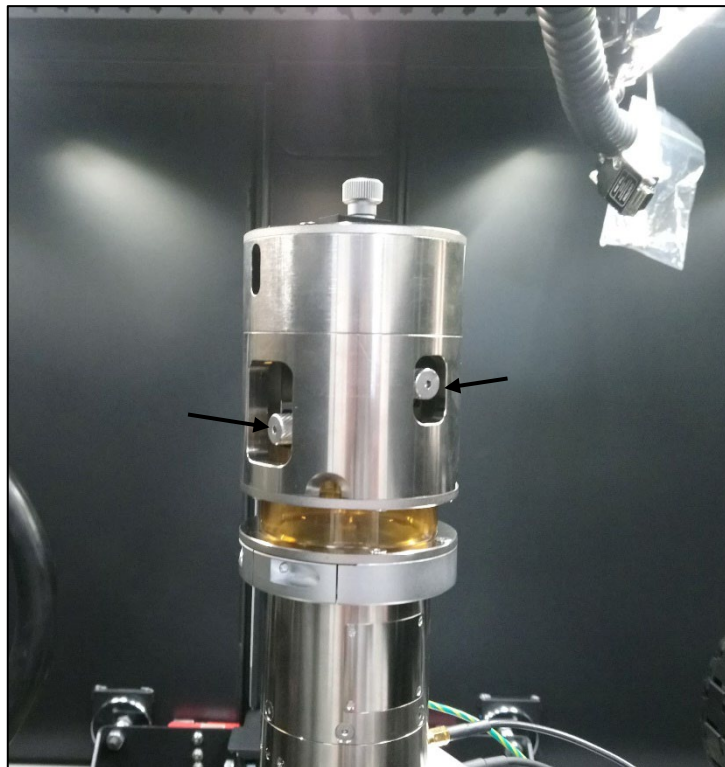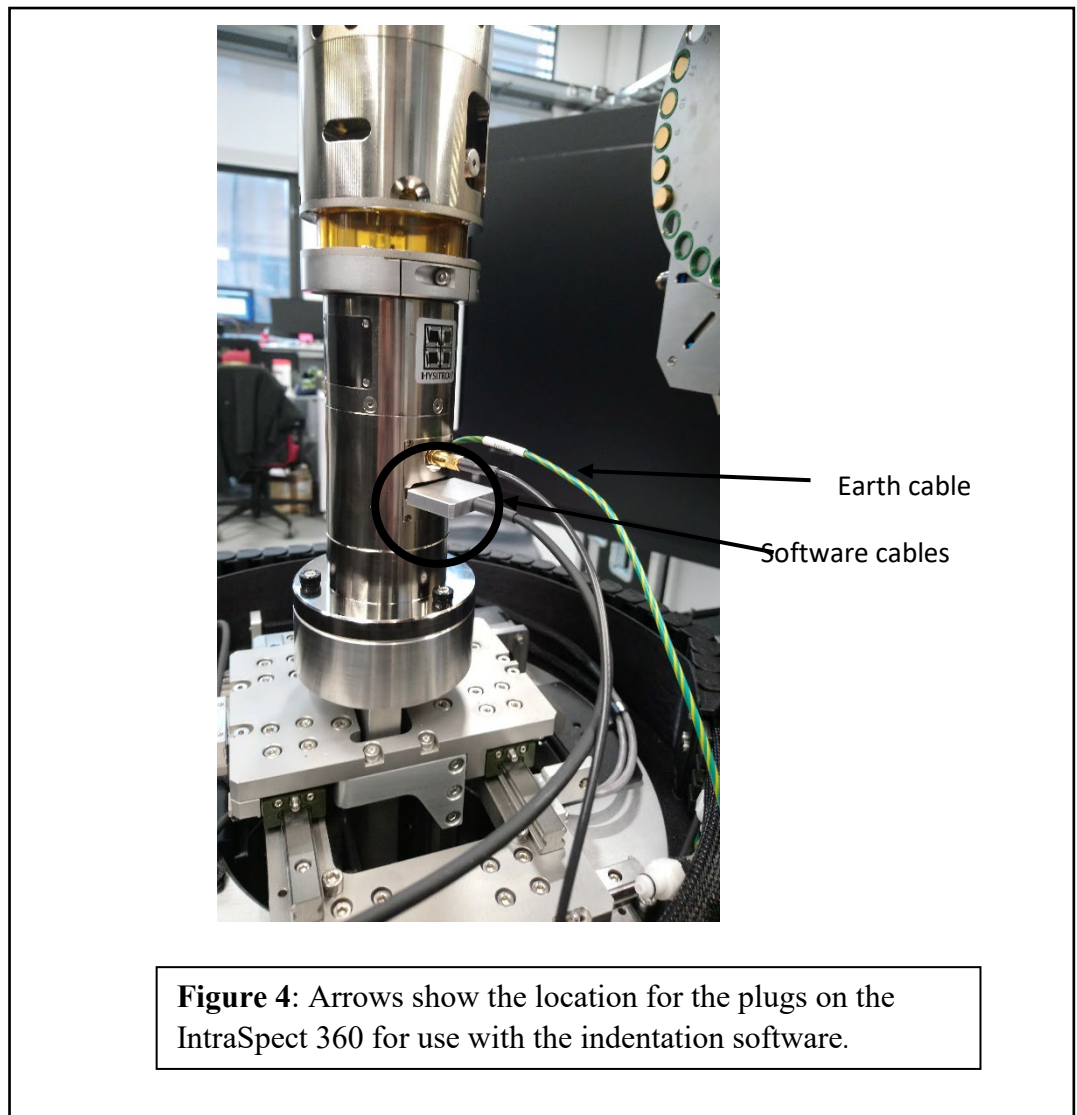

Figure 3: Arrows show the alignment dials on the housing of the IntraSpect 360.

NB: When setting up the scan, the background reference image should be done by removing the rig. And collecting the images at 0˚ and 90˚.

1.4 Starting the Software

1. After the reference image has been collected replace the rig into the Versa as before.
2. Plug the software cables into their designated spaces. (The cables are permanently located in the versa on the inside of the carousel)
3. Earth the IntraSpect 360 by clamping the earthing cable onto one of the base thumb screws, and checking to ensure that it is secure.

Earth cable

Software cables

Figure 4: Arrows show the location for the plugs on the IntraSpect 360 for use with the indentation software.

4. Switch on the unit shown in figure 5 after the IntraSpect has been fully installed within the Versa.

Figure 5: Hysitron Performech advanced control module connected to the in-situ device.
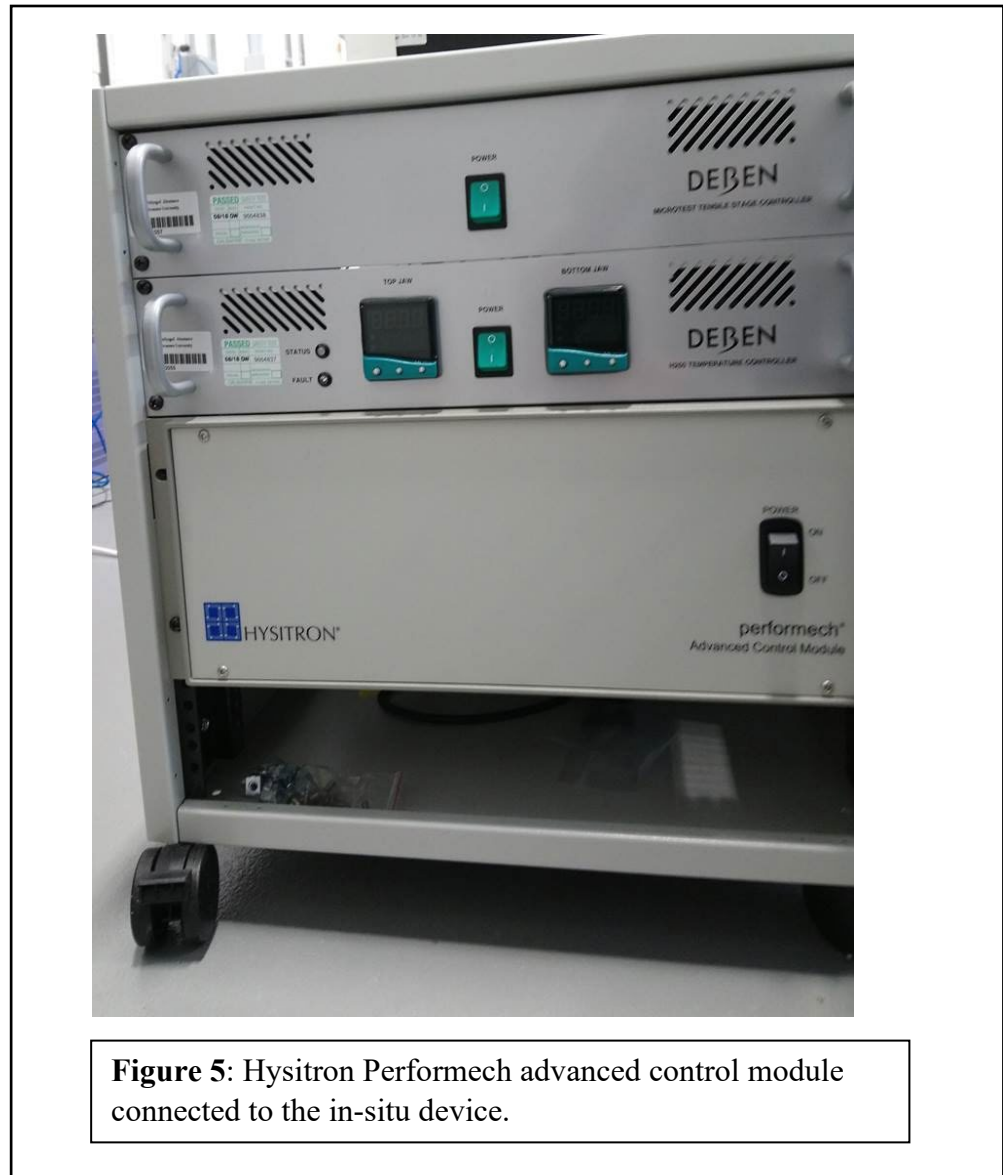
5. Once the unit is on turn on the laptop that is designated for use with the IntraSpect 360.

6. Open the Triboscan software from the desktop.

7. Run Calibration for high load, once pleased with the calibration results save them

8. Head to Load Function and open a saved Trapezium.

9. Set to the desired load, check that the hold time for the run is approximately 54,030 seconds approx. 15hrs. The scan will take between 14hr 10mins to 14hrs 20 mins. There is approximately a 20-30 min window after starting the scan to make fine adjustments to the alignment.

NB: There must be 2 scans at 0N load if carrying out DVC. When a load is applied the indenter will move to be in contact with the sample and minor adjustments will need to be made.

Appendix B

Selection of ideal spacing of indents for XPM

A series of XPM tests were performed on a fused quartz standard provided by Bruker Hysitron with a Berkovich tip geometry to visualise the impact of overlapping indents in XPM on the final results. Figure 1 shows an SPM of a region on a fused quarts standard sample that an XPM test was performed to display what is observed when indents are placed too close together and how they interact. The load set was 13476 µN to create large enough loads in the sample to be easily observed. The map was created over a 10 µm x 10 µm area with 100 indents. As the sample being tested is a manufacturer supplied standard the hardness and modulus values with a Berkovich tip were also provided by Bruker Hysitron, the hardness is 9.25 GPa and reduced modulus is 72.0 GPa.
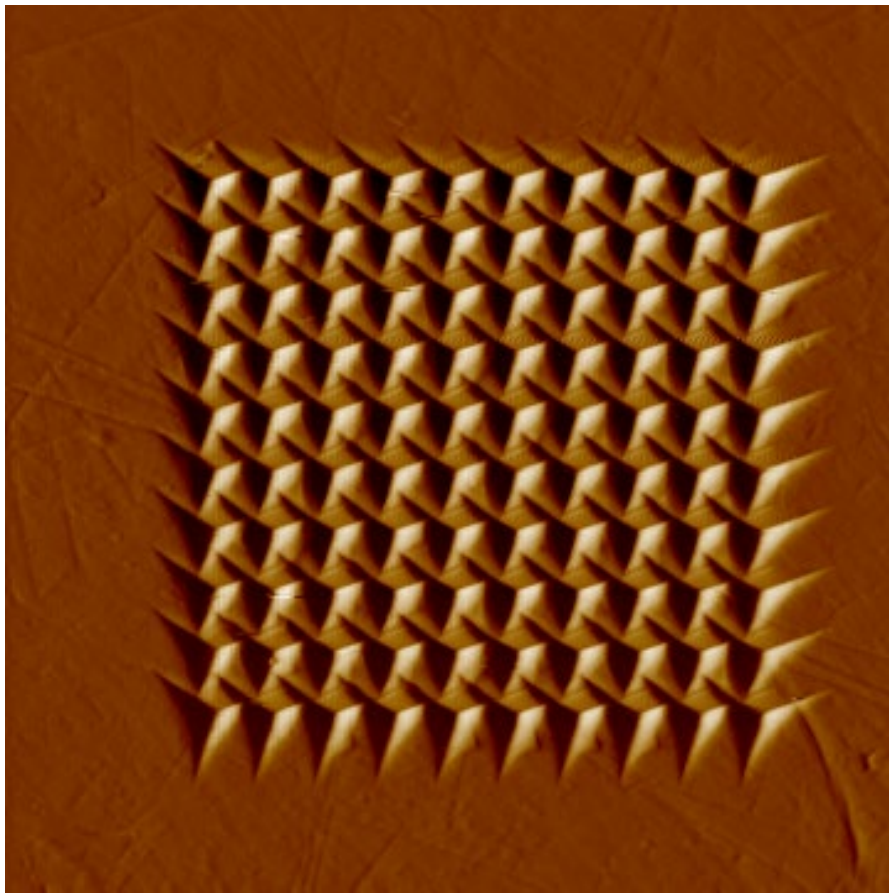

Figure 1. SPM of a 10 µm x 10 µm XPM map on fused quartz with a 1 µm spacing and a load of 13476 µN.

In figure 1 overlapping indents are clearly visible and not all the features of each indent can be observed on the sample showing that as the indents were performed within the residual indent. The following indents were therefore not performed on a smooth surface as necessary. As discussed previously the smoothness of a sample surface will have an impact on the data obtained.

Another map was performed with the same load and number if indents however the spacing was set to 2 μ with the map then covering a 20 μm x 20 μm area. The proximity of the indents as seen in figure 2 shows larger spacing with only a small degree of overlapping. From figure 3 most of the indents fall within a close hardness range 9.8 GPa to 10.5 GPa with four out of one hundred indents out of this range. Similarly, for the reduced modulus most indents fell within the range of 70 GPa and 72.5 GPa with five of the one hundred indents outside of the range. In this map, a significant outlier was observed, comparing the location of the outlier on the map with the SPM this anomaly was found to be due to the scratch that is at the centre of the indent.
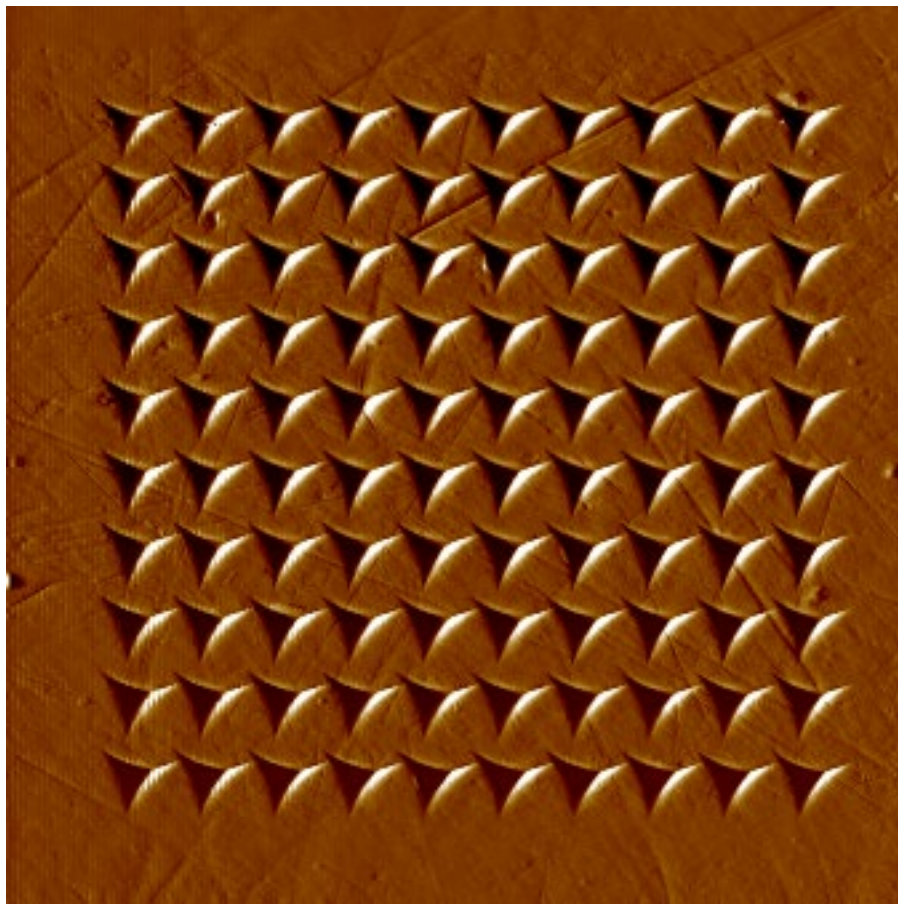

Figure 2. SPM of a 20 μm x 20 μm XPM map on fused quartz with a 2 μm spacing and a load of 13476 μN.

Figure 3. Image of TriboScan software showing the P/h graph, hardness and modulus maps and their corresponding histograms of the 20 µm x 20 µm XPM map on fused quartz.

In figure 3 a single indent was found to be harder and have a higher modulus than the surrounding region. This is explained when correlating the map with the SPM where it can be seen that a scratch is going through the indented area. The impact of the scratch on the surface of the material gives a higher value for both hardness and modulus. This reinforces the necessity of having smooth finish, with no scratches for testing.

A further map was done on another area of the fused quartz a 30 µm x 30 µm of 100 indents were performed with the same load as the previous maps. From the SPM in figure 4 there was no interaction between the indents. All one hundred indents fell within the range of 9.7 GPa to 10.6 GPa likewise for reduced modulus all one hundred indents were within the range of 70.1 GPa to 73.6 GPa as observed in the analysis in figure 5.

Figure 4. SPM of a 30 µm x 30 µm XPM map on fused quartz with a 3 µm spacing and a load of 13476 µN. Although the indents are close there is no interaction between them.
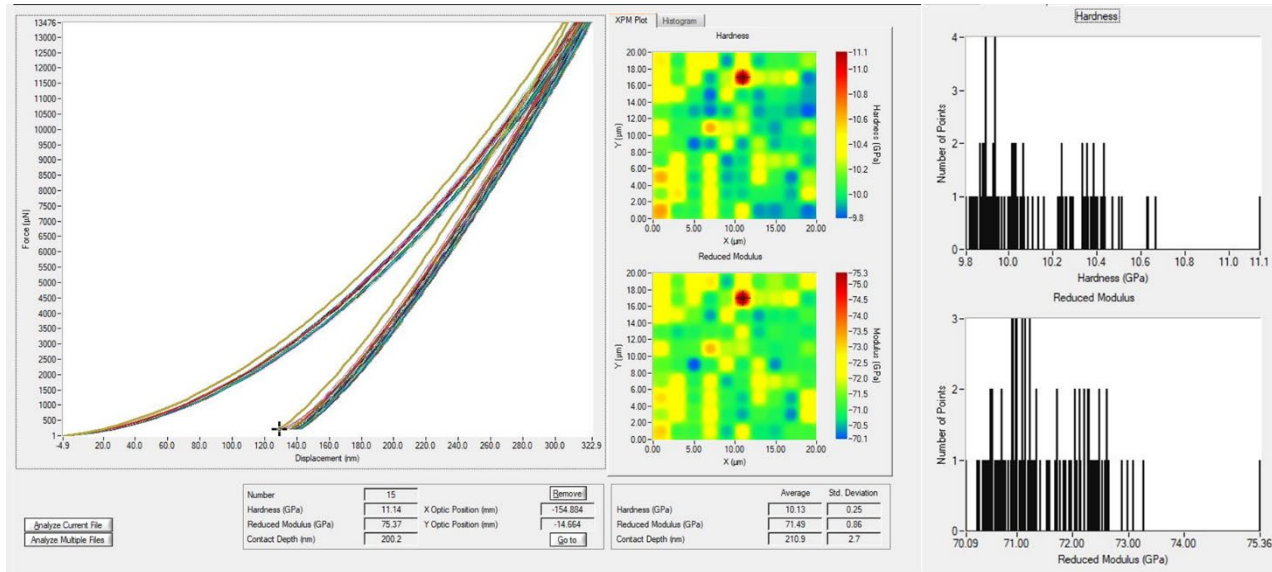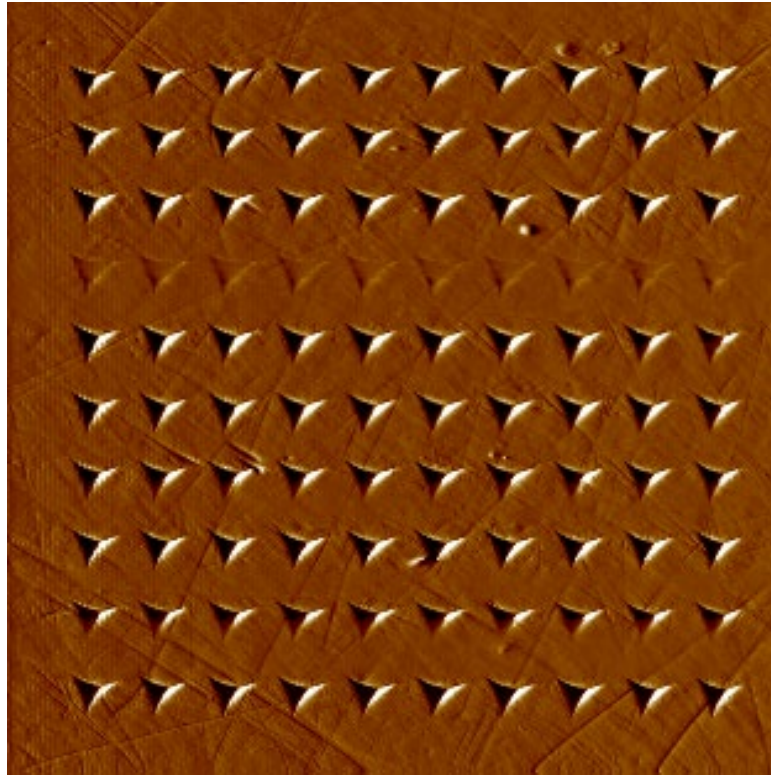

Figure 5. Image of TriboScan software showing the P/h graph, hardness and modulus maps and their corresponding histograms of the 30 µm x 30 µm XPM map on fused quartz.

A 40 μm x 40 μm XPM map was performed consisting of 100 indents of the same load with a 4 μm spacing between indents. Figure 6 shows the SPM image of the map there is no interaction between the indents and there is sufficient spacing between indents to prevent this, however, this spacing may miss microstructural features on a surface as the resolution of the map will be lower. Figure 7 shows that as with the map that had a 3 μm spacing all one hundred hardness and reduced modulus values were found to fall within a small range, reflecting the uniformity and smoothness of the sample tested. The Hardness value range from all the indents was between 9.7 GPa and 10.5 GP and reduced modulus was 70.4 GPa to 73.5 GPa. Further proving that there was no interaction between indents.

Figure 6. SPM of a 40 μm x 40 μm XPM map on fused quartz with a 4 μm spacing and a load of 13476 μN. As the SPM is of a larger area the indents will appear smaller as though zoomed out.
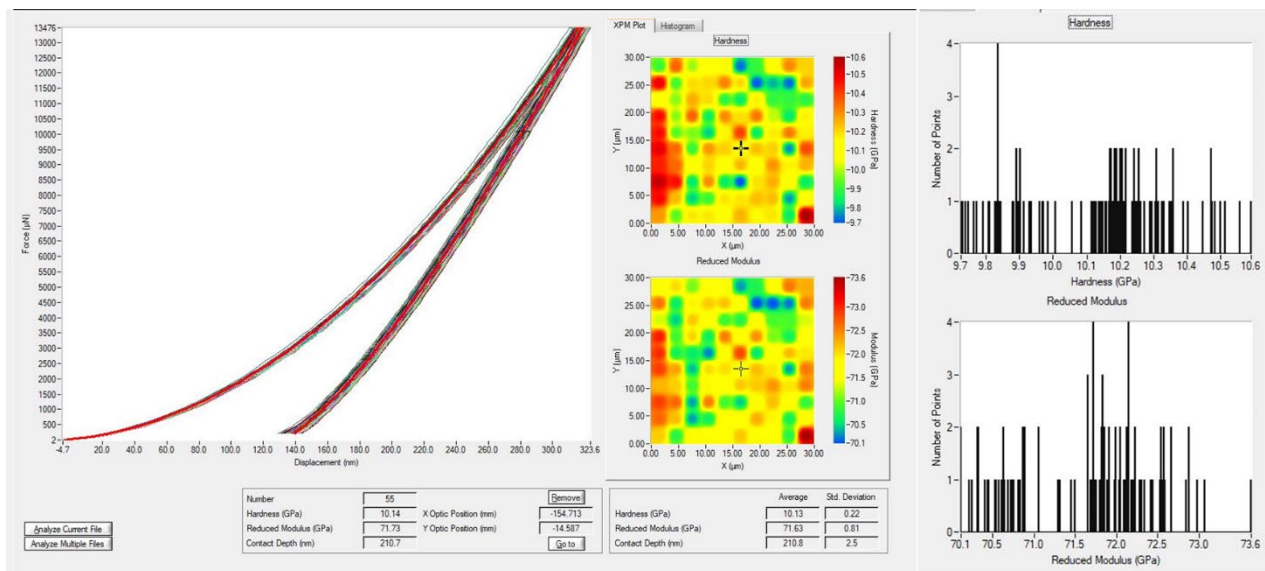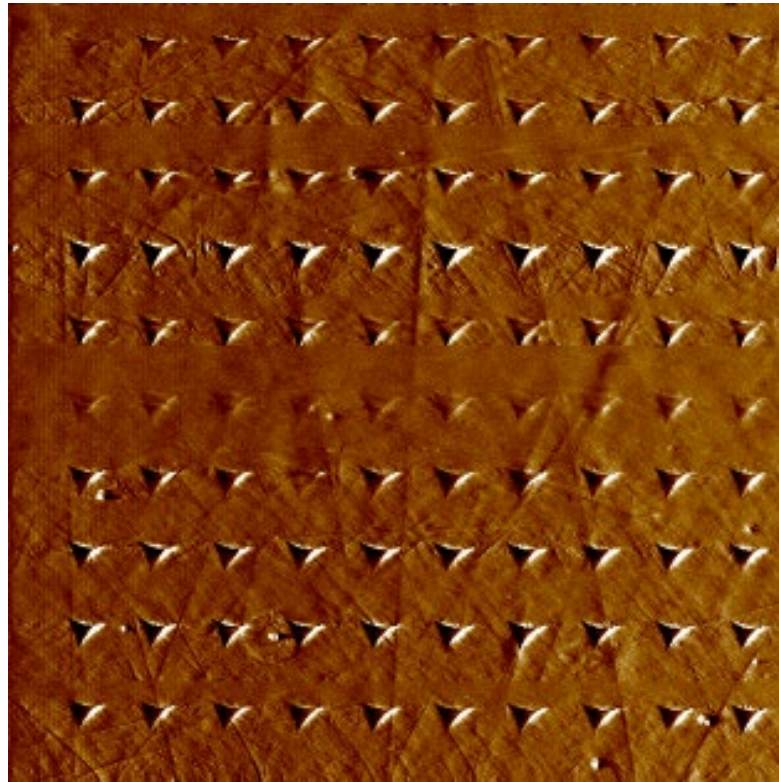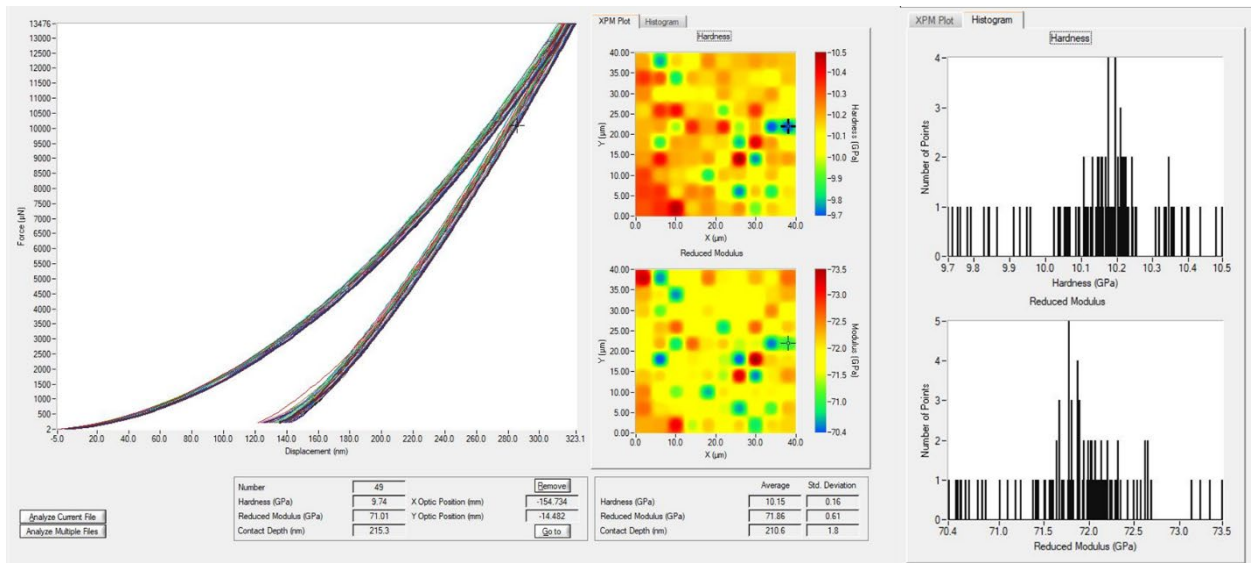
Figure 7. Image of TriboScan software showing the P/h graph, hardness and modulus maps and their corresponding histograms of the 40 μm x 40 μm XPM map on fused quartz.

References

1. Dykas M. Novel approach to correlative imaging. 2017.

2. Su Y, Nykanen M, Jahn KA, Whan R, Cantrill L, Soon LL, et al. Multi-dimensional correlative imaging of subcellular events: combining the strengths of light and electron microscopy. Biophys Rev. 2010 Jul 28;2(3):121–35.

3. Mitchell RL, Coleman M, Davies P, North L, Pope EC, Pleydell-Pearce C, et al. Macro-to-nanoscale investigation of wall-plate joints in the acorn barnacle Semibalanus balanoides: correlative imaging, biological form and function, and bioinspiration. Journal of The Royal Society Interface. 2019 Aug 30;16(157):20190218.

4. Wang Y, Friedrich H, Voets IK, Zijlstra P, Albertazzi L. Correlative imaging for polymer science. Journal of Polymer Science. 2021;59(12):1232–40.

5. Gaponenko I, Cherifi-Hertel S, Acevedo-Salas U, Bassiri-Gharb N, Paruch P. Correlative imaging of ferroelectric domain walls. Sci Rep. 2022 Jan 7;12(1):165.

6. Godec M, Zaefferer S, Podgornik B, Šinko M, Tchernychova E. Quantitative multiscale correlative microstructure analysis of additive manufacturing of stainless steel 316L processed by selective laser melting. Materials Characterization. 2020 Feb 1;160:110074.

7. Chang Y, Lin M, Hangen U, Richter S, Haase C, Bleck W. Revealing the relation between microstructural heterogeneities and local mechanical properties of complex-phase steel by correlative electron microscopy and nanoindentation characterization. Materials & Design. 2021 May 1;203:109620.

8. Stika KM, Westphal CS, Kapur J, Raty RG, Li J, Kopchick JG, et al. Mapping chemical and mechanical property degradation in photovoltaic modules. In: 2014 IEEE 40th Photovoltaic Specialist Conference (PVSC). 2014. p. 2647–50.

9. Whitesides GM. Bioinspiration: something for everyone. Interface Focus. 2015 Aug 6;5(4):20150031.

10. Wang Y, Naleway SE, Wang B. Biological and bioinspired materials: Structure leading to functional and mechanical performance. Bioactive Materials. 2020 Dec 1;5(4):745–57.

11. Blob RW, Labarbera M. Correlates of variation in deer antler stiffness: age, mineral content, intra-antler location, habitat, and phylogeny. Biological Journal of the Linnean Society. 2001 Sep 1;74(1):113–20.

12. Landete-Castillejos T, García A, Pérez M, Ceacero F, Cappelli J, Gambin P, et al. Analysis of antler composition and mechanical properties reveal key micro-minerals for deer. In 2016.

13. Pathak NN, Pattanaik AK, Patra RC, Arora BM. Mineral composition of antlers of three deer species reared in captivity. Small Ruminant Research. 2001 Oct 1;42(1):61–5.

14. Handschuh S, Baeumler N, Schwaha T, Ruthensteiner B. A correlative approach for combining microCT, light and transmission electron microscopy in a single 3D scenario. Frontiers in Zoology. 2013 Aug 3;10(1):44.

15. Paul-Gilloteaux P, Heiligenstein X, Belle M, Domart MC, Larijani B, Collinson L, et al. eC-CLEM: flexible multidimensional registration software for correlative microscopies. Nat Methods. 2017 Feb;14(2):102–3.

16. Burnett TL, Withers PJ. Completing the picture through correlative characterization. Nat Mater. 2019 Oct;18(10):1041–9.

17. Arif M, Mahmoud M, Zhang Y, Iglauer S. X-ray tomography imaging of shale microstructures: A review in the context of multiscale correlative imaging. International Journal of Coal Geology. 2021 Jan 1;233:103641.

18. Daly M, Burnett TL, Pickering EJ, Tuck OCG, Léonard F, Kelley R, et al. A multi-scale correlative investigation of ductile fracture. Acta Materialia. 2017 May 15;130:56–68.

19. Johnston RE, Mitchell RL, Pleydell-Pearce C, Coleman M, North L, LaBonte D, et al. Correlating Microstructure to in situ Micromechanical Behaviour and Toughening Strategies in Biological Materials. Microscopy and Microanalysis. 2019 Aug;25(S2):372–3.

20. Meyers MA, Chen PY, Lin AYM, Seki Y. Biological materials: Structure and mechanical properties. Progress in Materials Science. 2008 Jan 1;53(1):1–206.

21. Clarke A, Eberhardt C, Eberhardt CN. Microscopy Techniques for Materials Science. Woodhead Publishing; 2002. 464 p.

22. Measurlabs. Optical microscopy | Measurlabs [Internet]. [cited 2022 Sep 19]. Available from: https://measurlabs.com/methods/[object Object]/

23. ZEISS Microscopy Online Campus | Microscopy Basics | Reflected Light Microscopy [Internet]. [cited 2022 Sep 19]. Available from: https://zeiss-campus.magnet.fsu.edu/articles/basics/reflected.html

24. Allegretta I, Legrand S, Alfeld M, Gattullo CE, Porfido C, Spagnuolo M, et al. SEM-EDX hyperspectral data analysis for the study of soil aggregates. Geoderma. 2022 Jan 15;406:115540.

25. Pretorius E. Traditional coating techniques in scanning electron microscopy compared to uncoated charge compensator technology: Looking at human blood fibrin networks with the ZEISS ULTRA Plus FEG-SEM. Microscopy Research and Technique. 2011;74(4):343–6.

26. A EM, A DJP, A DM, A MAP, Seatonb N, A DT, et al. Electron backscatter diffraction (EBSD) in the SEM: applications to microstructures in minerals and rocks and recent technological advancements.

27. EBSD Oxford Instruments - Introduction [Internet]. [cited 2018 Apr 14]. Available from: http://www.ebsd.com/introduction

28. Mayo SC, Stevenson AW, Wilkins SW. In-Line Phase-Contrast X-ray Imaging and Tomography for Materials Science. Materials. 2012 May;5(5):937–65.

29. du Plessis A, Broeckhoven C, Guelpa A, le Roux SG. Laboratory x-ray micro-computed tomography: a user guideline for biological samples. GigaScience. 2017 Jun 1;6(6):gix027.

30. Hsieh J. Computed Tomography: Principles, Design, Artifacts, and Recent Advances. SPIE Press; 2003. 406 p.

31. Metscher BD. MicroCT for comparative morphology: simple staining methods allow high-contrast 3D imaging of diverse non-mineralized animal tissues. BMC Physiology. 2009 Jun 22;9(1):11.

32. Kalender WA. Computed Tomography: Fundamentals, System Technology, Image Quality, Applications. John Wiley & Sons; 2011. 374 p.

33. Neues F, Epple M. X-ray Microcomputer Tomography for the Study of Biomineralized Endo- and Exoskeletons of Animals. Chem Rev. 2008 Nov 12;108(11):4734–41.

34. Poole KES, Chappell DDG, Clark E, Fleming J, Shepstone L, Turmezei TD, et al. PHOENIX (Picking up Hidden Osteoporosis Effectively during Normal CT Imaging without additional X-rays): protocol for a randomised, multicentre feasibility study. BMJ Open. 2022 May 1;12(5):e050343.

35. Amini M, Reisinger A, Pahr DH. Influence of processing parameters on mechanical properties of a 3D-printed trabecular bone microstructure. Journal of Biomedical Materials Research Part B: Applied Biomaterials. 2020;108(1):38–47.

36. Picavet P, Balligand M. Organic and mechanical properties of Cervidae antlers: a review. Veterinary Research Communications. 2016 Dec 1;40.

37. Kierdorf U, Flohr S, Gomez S, Landete-Castillejos T, Kierdorf H. The structure of pedicle and hard antler bone in the European roe deer (Capreolus capreolus): a light microscope and backscattered electron imaging study. J Anat. 2013 Oct;223(4):364–84.

38. Wang Z, Zhang Y, Jiang S, Wang J, Du D, Wang X, et al. The red deer antler: Bioinspired design of an Al-Si composite with a fenestrated network-particle structure. 2020 Apr 1;6:545–56.

39. Creveling PJ, Fisher J, LeBaron N, Czabaj MW. 4D Imaging of ceramic matrix composites during polymer infiltration and pyrolysis. Acta Materialia. 2020 Dec 1;201:547–60.

40. Pathak N, Butcher C, Worswick MJ, Bellhouse E, Gao J. Damage Evolution in Complex-Phase and Dual-Phase Steels during Edge Stretching. Materials (Basel). 2017 Mar 27;10(4):346.

41. Cahalane RM, Barrett HE, O'Brien JM, Kavanagh EG, Moloney MA, Walsh MT. Relating the mechanical properties of atherosclerotic calcification to radiographic density: A nanoindentation approach. Acta Biomaterialia. 2018 Oct 15;80:228–36.

42. Garcea SC, Wang Y, Withers PJ. X-ray computed tomography of polymer composites. Composites Science and Technology. 2018 Mar 1;156:305–19.

43. Withers PJ, Preuss M. Fatigue and Damage in Structural Materials Studied by X-Ray Tomography. Annual Review of Materials Research. 2012;42(1):81–103.

44. Robinson JB, Darr JA, Eastwood DS, Hinds G, Lee PD, Shearing PR, et al. Non-uniform temperature distribution in Li-ion batteries during discharge – A combined thermal imaging, X-ray micro-tomography and electrochemical impedance approach. Journal of Power Sources. 2014;252:51–7.

45. Bay BK, Smith TS, Fyhrie DP, Saad M. Digital volume correlation: Three-dimensional strain mapping using X-ray tomography. Experimental Mechanics. 1999 Sep 1;39(3):217–26.

46. Franck C, Hong S, Maskarinec S, Phd D, Ravichandran G. Three-dimensional Full-field Measurements of Large Deformations in Soft Materials Using Confocal Microscopy and Digital Volume Correlation. Experimental Mechanics. 2007 May 8;47:427–38.

47. Eastwood DS, Yufit V, Gelb J, Gu A, Bradley RS, Harris SJ, et al. Lithiation-Induced Dilation Mapping in a Lithium-Ion Battery Electrode by 3D X-Ray Microscopy and Digital Volume Correlation. Advanced Energy Materials. 2014;4(4):1300506.

48. Juri AZ, Basak AK, Yin L. Microstructural responses of Zirconia materials to in-situ SEM nanoindentation. Journal of the Mechanical Behavior of Biomedical Materials. 2021 Jun 1;118:104450.

49. Lowe T, Avcu E, Bousser E, Sellers W, Withers PJ. 3D Imaging of Indentation Damage in Bone. Materials (Basel). 2018 Dec 13;11(12):2533.

50. Fratzl P, Gupta HS, Fischer FD, Kolednik O. Hindered Crack Propagation in Materials with Periodically Varying Young's Modulus—Lessons from Biological Materials. Advanced Materials. 2007;19(18):2657–61.

51. North L, Labonte D, Oyen ML, Coleman MP, Caliskan HB, Johnston RE. Interrelated chemical-microstructural-nanomechanical variations in the structural units of the cuttlebone of Sepia officinalis. APL Materials. 2017 Nov;5(11):116103.

52. Jahan A, Ismail MY, Sapuan SM, Mustapha F. Material screening and choosing methods – A review. Materials & Design. 2010 Feb 1;31(2):696–705.

53. Kutz M. Handbook of Materials Selection. John Wiley & Sons; 2002. 1528 p.

54. Ravansari R, Wilson SC, Tighe M. Portable X-ray fluorescence for environmental assessment of soils: Not just a point and shoot method. Environment International. 2020 Jan 1;134:105250.

55. Olise FS, Owoade OK, Adekola SA, Olaniyi HB, Mtshali CB, Przybylowicz WJ, et al. A Combination of µ-PIXE, XRF, SEM-EDS and XRD Techniques in the Analyses of Sn-Mine Tailings. J Rad Nucl Appl. 2017 Sep 1;2(3):95–102.

56. Padoan R, Steemers A, Klein M, Aalderink B, de Bruin G. QUANTITATIVE HYPERSPECTRAL IMAGING OF HISTORICAL DOCUMENTS: TECHNIQUE AND APPLICATIONS. 2008 Jan 1;

57. Pereira MO, Felix VS, Oliveira AL, Ferreira DS, Pimenta AR, Carvalho CS, et al. Investigating counterfeiting of an artwork by XRF, SEM-EDS, FTIR and synchrotron radiation induced MA-XRF at LNLS-BRAZIL. Spectrochimica Acta Part A: Molecular and Biomolecular Spectroscopy. 2021 Feb 5;246:118925.

58. Pendleton MW, Washburn DK, Ellis EA, Pendleton BB. Comparing the Detection of Iron-Based Pottery Pigment on a Carbon-Coated Sherd by SEM-EDS and by Micro-XRF-SEM. Yale J Biol Med. 2014 Mar 5;87(1):15–20.

59. Oliver WC, Pharr GM. An improved technique for determining hardness and elastic modulus using load and displacement sensing indentation experiments. Journal of Materials Research. 1992 Jun 1;7(6):1564–83.

60. Zhang H, Stewart M, De Luca F, Smet PF, Sousanis A, Poelman D, et al. Young's modulus of thin SmS films measured by nanoindentation and laser acoustic wave. Surface and Coatings Technology. 2021 Sep 15;421:127428.

61. Liu C, Nagler O, Tremmel F, Unterreitmeier M, Frick JJ, Patil RP, et al. Cluster-based acoustic emission signal processing and loading rate effects study of nanoindentation on thin film stack structures. Mechanical Systems and Signal Processing. 2022 Feb 15;165:108301.

62. Wang H, Zhu L, Xu B. Principle and Methods of Nanoindentation Test. In: Residual Stresses and Nanoindentation Testing of Films and Coatings [Internet]. Singapore: Springer Singapore; 2018 [cited 2022 Jul 11]. p. 21–36. Available from: http://link.springer.com/10.1007/978-981-10-7841-5_2

63. Dean J, Aldrich-Smith G, Clyne TW. Use of nanoindentation to measure residual stresses in surface layers. Acta Materialia. 2011 Apr 1;59(7):2749–61.

64. Ebenstein DM, Pruitt LA. Nanoindentation of biological materials. Nano Today. 2006 Aug 1;1(3):26–33.

65. Oyen ML, Cook RF. A practical guide for analysis of nanoindentation data. Journal of the Mechanical Behavior of Biomedical Materials. 2009 Aug 1;2(4):396–407.

66. Gao X, Hao F, Fang D, Huang Z. Boussinesq problem with the surface effect and its application to contact mechanics at the nanoscale. International Journal of Solids and Structures. 2013 Aug 1;50(16):2620–30.

67. An analysis of nanoindentation in elasto-plastic solids | Elsevier Enhanced Reader [Internet]. [cited 2022 Jul 14]. Available from: https://reader.elsevier.com/reader/sd/pii/S0020768308003259?token=6364E4D 4C85B2D89E1575D7060F1C4BBAB5CA37FEF2C53BF7C5843FEE77598BF 77B9D13DDF8153D071E8D78E2A49C9D8&originRegion=eu-west-1&originCreation=20220714223345

68. Oliver WC. Measurement of hardness and elastic modulus by instrumented indentation: Advances in understanding and refinements to methodology. Journal of Materials Research. :3–20.

69. Strader JH, Shim S, Bei H, Oliver WC, Pharr GM. An experimental evaluation of the constant β relating the contact stiffness to the contact area in nanoindentation. Philosophical Magazine. 2006 Nov 21;86(33–35):5285–98.

70. Wu Z, Baker TA, Ovaert TC, Niebur GL. The effect of holding time on nanoindentation measurements of creep in bone. Journal of Biomechanics. 2011 Apr 7;44(6):1066–72.

71. Chen T, He L, Cullison MH, Hay C, Burns J, Wu Y, et al. The correlation between microstructure and nanoindentation property of neutron-irradiated austenitic alloy D9. Acta Materialia. 2020 Aug 15;195:433–45.

72. Wang Z, Nayak PK, Caraveo-Frescas JA, Alshareef HN. Recent Developments in p-Type Oxide Semiconductor Materials and Devices. Advanced Materials. 2016;28(20):3831–92.

73. Wasmer K, Gassilloud R, Michler J, Ballif C. Analysis of onset of dislocation nucleation during nanoindentation and nanoscratching of InP. Journal of Materials Research. 2012 Jan;27(1):320–9.

74. Jiang C, Lu H, Zhang H, Shen Y, Lu Y. Recent Advances on In Situ SEM Mechanical and Electrical Characterization of Low-Dimensional Nanomaterials. Scanning. 2017 Oct 25;2017:e1985149.

75. Nili H, Kalantar-zadeh K, Bhaskaran M, Sriram S. In situ nanoindentation: Probing nanoscale multifunctionality. Progress in Materials Science. 2013 Jan 1;58(1):1–29.

76. Diao Y, Tee BCK, Giri G, Xu J, Kim DH, Becerril HA, et al. Solution coating of large-area organic semiconductor thin films with aligned single-crystalline domains. Nature Mater. 2013 Jul;12(7):665–71.

77. Tarefder RA, Faisal H. Effects of Dwell Time and Loading Rate on the Nanoindentation Behavior of Asphaltic Materials. Journal of Nanomechanics and Micromechanics. 2013 Jun 1;3(2):17–23.

78. Herbert EG, Sudharshan Phani P, Johanns KE. Nanoindentation of viscoelastic solids: A critical assessment of experimental methods. Current Opinion in Solid State and Materials Science. 2015 Dec 1;19(6):334–9.

79. Hintsala ED, Hangen U, Stauffer DD. High-Throughput Nanoindentation for Statistical and Spatial Property Determination. JOM. 2018 Apr 1;70(4):494–503.

80. New England Complex Systems Institute [Internet]. [cited 2022 Sep 15]. Concepts: Power Law. Available from: https://necsi.edu/power-law

81. Bian K, Gerber C, Heinrich AJ, Müller DJ, Scheuring S, Jiang Y. Scanning probe microscopy. Nat Rev Methods Primers. 2021 May 13;1(1):1–29.

82. Currey JD, Landete-Castillejos T, Estevez J, Ceacero F, Olguin A, Garcia A, et al. The mechanical properties of red deer antler bone when used in fighting. J Exp Biol. 2009 Dec;212(Pt 24):3985–93.

83. Rodriguez-Florez N, Oyen ML, Shefelbine SJ. Insight into differences in nanoindentation properties of bone. Journal of the Mechanical Behavior of Biomedical Materials. 2013 Feb 1;18:90–9.

84. Liu Y, Luo D, Wang T. Hierarchical Structures of Bone and Bioinspired Bone Tissue Engineering. Small. 2016;12(34):4611–32.

85. Emri I, Gonzalez-Gutierrez J, Gergesova M, Zupančič BV, Saprunov I. Experimental Determination of Material Time-Dependent Properties. In: Hetnarski RB, editor. Encyclopedia of Thermal Stresses [Internet]. Dordrecht: Springer Netherlands; 2014 [cited 2022 Aug 21]. p. 1494–510. Available from: https://doi.org/10.1007/978-94-007-2739-7_907

86. Yang S, Zhang YW, Zeng K. Analysis of nanoindentation creep for polymeric materials. Journal of Applied Physics. 2004 Apr;95(7):3655–66.

87. Olesiak SE, Oyen ML, Ferguson VL. Viscous-elastic-plastic behavior of bone using Berkovich nanoindentation. Mech Time-Depend Mater. 2010 May 1;14(2):111–24.

88. Ho WF, Ju CP, Chern Lin JH. Structure and properties of cast binary Ti-Mo alloys. Biomaterials. 1999;20(22):2115–22.

89. Kobayashi E, Matsumoto S, Doi H, Yoneyama T, Hamanaka H. Mechanical properties of the binary titanium-zirconium alloys and their potential for biomedical materials. Journal of Biomedical Materials Research. 1995;29(8):943–50.

90. Oliveira NTC, Aleixo G, Caram R, Guastaldi AC. Development of Ti–Mo alloys for biomedical applications: Microstructure and electrochemical characterization. Materials Science and Engineering: A. 2007 Apr 15;452–453:727–31.

91. Sugano M, Tsuchida Y, Satake T, Ikeda M. A microstructural study of fatigue fracture in titanium–molybdenum alloys. Materials Science and Engineering: A. 1998 Mar 15;243(1):163–8.

92. Guo H, Enomoto M. Surface reconstruction associated with α precipitation in a Ti-Mo alloy. Scripta Materialia. 2006;54(7):1409–13.

93. Sukedai E, Yoshimitsu D, Matsumoto H, Hashimoto H, Kiritani M. β to ω phase transformation due to aging in a Ti-Mo alloy deformed in impact compression. Materials Science and Engineering A. 2003;350(1–2):133–8.

94. Zhao N, Wang Z, Cai C, Shen H, Liang F, Wang D, et al. Bioinspired Materials: from Low to High Dimensional Structure. Advanced Materials. 2014 Nov;26(41):6994–7017.

95. Katiyar NK, Goel G, Hawi S, Goel S. Nature-inspired materials: Emerging trends and prospects. NPG Asia Mater. 2021 Jul 30;13(1):1–16.

96. Luz GM, Mano JF. Biomimetic design of materials and biomaterials inspired by the structure of nacre. Philosophical Transactions of the Royal Society A: Mathematical, Physical and Engineering Sciences. 2009 Apr 28;367(1893):1587–605.

97. Rousseau M, Lopez E, Stempflé P, Brendlé M, Franke L, Guette A, et al. Multiscale structure of sheet nacre. Biomaterials. 2005 Nov 1;26(31):6254–62.

98. Naveen J, Jawaid M, Goh KL, Reddy DM, Muthukumar C, Loganathan TM, et al. Advancement in Graphene-Based Materials and Their Nacre Inspired Composites for Armour Applications—A Review. Nanomaterials. 2021 May;11(5):1239.

99. Yang Y, Li X, Chu M, Sun H, Jin J, Yu K, et al. Electrically assisted 3D printing of nacre-inspired structures with self-sensing capability. Science Advances. 2019 Apr 5;5(4):eaau9490.

100. Libonati F, Vellwock AE, Ielmini F, Abliz D, Ziegmann G, Vergani L. Bone-inspired enhanced fracture toughness of de novo fiber reinforced composites. Sci Rep. 2019 Feb 28;9(1):3142.

101. Wegst UGK, Bai H, Saiz E, Tomsia AP, Ritchie RO. Bioinspired structural materials. Nature Mater. 2015 Jan;14(1):23–36.

102. Fratzl P, Weinkamer R. Nature's hierarchical materials. Progress in Materials Science. 2007 Nov 1;52(8):1263–334.

103. Reznikov N, Shahar R, Weiner S. Bone hierarchical structure in three dimensions. Acta Biomaterialia. 2014 Sep 1;10(9):3815–26.

104. Checa AG, Salas C, Rodríguez-Navarro AB, Grenier C, Lagos NA. Articulation and growth of skeletal elements in balanid barnacles (Balanidae, Balanomorpha, Cirripedia). Royal Society Open Science. 6(9):190458.

105. Checa AG, González-Segura A, Rodríguez-Navarro AB, Lagos NA. Microstructure and crystallography of the wall plates of the giant barnacle Austromegabalanus psittacus: a material organized by crystal growth. J R Soc Interface. 2020 Mar;17(164):20190743.

106. Lincoln GA, Tyler NJ. Role of oestradiol in the regulation of the seasonal antler cycle in female reindeer, Rangifer tarandus. J Reprod Fertil. 1999 Jan;115(1):167–74.

107. Bubenik GA, White R, Bartos L. Antler growth in male and female reindeer and its relationship to sesonal blood levels of alkaline phosphatase. Folia Zoologica. 2000 Jan 1;49:161–6.

108. Reimers E, Nieminen M, Tsegaye D. Antler casting in relation to parturition in semi-domesticated female reindeer. Rangifer. 2013 Jan 27;33.

109. Landete-Castillejos T, Garcia A, Gallego L. Body weight, early growth and antler size influence antler bone mineral composition of Iberian red deer (Cervus elaphus hispanicus). Bone. 2007 Jan;40(1):230–5.

110. Landete-Castillejos T, Kierdorf H, Gomez S, Luna S, García AJ, Cappelli J, et al. Antlers - Evolution, development, structure, composition, and biomechanics of an outstanding type of bone. Bone. 2019 Nov 1;128:115046.

111. Baxter BJ, Andrews RN, Barrell GK. Bone turnover associated with antler growth in red deer (Cervus elaphus). Anat Rec. 1999 Sep 1;256(1):14–9.

112. Wang D, Berg D, Ba H, Sun H, Wang Z, Li C. Deer antler stem cells are a novel type of cells that sustain full regeneration of a mammalian organ—deer antler. Cell Death Dis. 2019 Jun 5;10(6):1–13.

113. Landete-Castillejos T, Estevez JA, Martínez A, Ceacero F, Garcia A, Gallego L. Does chemical composition of antler bone reflect the physiological effort made to grow it? Bone. 2007 Apr;40(4):1095–102.

114. Banks Jr. WJ, Epling GP, Kainer RA, Davis RW. Antler growth and osteoporosis I. Morphological and morphometric changes in the costal compacta during the antler growth cycle. The Anatomical Record. 1968;162(4):387–97.

115. Endochondral Ossification - an overview | ScienceDirect Topics [Internet]. [cited 2022 Oct 1]. Available from: https://www.sciencedirect.com/topics/veterinary-science-and-veterinary-medicine/endochondral-ossification

116. Dryden GM, Dryden GM. Nutrition of antler growth in deer. Anim Prod Sci. 2016 Feb 25;56(6):962–70.

117. Baksi SN, Newbrey JW. Bone metabolism during antler growth in female reindeer. Calcif Tissue Int. 1989 Mar 1;45(5):314–7.

118. Landete-Castillejos T, Currey JD, Ceacero F, García AJ, Gallego L, Gomez S. Does nutrition affect bone porosity and mineral tissue distribution in deer antlers? The relationship between histology, mechanical properties and mineral composition. Bone. 2012 Jan 1;50(1):245–54.

119. Estevez J, Landete-Castillejos T, García A, Ceacero F, Gallego L. Population management and bone structural effects in composition and radio-opacity of Iberian red deer (Cervus elaphus hispanicus) antlers. European Journal of Wildlife Research. 2008 May 1;54:215–23.

120. Landete-Castillejos T, Currey JD, Estevez JA, Gaspar-López E, Garcia A, Gallego L. Influence of physiological effort of growth and chemical composition on antler bone mechanical properties. Bone. 2007 Nov;41(5):794–803.

121. Landete-Castillejos T, Currey JD, Estevez JA, Fierro Y, Calatayud A, Ceacero F, et al. Do drastic weather effects on diet influence changes in chemical composition, mechanical properties and structure in deer antlers? Bone. 2010 Oct 1;47(4):815–25.

122. Kierdorf U, Kierdorf H. Antlers as biomonitors of environmental pollution by lead and fluoride: A review. European Journal of Wildlife Research. 2005 Aug 31;51:137–50.

123. McDonald CG, Demarais S, Campbell TA, Janssen HF, Allen VG, Kelley AM. PHYSICAL AND CHEMICAL CHARACTERISTICS OF ANTLERS AND ANTLER BREAKAGE IN WHITE-TAILED DEER. swna. 2005 Sep;50(3):356–62.

124. Johnson HE, Bleich VC, Krausman PR. Mineral deficiencies in tule elk, Owens Valley, California. J Wildl Dis. 2007 Jan;43(1):61–74.

125. Wu J, Mai YW. The essential fracture work concept for toughness measurement of ductile polymers. Polymer Engineering & Science. 1996;36(18):2275–88.

126. Serrano MP, Gambín P, Landete-Castillejos T, García A, Cappelli J, Pérez-Barbería FJ, et al. Effects of Mn supplementation in late-gestating and lactating red deer (Cervus elaphus hispanicus) on milk production, milk composition, and calf growth. Journal of Animal Science. 2018 May 4;96(5):2038–49.

127. Weladji RB, Holand Ø, Steinheim G, Colman JE, Gjøstein H, Kosmo A. Sexual dimorphism and intercorhort variation in reindeer calf antler length is associated with density and weather. Oecologia. 2005 Oct 1;145(4):549–55.

128. Shah SR, DesJardins JD, Blob RW. Antler stiffness in caribou (Rangifer tarandus): testing variation in bone material properties between males and females. Zoology (Jena). 2008;111(6):476–82.

129. Mitchell RL, Coleman M, Davies P, North L, Pope EC, Pleydell-Pearce C, et al. Macro-to-nanoscale investigation of wall-plate joints in the acorn barnacle *Semibalanus balanoides* : correlative imaging, biological form and function, and bioinspiration. J R Soc Interface. 2019 Aug;16(157):20190218.

130. Pathak S, Swadener JG, Kalidindi SR, Courtland HW, Jepsen KJ, Goldman HM. Measuring the dynamic mechanical response of hydrated mouse bone by nanoindentation. J Mech Behav Biomed Mater. 2011 Jan;4(1):34–43.

131. Jirousek O. Nanoindentation of Human Trabecular Bone – Tissue Mechanical Properties Compared to Standard Engineering Test Methods. In: Nemecek J, editor. Nanoindentation in Materials Science [Internet]. InTech; 2012 [cited 2022 Jul 21]. Available from: http://www.intechopen.com/books/nanoindentation-in-materials-

science/nanoindentation-of-human-trabecular-bone-tissue-mechanical-properties-compared-to-standard-engineeri

132. 14:00-17:00. ISO. [cited 2022 Jul 21]. ISO 14577-1:2015. Available from: https://www.iso.org/cms/render/live/en/sites/isoorg/contents/data/standard/05/66/56626.html

133. Sun X, Li L, Guo Y, Zhao H, Zhang S, Yu Y, et al. Influences of organic component on mechanical property of cortical bone with different water content by nanoindentation. AIP Advances. 2018 Mar;8(3):035003.

134. ImageJ Wiki [Internet]. [cited 2022 Sep 24]. BoneJ. Available from: https://imagej.github.io/plugins/bonej

135. Rondanelli M, Faliva MA, Peroni G, Infantino V, Gasparri C, Iannello G, et al. Essentiality of Manganese for Bone Health: An Overview and Update. Natural Product Communications. 2021 May 1;16(5):1934578X211016649.

136. Buddhachat K, Klinhom S, Siengdee P, Brown JL, Nomsiri R, Kaewmong P, et al. Elemental Analysis of Bone, Teeth, Horn and Antler in Different Animal Species Using Non-Invasive Handheld X-Ray Fluorescence. PLOS ONE. 2016 May 19;11(5):e0155458.

137. US Department of Commerce NO and AA. What are barnacles? [Internet]. [cited 2022 Nov 3]. Available from: https://oceanservice.noaa.gov/facts/barnacles.html

138. Cornwall IE. Barnacle shell figures and repairs. Can J Zool. 1960 Aug;38(4):827–32.

139. Perez-Huerta A, Zhu W. Assessment of crystallographic influence on material properties of calcite brachiopods. Mineralogical Magazine. 2008 Apr 1;72.

140. Sly MK, Thind AS, Mishra R, Flores KM, Skemer P. Low-temperature rheology of calcite. Geophysical Journal International. 2020 Apr 1;221(1):129–41.

141. Murdock GR, Currey JD. Strength and Design of Shells of the Two Ecologically Distinct Barnacles, Balanus balanus and Semibalanus (Balanus) balanoides (Cirripedia). Biological Bulletin. 1978;155(1):169–92.

142. Rössner GE, Costeur L, Scheyer TM. Antiquity and fundamental processes of the antler cycle in Cervidae (Mammalia). Sci Nat. 2020 Dec 16;108(1):3.

143. Kierdorf U, Stock S, Gomez S, Antipova O, Kierdorf H. Distribution, structure, and mineralization of calcified cartilage remnants in hard antlers. Bone Reports. 2022 Apr 1;16:101571.

144. Carlisle ER, Fischgrund JS. CHAPTER 27 - Bone Graft and Fusion Enhancement. In: Errico TJ, Lonner BS, Moulton AW, editors. Surgical Management of Spinal Deformities [Internet]. Philadelphia: W.B. Saunders; 2009 [cited 2022 Nov 13]. p. 433–48. Available from: https://www.sciencedirect.com/science/article/pii/B9781416033721500305

145. Singh RR, Khanna PP, Singh AK, Goyal SP. Elemental characterization of antlers of various deer species using X-Ray Fluorescence (XRF): A tool for forensic examination. Forensic Science International. 2022 Mar 1;332:111172.

146. Cappelli J, Garcia A, Ceacero F, Gomez S, Luna S, Gallego L, et al. Manganese Supplementation in Deer under Balanced Diet Increases Impact Energy and Contents in Minerals of Antler Bone Tissue. PLOS ONE. 2015 Jul 15;10(7):e0132738.

147. Melnycky NA, Weladji RB, Holand Ø, Nieminen M. Scaling of antler size in reindeer (Rangifer tarandus): sexual dimorphism and variability in resource allocation. Journal of Mammalogy. 2013 Dec 16;94(6):1371–9.

148. Gómez JÁ, Landete-Castillejos T, García AJ, Gallego L. Importance of growth during lactation on body size and antler development in the Iberian red deer (Cervus elaphus hispanicus). Livestock Science. 2006 Dec 1;105(1):27–34.

149. Gómez J, Landete-Castillejos T, García AJ, Gaspar-López E, Estevez JA, Gallego L. Lactation growth influences mineral composition of first antler in Iberian red deer Cervus elaphus hispanicus. wbio. 2008 Sep;14(3):331–8.

150. Garulli T, Katafiasz TJ, Greenhalgh ES, Pinho ST. A novel bio-inspired microstructure for improved compressive performance of multidirectional CFRP laminates. Composites Part B: Engineering. 2023 Sep 1;264:110867.

151. Fan Z, Swadener JG, Rho JY, Roy ME, Pharr GM. Anisotropic properties of human tibial cortical bone as measured by nanoindentation. Journal of Orthopaedic Research. 2002;20(4):806–10.

152. Ziv V, Wagner HD, Weiner S. Microstructure-microhardness relations in parallel-fibered and lamellar bone. Bone. 1996 May 1;18(5):417–28.

153. de Bien C, Mengoni M, otreppe V, Freichels H, Jérôme C, Ponthot JP, et al. Development of a biomechanical model of deer antler cancellous bone based on X-ray microtomographic images. 2012 Apr 1;